

Determining Random Vibration Response of Terrestrial Rovers from Ground Inputs

Détermination de la réponse aux vibrations aléatoires des véhicules terrestres à partir des entrées au sol

A Thesis Submitted to the Division of Graduate Studies of the
Royal Military College of Canada by
William Phippen, MAsc, RMC

In Partial Fulfillment of the Requirement for the Degree of
Master of Applied Science in Mechanical Engineering
August 2019

© This thesis may be used within the Department of National Defence but
copyright for open publication remains the property of the author.

Without the love and support of my fiancée Paisley I would not have been able to endure the challenges of parenting, working and completing this research. Thank you for your encouragement and love throughout this chapter of life. In addition to this I could not have succeeded to this point without the inspiration of my loving children Miles and Mya, you both inspire me and give me the motivation needed to be successful.

Acknowledgements

I would like to thank Dr. Diane Wowk for her support and mentorship as I completed my research and thesis. I would also like to acknowledge Dr. Il-Yong Kim for his teachings and guidance as it led me towards the research I completed and gave me the fundamental knowledge to start this work. Thank you to Mr. Stephen Roper for your continued support as I struggled through this research and also to Mr. Wennian Yu for your assistance as it was needed. Lastly a special thank you to Dr. Kim Woodhouse, without your support in the very early stage of my educational career I would not have had this opportunity.

Abstract

Terrestrial rovers will play an important role in space exploration on the Moon and Martian surfaces. Before a rover is launched there are several series of testing, and design changes to ensure the rover will last the life of the mission. Currently the Canadian Space Agency (CSA) works with companies such as Neptec to test prototype rovers at the CSA's Mars Emulation Terrain (MET). This allows engineers and scientists to test new designs and equipment to handle the terrain that could be faced on another planet's surface, by modifying suspension and damping systems. The current method of building prototypes and testing them on the MET is useful but costly and does not fully represent the surface topology that the rovers will encounter. The current work presents the foundation for determining a representative vibration input for a given terrain type, with a single model determining the vibration response of a lunar test rover. More specifically the vibration over a known aggregate was determined in the form of a power spectral density (PSD) to be used as an input to a finite element (FE) model, to give the response PSD of the rover. The predicted PSD of the rover was compared to the experimental PSD, and was within the probability of 3σ of occurrence at specific frequencies thus verifying the FE model. It was determined that at low frequencies less than 1000Hz, the method of double integration was more reliable for generating vibration displacement trend data from accelerometer data for the rover and at high frequencies, above 1000Hz, the Omega arithmetic method was more reliable. Additionally, when the magnitude of the displacement is needed the omega arithmetic method should be used. The FE model is able to predict the absolute excitation and payload excitation for a given terrain PSD input, and can be used in the next step toward future modelling of the vibration inputs of a planet's surface given its terrain's topology.

Résumé

Les rovers terrestres joueront un rôle important dans l'exploration spatiale des surfaces lunaires et martiennes. Avant le lancement d'un mobile, plusieurs séries de tests sont nécessaires et des modifications de conception ont été prises pour que le mobile dure toute la vie. Actuellement, l'Agence spatiale canadienne (ASC) collabore avec des entreprises telles que Neptec pour tester des prototypes de rovers sur le terrain d'émulation de Mars (MET) de l'ASC. Cela permet aux ingénieurs et aux scientifiques de tester de nouvelles conceptions et de nouveaux équipements pour gérer le terrain qui pourrait être exposé sur la surface d'une autre planète, en modifiant les systèmes de suspension et d'amortissement. La méthode actuelle de construction et de test des prototypes sur le MET est utile mais coûteuse et ne représente pas pleinement la topologie des surfaces que les rovers rencontreront. Les travaux en cours présentent les bases permettant de déterminer une entrée de vibration représentative pour un type de terrain donné, un modèle unique déterminant la vibration de réponse d'un mobile d'essai lunaire. Plus spécifiquement, la vibration sur un agrégat connu a été déterminée sous la forme d'une densité spectrale de puissance (DSP) à utiliser comme entrée d'un modèle d'éléments finis (EF), pour donner la réponse DSP du mobile. La DSP prévue du mobile a été comparée à la DSP expérimentale et se situait dans la probabilité d'occurrence de 3σ à des fréquences spécifiques, ce qui a permis de vérifier le modèle EF. Il a été déterminé qu'aux basses fréquences, inférieures à 1000 Hz, la méthode de la double intégration était plus fiable pour générer des données de tendance de déplacement de vibrations à partir des données de l'accéléromètre du mobile et aux hautes fréquences, supérieures à 1000 Hz, la méthode arithmétique Omega était plus fiable. De plus, lorsque la magnitude du déplacement est nécessaire, la méthode arithmétique Oméga doit être utilisée. Le modèle d'EF est capable de prédire l'excitation absolue et la charge utile pour une entrée DSP de terrain donnée, et peut être utilisé dans la prochaine étape de modélisation future des entrées de vibrations de la surface d'une planète compte tenu de la topologie de son terrain.

Table of Contents

Acknowledgements.....	iii
Abstract.....	iv
Résumé.....	v
Table of Contents.....	vi
List of Tables.....	viii
List of Figures.....	ix
List of Acronyms.....	xii
List of Symbols.....	xiii
1. Introduction.....	1
1.1. Motivation.....	4
1.2. Goals.....	5
1.3. Methodology.....	6
1.4. Chapter Overview.....	6
2. Literature Review.....	7
2.1. Background.....	7
2.1.1. Vibration.....	7
2.1.1.1. Natural Frequency and Damping.....	8
2.1.2. Modal Analysis.....	9
2.1.2.1. Modal Super Position to Describe System Vibration.....	10
2.1.3. Random Vibration.....	11
2.2. PSD.....	13
2.2.1. PSD – Definition.....	13
2.2.2. PSD Generation.....	14
2.2.2.1. PSD Generation from Complex Conjugate.....	15
2.2.2.2. Welch Method.....	16
2.2.2.3. PSD Refinement.....	16
2.2.3. Analyzing Time History Data.....	17
2.2.3.1. Leakage and Windowing.....	21
2.2.3.2. Displacement Time Histories.....	25
2.2.3.2.1. Integration.....	25
2.2.3.2.2. Omega Arithmetic Method.....	26
2.3. Modelling Vibration.....	28
2.3.1. Analysis Type.....	28
2.3.2. Performing and Interpreting Structural Dynamic Analyses.....	30
2.3.2.1. Interpreting Response PSD.....	31
2.3.2.2. Analyzing PSD Curves for Dynamic Motion.....	32
2.3.3. Testing Standards.....	34
2.3.3.1. Military Standards.....	35
2.4. Ground Vehicle Vibration Analysis and Simulation.....	38
2.5. Areas for Further Research (Vibration Response Spectrum).....	38
3. Methodology.....	42
3.1. Introduction.....	42
3.2. Model details.....	51

3.2.1.	Rover Geometry.....	51
3.2.1.1.	Initial Rover Geometry	52
3.2.1.2.	Baseline Rover Geometry	54
3.2.2.	Material Properties.....	57
3.2.3.	Mesh.....	57
3.2.3.1.	Element Type and Mesh Density Study.....	58
3.2.4.	Loading and Boundary Conditions	62
3.2.5.	Solution.....	63
3.3.	PSD Generation	63
3.3.1.	Acceleration PSD Generation from Accelerometer Data	64
3.3.2.	Omega Method.....	67
3.3.3.	Integration Method.....	69
3.4.	Damping Effects on Vibration Response.....	72
4.	Results.....	77
4.1.	FE Model Verification	77
4.1.1.	Input for Model Verification.....	77
4.1.2.	Baseline Model Analysis	79
4.2.	Input PSD Evaluation	87
4.2.1.	Generated PSDs	91
5.	Discussion.....	94
5.1.	Additional Model Evaluation.....	94
5.1.1.	Effect of Geometry on Response PSD.....	94
5.1.1.1.	Effect of Rover Geometry on Response PSD	98
5.1.2.	Effect of Loading and Boundary Conditions on Response PSD.....	99
5.1.2.1.	Boundary Condition Variation.....	99
5.1.2.2.	Loading Variation	101
5.1.3.	Accounting for Payloads and Impact on Response PSD	104
5.2.	CSA Rover Analysis.....	106
6.	Conclusions and Future Work	108
6.1.	Future Work.....	108
	Reference	110
	Appendix A.....	116

List of Tables

Table 1: Multi-planet civilization progression [1-4].	2
Table 2: Vibration systems overview.	7
Table 3: Effects of damping on a system's step response.	9
Table 4: Fourier transform Omega Arithmetic [38, 41].	28
Table 5: Spectral density Omega Arithmetic [38, 41].	28
Table 6: Peak output from PSD NAVMAT [41].	32
Table 7: Automobile natural frequencies [47].	33
Table 8: Juno rover overview [57].	42
Table 9: Rock Bed details [57].	44
Table 10: Material properties.	57
Table 11: Modes of lower order and higher order FE models at 2.5% damping.	60
Table 12: Mesh density comparison using higher and lower order elements with input PSD generated from CSA raw acceleration data.	61
Table 13: Modal result comparison for nominal and high density mesh.	61
Table 14: Juno rover modal analysis 8x Scale.	80
Table 15: Modes of simulated geometries.	97
Table 16: Overall GRMS comparison of Initial to Baseline model.	98
Table 17: First five modes due to varying PSD input on a constant geometry.	100
Table 18: First five modes with and without the presence of a point mass with constant geometry and volume.	104
Table 19: Output PSD with & without 37kg point load included in Input PSD.	105
Table 20: Mode 1-10 of model with & without Payload.	105

List of Figures

Figure 1: Acceptance Response PSD Level Specification for terrestrial space rovers during operation [5].	5
Figure 2: First three modes of a cantilever beam in 3D, with fixed zero DOF end.	10
Figure 3: Normal distribution representation of random vibration 3σ includes 99.7% of expected peaks [12].	12
Figure 4: PSDs of identical broadband data measured with 1 Hz spectral resolution (red), 4 Hz spectral resolution (green) and 8 Hz spectral resolution (blue) , showing trend and amplitude differences [14]	13
Figure 5: Example of a 200Hz sine function sampled at 2000Hz.	19
Figure 6: 1800Hz sine function sampled at 2000Hz.	19
Figure 7: Aliasing overlay of 200Hz and 1800Hz signals samples at 2000Hz, signals are seen as identical with 180° phase shift.	20
Figure 8: Fourier transform of 1800Hz signal sampled at 2000Hz showing a spectral peak at 200Hz due to aliasing.	20
Figure 9: FT of well acquired signal giving spectral peak at 1Hz [30].	21
Figure 10: FT of poorly acquired signal with leakage about the 1Hz peak [30].	22
Figure 11: Implementation of windowing on time history to reduce leakage about the 1Hz spectral peak [30].	23
Figure 12: Windowing of time history segments, with no overlapping data is lost, with 50% overlapping 90% of time history is recovered and leakage minimized [15].	24
Figure 13: Modal super position of 3 mode system providing full system deformation.	29
Figure 14: Response PSD from NAVMAT P-9492 input PSD specification [41].	31
Figure 15: Vehicle response PSD, highlighting three spectral peaks due to input PSD [47].	33
Figure 16: Sample PSD test specification profile for Naval shaker table capabilities [48].	35
Figure 17: MIL-STD-1540C Section 7 Minimum Random Vibration Spectrum – Unit Test [49].	36
Figure 18: Equivalent acceleration, velocity and displacement NAVMAT input PSD for electronic component testing [48, 50].	37
Figure 19: Example of response PSDs based on varying natural frequencies to a base input per MIL-STD-1540C [55].	39
Figure 20: VRS example from MIL-STD-1540C base input, validating that peak responses are not exceeded based on response PSD [55].	40
Figure 21: Flight data PSD and specification limit showing two spectral peaks above the PSD test limits [55].	41
Figure 22: Flight data VRS and specification limit showing that the vibration in flight does not exceed the test limit specifications [34].	41
Figure 23: Juno Rover with rubber tires.	42
Figure 24: Payload configuration [58].	43
Figure 25: CSA MET, with Rock Bed area highlight in red box [54].	43
Figure 26: Accelerometer placement on Juno, adapted from CSA [5].	49

Figure 27: CSA field data response PSD at location 11 in the Z direction, as Juno drove on BR5 with payload mounted.	50
Figure 28: Raw accelerometer data from CSA accelerometer 5Z.	51
Figure 29: Initial rover geometry ANSYS divisions for meshing.	52
Figure 30: Location of FE model origin.	53
Figure 31: Detail A - Chassis Cross Sectional Supports.....	54
Figure 32: Baseline rover geometry showing divisions for meshing.....	55
Figure 33: Detail G - Swash Plate Geometry.....	56
Figure 34: Baseline rover geometry - Swash Plate are highlighted by the green boxes.	56
Figure 35: Fully meshed Baseline rover.	58
Figure 36: Comparison of higher and lower order element response PSD with 2.5% damping against field data response PSD at location 11Z.	59
Figure 37: Boundary conditions with motor arms constrained ($U_X = 0$, $U_Z = 0$)..	62
Figure 38: ANSYS best fit of displacement PSD data.....	63
Figure 39: Raw accelerometer data from CSA accelerometer 5Z.	65
Figure 40: Generated PSD from 5Z accelerometer data without payload present against CSA provided PSD with payload present, log-log format.	66
Figure 41: Raw acceleration data from 5Z and displacement data generated using Omega Method.	68
Figure 42: Displacement PSD generated using the Omega Arithmetic Method, in log-log format from CSA 5Z accelerometer.	69
Figure 43: First integration of accelerometer 5Z data to generate velocity data.....	70
Figure 44: Double integration of accelerometer 5Z data to generate displacement data.....	71
Figure 45: Displacement PSD generated with Welch Method from Double Integration using log-log format.	72
Figure 46: Output PSD for sensor 11Z field versus simulated response PSD at 1% damping.	73
Figure 47: Output PSD for sensor 11Z field versus simulated response PSD at 2.5% damping.	74
Figure 48: Difference in Output PSD magnitude for 11Z omega method versus integration method generation	75
Figure 49: Base accelerometer locations on Juno's wheels, adapted from CSA [5].	78
Figure 50: 1Z output PSD provided by CSA from BR5 (D) [5].....	79
Figure 51: Visual representation of vibration path to location 11Z on chassis.....	85
Figure 52: Comparison of field data to simulated data at chassis location 11z.	86
Figure 53: Z-axis 3σ simulated response PSD comparison with field data generated response PSDs with 2.5% damping used in the FE modelling.....	88
Figure 54: Payload Z-axis 3σ simulated response PSD comparison with field data generated response PSDs with 2.5% damping used in the FE modelling.....	89
Figure 55: Actuator mounting point to drive arm actual comparison to FE model simplification provided in a) and b), connectional axel joint simplification provided in c) and d).	90
Figure 56: Generated input PSD comparison between Double Integration Method and Omega Arithmetic Method of displacement	92
Figure 57: Constant PSD input (White Noise vibration input) at $10G^2/Hz$	94

Figure 58: Geometry variation with approximately constant volume = $1 \times 10^6 \text{mm}^2$	95
Figure 59: Response PSD spectrum for constant geometry, volume model and input PSD with different loading cases.	96
Figure 60: Model 8 mode 3, torsional deformation. Red represents areas of large displacement, and dark blue indicates zero displacement.	97
Figure 61: Solid steel cube with response PSD probes used to determine relationship between input and response PSD based on varying loading faces.	99
Figure 62: Response PSD spectrum for constant geometry and volume model with different input PSD variations.	101
Figure 63: Solid steel cube with response PSD probes used to determine relationship between response PSD and unbalanced loading based on a point load.	102
Figure 64: Response PSD spectrum for constant geometry, volume model and input PSD with different loading cases.	103

List of Acronyms

AGREE	Advisory Group on Reliability of Electronic Equipment
CF	Crest Factor
CSA	Canadian Space Agency
DFT	Discrete Fourier Transform
DOF	Degree of Freedom
ELV	Expendable Launch Vehicle
EOM	Equations of Motion
FE	Finite Element
FFT	Fast Fourier Transform
FT	Fourier Transform
G	Gravitational equivalent units
GRMS	Gravitation Root Mean Square
LVDT	Linear Variable Displacement Transducer
MDOF	Multiple Degree of Freedom
MET	Mars Emulation Terrain
ODE	Ordinary Differential Equation
PCB	Printed Circuit Board
PDE	Partial Differential Equation
PSD	Power Spectral Density
RMS	Root Mean Square
SDOF	Single Degree of Freedom
STS	Space Transport System
VRS	Vibration Response Spectrum
WOSA	Weighted Overlapped Segment Averaging



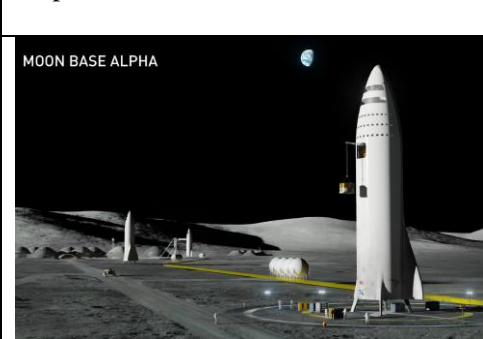
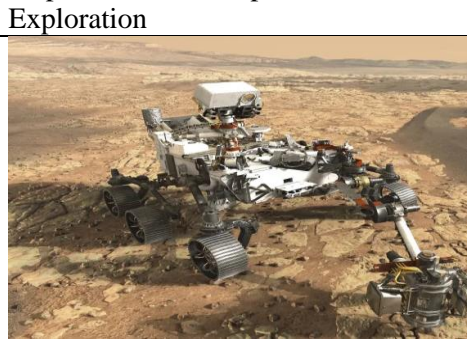

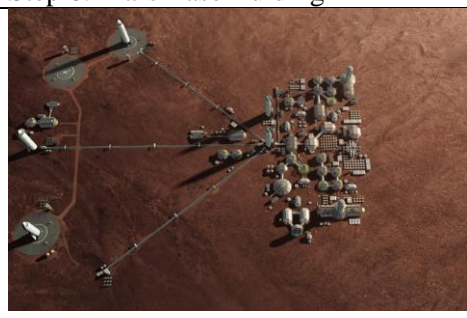


List of Symbols

c_c	Critical Damping Ratio
f	Frequency
f_N	Nyquist Frequency
f_n	Natural Frequency
m	Mass or Mass Matrix
$x(t)$	Displacement as a function of time
$w(t)$	Windowing Function
B	Bandwidth of ideal rectangular filter
C or c	Damping Coefficient or Damping Matrix
C_{tire}	Circumference of tire/wheel
F	Force
K	Stiffness or Stiffness Matrix
M	Sampling Coefficient based on Input PSD
N	Number of samples
Q	Q factor for system damping
T	Time duration
$X(f)$	Displacement as a function of frequency
W	Sampling Coefficient based on Maximum Analysis Frequency
ω_n	Angular Natural Frequency
Δf	Frequency Resolution
Δt	Time of sample separation
ζ	Damping Ratio
σ	Standard Deviation
ω	Angular Frequency
ϕ	Phase Angle
\hat{X}_{PSD}	One Sided PSD
$\ddot{X}(f)$	Acceleration as a function of frequency
$\dot{X}(f)$	Velocity as a function of frequency
X_{PSD}	Double Sided PSD
$\ddot{x}(t)$	Acceleration as a function of time
$\dot{x}(t)$	Velocity as a function of time
$[I]$	Identity Matrix
$\{a\}$	Vector of Mode Shapes
$\Delta(\bar{x}^2)$	Filtered Mean Square

1. Introduction

Terrestrial space rover exploration started with the lunar rover Lunokhod 0 from the Soviet Union, but the mission was not successful as the rover crashed on February 19, 1969. This mission was followed up with Lunokhod 1 being the first successful lunar rover, landing on the surface of the moon on Nov. 10, 1970. The successful Moon landing led to the Soviets attempts to land a rover on the Martian surface. However, the first successful Mars rover landing was completed by National Aeronautics and Space Administration (NASA) when Spirit landed on Jan 4, 2004. In today's space exploration programs the push is to use the Moon as a stepping stone to Mars. The most recent venture is between NASA and the Canadian Space Agency (CSA) called "Lunar Gateway". This project is to set up a base station orbiting the Moon by the year 2026, and then create rocket launch pads on the Moon's surface to allow easier transport to Mars [1]. Terrestrial rovers will play an important part in this project as they will search for useable resources on the Moon's surface and study the lunar mineralogy and chemistry. As the lunar orbiter will be significantly closer to the rovers on the Moon, the communication relay will be faster and give better turnaround times on soil analysis and travel plans without having to send astronauts to the surface. This progression of space exploration leading up to the colonization of Mars can be seen in Table 1. Some of these steps are already underway with rovers evaluating the soil surface, the material properties of Mars, and searching for signs of life and water.

Table 1: Multi-planet civilization progression [1-4].

Step 1: Gateway	Step 2: Rover Exploration
 A 3D rendering of a space station (Gateway) in orbit around Earth. The station consists of a central hub and several modules, with solar panels extended. Earth is visible in the background.	 A 3D rendering of a rover on the surface of Mars. The rover is a six-wheeled vehicle with a camera mast and various instruments. The terrain is rocky and reddish-brown.
Step 3: Moon Launch Base	Step 4: Mars Development Exploration
 A 3D rendering of a launch base on the Moon. A large white rocket is being prepared for launch. The text "MOON BASE ALPHA" is visible in the top left corner. The lunar surface is dark and cratered.	 A 3D rendering of a Mars development site. A large, complex structure with multiple modules and solar panels is situated on the surface. The terrain is reddish-brown and rocky.
Step 5: Mars Base Start-Up	Step 6: Mars Base Buiding
 A 3D rendering of a Mars base start-up. A long, thin structure is being built on the surface. The text "BASE BUI" is visible in the bottom right corner. The terrain is reddish-brown.	 A 3D rendering of a Mars base building. A large, complex structure with multiple modules and solar panels is being built on the surface. The terrain is reddish-brown.
Step 7: Mars Colony Started	Step 8: Multi-Planet Civilization
 A 3D rendering of a Mars colony started. A large, complex structure with multiple modules and solar panels is built on the surface. The terrain is reddish-brown.	 A 3D rendering of a multi-planet civilization. A large, complex structure with multiple modules and solar panels is built on the surface. The terrain is reddish-brown.

Well before space programs get to the launch phase, there are several series of testing and design modifications. This testing includes the rover and payloads as well as the launch vehicles. Missions to the Moon and Mars take years to develop and once a rover and payload leave the Earth's surface they must function as intended without intervention for the life of the mission. Some of the important factors that need to be considered are handling vibrations during launch, travel to its destination and for the duration of exploration on the surface of the Moon or Mars. The Sun's radiation is another important factor as there is no atmosphere on either the Moon or Mars. Moon and Mars mission rovers have unique challenges from one another such as the communication lag time of 3 seconds between the Moon and the Earth versus minutes to hours on Mars. This means the rover needs to either wait or have some self-autonomy to drive and make decisions. Moon missions must also be able to handle a 2 week period of no sunlight and the vacuum of space draining all heat from the rover, whereas Mars despite cold winter weather, still has some light to allow battery charging. In both cases the vacuum of space needs to be considered. Unlike vehicles on the Earth's surface, some sections of the rover must be air tight in order to avoid contamination of organic material testing that occurs onboard the rover as soil samples are collected. Different types of drive systems are required for different missions as the lunar regolith is more abrasive than Martian soil. This thesis will focus on terrain types similar to that on Mars or the craters of the Moon.

Today the CSA currently works with NASA, a Canadian based company called Neptec (now Maxtar), as well as others to test prototype rovers at the CSA's Mars Emulation Terrain (MET). This allows engineers and scientists to evaluate the ability of new designs and equipment to handle the terrain that could be faced on another planet's surface. The ability to use the MET can provide valuable information as to how the rover performs. If the design cannot handle the test environment then new designs and new components must be built at additional cost. The CSA would like to simulate the rover driving over terrains through numerical models that use ground input spectrums to represent vibration so that multiple design iterations can be simulated and trialed without the cost and time of physically building prototype rovers. Allowing for the early test phases of a rover mission to be more efficient and having a better representation of the true surface of a planet will provide more reliable data to use in the final mission rover design. The focus of this thesis is on developing an input spectrum that can be used with a FE model of the rover in order to predict how it will respond when driving over a specified terrain. This will ultimately allow for design evaluation of rovers carrying different payloads over different terrains, through different maneuvers, and under different gravitational fields. The predictions from these simulations could be used in the initial design stages or with the final mission rover.

1.1. Motivation

Rover chassis and payloads such as instruments installed on the rover are designed to withstand the environment from the launch and operations. During operation, the rover and payloads are subjected to random vibrations caused mainly by the rover's displacement over the terrain. During the design phase, analyses are conducted to verify the strength of the rover chassis and natural frequency of both the rover and payload(s). The natural frequency is important to ensure that instruments onboard the rover and the rover's structure do not go into resonances during operation and cause fatigue failure or give inaccurate readings. Random analysis is used for the rover's operational environment by inputting a vibration magnitude at various frequency ranges to simulate the vibration and loading due to terrain roughness and soil movement. This environment is difficult to predict since many parameters are contributing, such as the rover's configuration, speed, and the terrain.

One criterion the CSA uses to evaluate rovers is the response limits to random vibration in the form of a Power Spectral Density (PSD), this specification limit is given in Figure 1. This graph represents the allowable response PSD, and a rover's response to any given terrain must be contained within these limits. The solid black line is the allowable acceleration response PSD for a payload moving in the vertical, z-axis, direction with the dashed line being the allowable response PSD for the payload in the horizontal, x-y plane. The solid red and blue lines are the PSD response limits in the vertical, z-axis, and horizontal, x-y plane, respectively for the rovers chassis. Currently the only method the CSA uses to evaluate a rover's response PSD is to test a rover in the MET, measure the accelerations, convert the data to a PSD and then compare this against the specification limit in Figure 1. The CSA would like to be able to predict a rover's response through numerical simulation to cut down on the cost and time associated with physical testing, however realistic input spectrums do not currently exist. If input PSDs corresponding to different terrain existed, they could be used along with a finite element (FE) model of the rover to predict the response PSD that could be compared to the exposure limits shown in Figure 1.

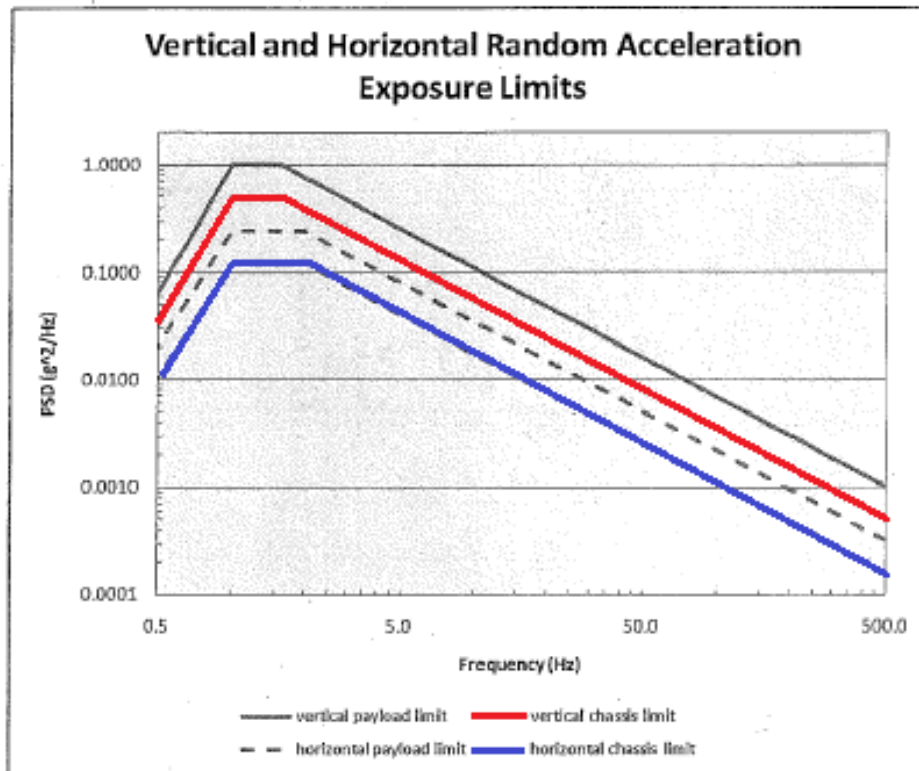


Figure 1: Acceptance Response PSD Level Specification for terrestrial space rovers during operation [5].

1.2. Goals

The main objective of this thesis is to define the random vibration input for a specified terrain from the ground to the rover to use in a vibration analysis of the rover. The input could later be used as a requirement for future rover qualification. It would be ideal to have the input PSD for a given terrain such that the output PSD can be accurately predicted to show that each onboard component is below its given PSD specification limit for random vibration. It would also be beneficial to know whether any section of the rover or its payload would experience resonant frequencies during standard operation.

The ultimate goal for the future would be to take a topology reading from satellite images of a planet's surface in the area that the rover will be exploring and create an input PSD. This would aid in designing the rover's suspension and damping systems to ensure the life of all payloads and the success of a mission. The method presented in this thesis could serve as the basis for this type of detailed input PSD modelling.

1.3. Methodology

The CSA provided raw acceleration data for the wheel mounting locations as it drove through Rock Bed 5(D) in the MET, further detailed in Chapter 3. This acceleration data at the wheels was used to develop the input PSD. The CSA also provided response PSDs generated from field testing at 23 locations on the rover, further detailed in Chapter 3.1. These response PSDs were used for evaluating the effectiveness of the FE model and to verify the generated input PSD.

An Initial FE model with a simplified chassis representation was created and verified by taking the experimental output PSD measured from the main drive shaft and using it directly as an input PSD for the rover model. This Initial model was used to verify the fidelity of the chassis geometry needed to accurately determine the response PSD of the system without the wheels and drive arms of the rover. A more realistic Baseline FE model was then generated to include the drive arms which allowed for the experimental output PSD to be applied as an input at each wheel axle. Once the Baseline FE model was shown to provide acceptable predictions of vibrational response, the raw accelerometer data from the wheel areas were analyzed to determine an input PSD that could be generated directly from the ground in the time domain. Two methods were used to approximate the displacement input from the acceleration; the omega arithmetic method and the double integration method with trapezoidal integration. Input PSDs were generated for accelerometer data and the two sets of displacement data. The FE model's damping value, solver parameters and mesh were refined to predict the response PSD at 1σ and 3σ probabilities of occurrence. The accuracy of the developed input PSD was evaluated by inputting it into the FE model and comparing the 3σ response PSD generated against the CSA's field response PSD at each vertical, z-axis accelerometer.

1.4. Chapter Overview

Chapter 2 outlines the fundamental theory required for vibration analysis and the methods of determining a systems vibration response. This chapter summarizes random vibration analysis using PSDs and the generation of a PSD based on the statistical probability of a response to a given input. Chapter 3 presents the FE model development and the methodology used to determine and generate a suitable input PSD. Chapter 4 provides the verification of the FE model and the validation of the ground input PSD generated for given terrain using three different methodologies. Chapter 5 discusses feasibility of the model, and key findings in constructing a random vibration FE model. Chapter 6 is a conclusion of the methods used to determine a terrain's input PSD and provides areas of future work to improve the accuracy of the models.

2. Literature Review

2.1. Background

When an object is in motion, it is subject to various forces and vibrations due to interactions with the environment around it. For example, a vehicle driving over a certain terrain will have a response that is dependent on the vehicle's natural frequencies as well as the travel speed and road topology. If the natural frequencies and mode shapes are known, the response motion of the object can be determined probabilistically. This probability solution, is how random vibration analyses are performed and is key in scenarios such as cars driving over terrain since it is random loading rather than a sinusoidal loading. This solution is useful when designing a system to ensure that the desired functionality and capability can be met and maintained in a given environment, thus the importance of vibration analysis.

2.1.1. Vibration

In general there are two types of vibration: rigid body vibration and flexible body vibration. Rigid body vibration can be used to analyze single degree of freedom (SDOF) problems such as a simple pendulum or multi degree of freedom (MDOF) problems such as the rover as it drives over terrains at slow speeds using ordinary differential equations (ODE). Flexible body vibration uses partial differential equations (PDE) to describe the motion of items like guitar strings oscillating, as sections of the string move relative to one another and not as a single rigid object. In reality the rover is a combination of rigid and flexible body vibration. At the frequencies below 66Hz the rover will exhibit rigid body vibration, but at frequencies above 66Hz there will be relative movement within the rover structure. The three types of vibrations differ in terms of the corresponding number of mode shapes and type of differential equations used to represent the motion as summarized in Table 2.

Table 2: Vibration systems overview.

Vibration Type	Number of Equations of Motion (EOM)	Number of Natural Frequencies	Number of Mode Shapes	Solution Method
Rigid Body – SDOF	1	1	1	ODE
Rigid Body – MDOF	# DOF	# DOF	# DOF	ODE
Flexible Body	# DOF $\rightarrow \infty$	∞	∞	PDE

In addition to the two types of vibration there are also classes of non-linear and linear vibration. In non-linear vibration there are large displacements and/or the motion is just restricted to oscillation. Random vibration analysis is considered to be linear vibration because stiffness is calculated based on the structure's initial status and does not change throughout the analysis. Linear vibration deals with small oscillating displacements. In general the equation of motion (EOM) for rigid body vibration is given in Equation (1) [6], which is valid for any MDOF, SDOF linear and nonlinear problem.

$$[m]\{\ddot{x}(t)\} + [K]\{x(t)\} = 0 \quad (1)$$

where m is the mass matrix of the system, $x(t)$ is the displacement as a function of time and K is the stiffness matrix for the system.

2.1.1.1. Natural Frequency and Damping

Every system has natural frequencies (f_n), for this work the damping is less than 10% so the damped natural frequency is within 2% of the undamped natural frequency such that the two terms will be used interchangeably. This resonance or natural frequency is the frequency at which a system will oscillate without continuous or repeated external force being added to system. The natural frequency of a system can be defined based on the natural frequency of motion/angular frequency ($\omega_n = 2\pi f_n$), which is for a system without damping. Since in reality all systems have damping, the ODE given in Equation (2) [6] must be used,

$$[m]\{\ddot{x}(t)\} + [c]\{\dot{x}(t)\} + [K]\{x(t)\} = 0 \quad (2)$$

where c is the damping factor. In order to solve the equation, a solution of the form $x = Ae^{st}$ is assumed [2]. The natural frequency of a system with damping can be determined and the ODE solved [6] by the roots of Equation (2) given in Equation (3), where $s_{1,2}$ is the first and second root, ω_n is the undamped natural frequency and ζ is the damping ratio. The damping ratio is defined as $\zeta = \frac{c}{2m\omega_n}$ but this is more commonly written as the ratio between actual and critical damping shown in Equation (4) [7].

$$s_{1,2} = -\zeta\omega_n \pm \omega_n\sqrt{\zeta^2 - 1} \quad (3)$$

$$\zeta = \frac{c}{c_c} \quad (4)$$

Where c_c is the critical damping of the system given in Equation (5) [7].

$$c_c = 2\sqrt{km} \quad (5)$$

There are 3 damping scenarios that will occur based on the value of the damping ratio as summarized in Table 3. The most common is damped oscillations when ζ is between 0 and 1.

Table 3: Effects of damping on a system's step response.

Damping Ratio Value (ζ)	State of System	Graphical Representation [8]
0	Undamped oscillation	
≥ 1	Vibration will not occur	
<1	Damped oscillation	

Knowing that a damping ratio <1 , leads to a decaying oscillation a damped natural frequency (ω_d) can be found using Equation (6).

$$\omega_d = \omega_n \sqrt{1 - \zeta} \quad (6)$$

In most cases when small damping is occurring, the damping ratio is <0.1 (10%) and the damped natural frequency can be approximated as $0.98\omega_n$. Even though the undamped and damped natural frequencies are very similar, the damped natural frequency should be used to avoid a phase error as the oscillation decays. In the case of the rover's analysis the modal analysis produces the undamped natural frequencies. The response to an input vibration has a single constant damping ratio applied to the entire rover as a system. This means the input vibration will be damped as it propagates through the rover.

2.1.2. Modal Analysis

The modes of a system are the characteristic deformation shapes of the system at the different frequencies. When this deformation occurs at the systems natural frequency it is referred to as a normal mode. These normal modes are what are solved for in modal analysis in order to determine a systems natural frequencies

and the given response. In a SDOF system like an ideal string, the modes occur at harmonic frequencies, where a harmonic is the whole-number multiple of the frequencies.

In general the frequencies of the modes have no simple relation to each other, and the vibrating bodies do not have harmonic modes [9]. Referencing a 3D cantilever beam system with a square cross section, shown in Figure 2 the blue represents zero displacement and red represents the most displacement. Modes 1 and 2 are the bending motion of the beam at a natural frequency of 2300Hz, and Mode 3 is the torsional deformation of the beam at 4631Hz. This generic case provides evidence that modes are not generally harmonics in most cases but normal modes provide the characteristic deformation shape of a geometry at its natural frequencies.

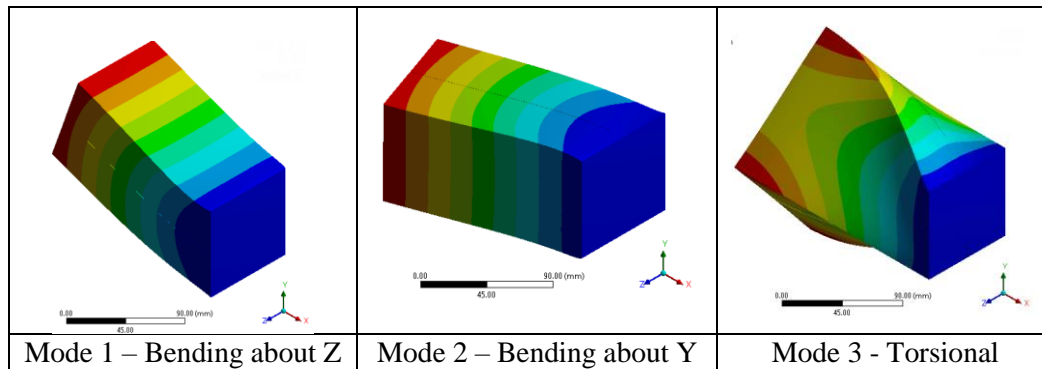


Figure 2: First three modes of a cantilever beam in 3D, with fixed zero DOF end.

2.1.2.1. Modal Super Position to Describe System Vibration

The super positioning of modes for any MDOF system that is lightly damped can describe the total vibration of the system [10]. This method of analysis is useful when looking at the response vibration spectrum, as the peak magnitudes in the spectrums at given frequencies due to the structures geometry can be easily identified. In the context of the rover, this allows for quick differentiation between spectral peaks due to the structures geometry versus spectral peaks due to travelling speeds and rotation of the wheels. Looking at Equation (1), the solution for the vibration displacement of the structure will take the form of Equation (7), where each x_N in the vector is a solution to Equation (2) of the form $x = Ae^{st}$.

$$\{x(t)\} = \begin{Bmatrix} x_1(t) \\ \vdots \\ x_N(t) \end{Bmatrix} = \begin{Bmatrix} a_1 \\ \vdots \\ a_N \end{Bmatrix} \cos(\omega_{n_i}t - \phi_i) \quad (7)$$

The vector $\{a\}$ is a vector of amplitudes/modes for the system, with corresponding natural frequencies ω_{n_i} from i to N . ϕ_i is the phase angle representing the complex number of the vibration and the solution x is for each mode. Substituting $\{x(t)\}$

from Equation (7) into the Equation (2) gives the equation of motion for each mode in terms of the corresponding natural frequency written as Equation (8)a.

$$-\omega^2[m]\{a\} \cos(\omega t - \phi) + [K]\{a\} \cos(\omega t - \phi) = 0 \quad (8)a$$

with the phase angle, $\phi = \omega t$, the EOM can be simplified to Equation (8)b.

$$(-\omega^2[m] + [K])\{a\} = 0 \quad (8)b$$

With Equation (8) the mode shapes of a system can be determined where the trivial solution is $\{a\}=0$, meaning no vibration occurs, or $(-\omega^2[m] + [K])$ equals zero. In order to determine the mode shapes, the determinate of $(-\omega^2[m] + [K])$ must set to zero and solved, as seen in Equation (9):

$$\det(-\omega^2[m] + [K]) = 0 \quad (9)$$

The number of DOF is the same as the number of roots for the determinate [10]. However, it is more convenient to solve for the modes using a computer by rearranging Equation (1) and multiplying through by the mass inverse, where $[A] = [m]^{-1}[K]$ and $[I]$ is the identity matrix, giving:

$$\begin{aligned} -\omega^2[m]\{a\} + [K]\{a\} &= 0 \\ -\omega^2[I]\{a\} + [m]^{-1}[K]\{a\} &= 0 \\ [A]\{a\} = \omega^2[I]\{a\} &= \omega^2\{a\} \end{aligned} \quad (1)a$$

Equation (1)a is now in standard matrix notation and the mode shapes $\{a\}$ and corresponding frequencies (ω) can be solved. The amplitude of each mode is stored in the vector $\{a\}$ at a given frequency (ω) for a known mass (m), knowing the mode shapes $\{a\}$ will provide the systems deformation and the corresponding frequencies. With this information the overlaying of the modes and frequencies can be used to determine a systems response to a given input.

2.1.3. Random Vibration

Random vibration is any form of vibration that is not sinusoidal and is randomized along a frequency band. Random vibration can be analogous to white light. Just as white light can be split into different spectrums of specific wave lengths, random vibration is able to be split into different energy spectrums of specific frequencies known as power spectral densities (PSD), described further in Section 2.2. Random vibration can be stationary such as a component on a shaker table, or nonstationary such as a vehicle driving.

Since random vibration is that, random, the amplitude of the vibration cannot be expressed in terms of a deterministic mathematical function. In other words, the

deformation or response of a structure at a specific point in time cannot be predicted, but the probability that the structure will deform less than a given magnitude can be predicted. Knowledge of the past history of random vibration is adequate enough to predict the probability of occurrence of acceleration and displacement magnitudes for a system in response to the applied vibration input [11]. Understanding this means that random vibration is represented as a statistical analysis with the key characteristics being mean, standard deviation, histogram, and PSD.

The probability that a vibration's amplitude will be less than some value with some degree of certainty is based on the standard deviation (σ) of the normally distributed magnitudes of the vibration. If the data has a mean value of zero, the root mean square (RMS) will be the standard deviation. Figure 3 [12] provides the probability of a vibration amplitude occurring in each standard deviation of the collected time history data shown. If a system is assumed to be linear then the likelihood of a specific response vibration amplitude can be predicted based on this probability. Based on a 3σ value for system response to an input, 99.7% of the true response output would be below or contained in the amplitudes determined. It is important to note that both input and response vibrations have a 0.3% probability that peaks will be greater than 3σ prediction, even in stationary vibration [13]. ANSYS will output the 1σ response with a mean removal, zero mean, to allow the user easy manipulation of the results to meet the safety standard applied.

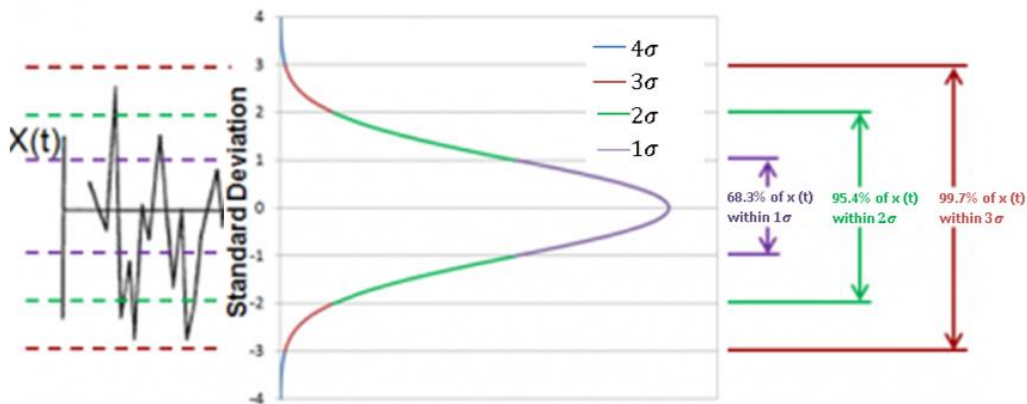


Figure 3: Normal distribution representation of random vibration 3σ includes 99.7% of expected peaks [12].

One special case in random vibration is white noise. White noise is a term used to describe a random signal that has a constant power spectral density over the entire frequency range [13]. In terms of a random vibration, this means the normalized

magnitude of vibration at every frequency is constant. White noise will be used in later analysis to represent stochastic vibration on given geometries, to see the effects of geometry impact when pure random vibration is applied.

2.2. PSD

2.2.1. PSD – Definition

Random vibration can be represented as a power spectral density (PSD). A PSD is a method of overlaying data, in this case vibration data, and comparing it independently of its spectral resolution by normalizing the amplitude of the vibration by the frequency resolution. Where the frequency resolution is the ability to distinguish smaller frequency bands from each other. When determining the PSD, the Fourier Transform (FT) of the time history data is required. To understand the effects of resolution consider 3 different resolutions 1Hz, 4Hz and 8Hz. When the FT is taken, the amplitude output graphs have varying orders of magnitudes relative to one another but carry the same trends. Despite the peaks in the higher resolution data being much lower than the peaks of the coarse resolution data the RMS, or total area under the curve would be the same. By normalizing the magnitudes of vibration about the frequency resolution each will be resolved to have similar amplitudes. The 1Hz PSD would remain the same as the FT but, the 4 and 8Hz PSD would be a factor of 4 and 8 reduction of amplitude at each frequency [14]. Figure 4 depicts how the higher resolution data 8Hz has lower amplitude range, similarly for the 4Hz resolution. However, despite the amplitude changes the total area under the curve remains constant.

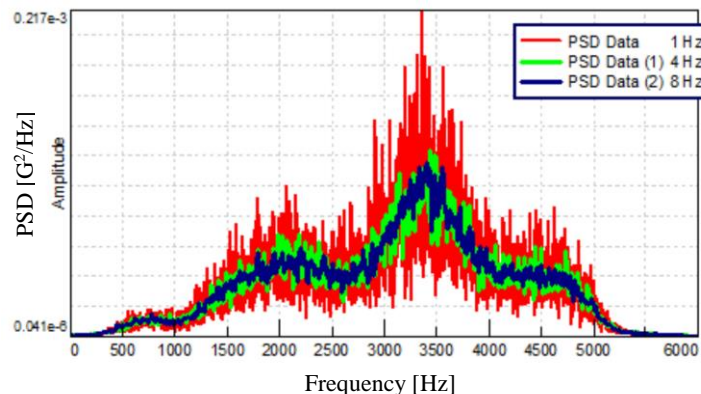


Figure 4: PSDs of identical broadband data measured with 1 Hz spectral resolution (red), 4 Hz spectral resolution (green) and 8 Hz spectral resolution (blue) , showing trend and amplitude differences [14]

2.2.2. PSD Generation

In general there are 3 methods to calculate the PSD from a time history [15,16]:

1. Measure the RMS value in successive frequency bands through the use of a band pass filter
2. Wiener-Khintchine approach of taking the FT of an autocorrelation function
3. Taking the limit of the FT multiplied by its complex conjugate and dividing by the period as it approaches infinity

Method 1 is a field test and iteration approach which is not practical in most applications or for the purpose of this research because this would require multiple field runs of the rover with identical setup, and completing a convergence test of sensor resolutions until the Fast Fourier Transform (FFT) of the vibration was nearly identical. This is currently how the CSA is testing rovers and determining the response PSD. Method 2 uses the Wiener-Khintchine theorem which states that for a continuous time, if x is a wide-sense stationary random process and that the autocorrelation function is defined with a statistical expected value then a function exists in the frequency domain such that it is the power spectral density [17, 18]. This method is using the unique case of the cross correlation theorem. This is a mathematical technique of seeing the correlation between two random series. The Wiener-Khintchine theorem is using the special case of when series' are equal to each other, referred to as autocorrelation. Autocorrelation is used when a time lag is applied to a series and then copied onto itself to look for patterns that are masked by noise. If the FT of a signals autocorrelation is taken it produces the PSD of the series and likewise if the inverse FT of a PSD is take the series autocorrelation function is formed [17, 18]. This method of analysis to resolve the PSD is a highly mathematical approach that is not suitable for practical engineering.

Focusing on method 3, the double sided and one sided equations are shown in Equations (10) and (11) [15, 16], respectively, where the difference is such that the double sided is mirrored about the Nyquist frequency (half the sample rate). Alternatively, a one-sided PSD contains the total signal power in half the Nyquist interval [19]. Considering the use of complex numbers and the real number counterparts such as $e^{i\omega_0 t}$ and $\cos(\omega_0 t)$, the same power is spread in the real-signal case over positive and negative frequencies which is half as large as the complex spectrum. The one sided PSD of the signal represented as a complex number would be $\delta(\omega - \omega_0)$ and for the signal represented as a real number would be $\frac{1}{2}[\delta(\omega - \omega_0) + \delta(\omega + \omega_0)]$.

$$X_{PSD}(f) = \lim_{T \rightarrow \infty} \frac{X(f)X^*(f)}{T} \quad (10)$$

$X(f)$ is the FT with dimensions of amplitude-time and is double sided.

$$\hat{X}_{PSD}(f) = \lim_{\Delta f \rightarrow 0} \frac{G(f)G^*(f)}{\Delta f} \quad (11)$$

$G(f)$ is the FT with dimensions of amplitude, is single sided, and has been converted to RMS by dividing through by $\sqrt{2}$, thus denoting $\hat{X}_{PSD}(f)$ as a single sided PSD. It is important to note that when creating a PSD it is acceptable to allow $\Delta f \neq 0$, for relatively low frequencies sometimes up to 20Hz depending on the application based on the cut off frequency used to remove noise from the system.

2.2.2.1. PSD Generation from Complex Conjugate

As discussed in Section 2.2.1 method 3, which uses the complex conjugate, it is the most practical approach to solving for a PSD to represent a vibration spectrum. This method can be rewritten as Equation (12) [16] and is a common engineering method for determining the PSD for a given vibration.

$$PSD(f) = \lim_{\Delta f \rightarrow 0} \frac{\Delta(\bar{x}^2)}{\Delta f} \quad (12)$$

$\Delta(\bar{x}^2)$ is the filtered mean square, filtered by FT or FFT, and Δf is the frequency resolution. Equation (12) [16] calculates the PSD by taking the limit of the FT of the vibration magnitude in displacement, velocity or acceleration, and multiplies by its complex conjugate and divides through by its period as the period approaches infinity. This has units of magnitude squared per hertz. The unit is one over the frequency resolution the magnitude has been normalized over.

A PSD is calculated from a FT or FFT, but has the advantage of being independent of the time duration of the sample. An FT or FFT representation of the vibration assumes an infinite time of sampling and is not normalized to the frequency resolution and is therefore influenced by the time duration of the time history sample with the number of spectral lines influencing the response.

Since a PSD provides the normalized magnitude of vibration, the vibration's phase information is lost. In modal analyses and when reverse engineering an exact input vibration spectrum the phase information is required. Since the phase information is discarded, the same input or output PSD could represent several different series' of vibration hence the probability of vibration amplitudes is all that can be deduced. It would be possible to see a frequency peak at 10Hz from a PSD but without the raw time history data it cannot be said that this peak happened at 10sec

or 100sec into the sample time whereas with an FT or FFT you could compute the inverse and all complex numbers would give you the specific phase of the vibration at a given time.

2.2.2.2. Welch Method

The Welch method, also known as the weighted overlapped segment averaging (WOSA) method is a common method of analytically generating a PSD [20]. The Welch method has been used to represent the PSD of a time history since 1961 when introduced by Peter Welch, however it was not until the paper in 1967 "*The Use of Fast Fourier Transform for the Estimation of Power Spectra: A Method Based on Time Averaging Over Short, Modified Periodograms*" that the FFT was included. Since this time it has been used widely and has been the primary method to produce PSDs in MatLab since before 2006. This method splits data into L overlapping segments each of length M, with S number of points in each segmented length. When S = 0.5M this implies there is 50% overlapping of the segments M. This new data set composed of overlapping segments is referred to as a periodogram. A modified periodogram is generated by computing the discrete Fourier transform (DFT) with a windowing method such as rectangular or Hanning, which is further described in 2.2.3.1. The resultant of the RMS of the modified periodogram is the PSD shown in Equation (13) [20].

$$\hat{X}_{PSD}(f) = \frac{1}{L} \sum_{l=0}^{L-1} \frac{1}{S} \left(\sum_m x[m](w[m]) e^{-j2\pi \frac{i}{M}} \right) \quad (13)$$

Where $m = (l - 1)S, \dots, M + (l - 1)S - 1$ for each segment $l = 1$ to L with a windowing function $w[m]$ in this case Hanning windowing and $-\left(\frac{M}{2} - 1\right) \leq i \leq \left(\frac{M}{2}\right)$ [20]

2.2.2.3. PSD Refinement

When creating a PSD from time history data it is important to consider the reliability of the PSD, which is proportional to the statistical DOF [15]. The higher the DOF the more reliable the PSD. The statistical DOF is linked to the Δf of the system where Δf is considered the frequency resolution, and defined in Equation (14) [15, 21].

$$\Delta f = \frac{1}{T} \text{ where } T = N\Delta t \quad (14)$$

Recalling N is the number of samples (data points collected) and Δt is the time separation of the samples. With this knowledge, the statistical DOF can be defined as Equation (15) [15, 22-24].

$$S_{DOF} = 2BT \quad (15)$$

If an ideal rectangular filter is implemented then half of the data ($N/2$) will remain, giving $B = \Delta f$, so that BT is a unity gain giving 2 DOF as the input and response are the same having a gain of 1. This total time history can then be subdivided with each subdivision or record having 2 DOF, thus widening the frequency resolution of the entire time history and improving the overall DOF to twice the number of individual records. This increases the reliability of the PSD. The risk with this is that narrow peaks can become smeared as the resolution is widened [15, 22-24]. Based on the frequency resolution required this trade off needs to be considered. The effects can be mitigated by windowing, as well as the number of records and sampling rate chosen to analyze a given time history. Details on each of these topics are outlined in Section 2.2.3, Analyzing Time History Data.

2.2.3. Analyzing Time History Data

In order to generate a PSD, a time history of empirical or simulated data is required. A time history can be changed to the frequency domain and then an input PSD can be created to show the magnitude of vibration at each frequency band. When creating a PSD, windowing, cut off frequency and the number of samples in the vibration time history are the most important aspects to consider. This vibration magnitude input can be used to then simulate different conditions and to determine a systems response PSD. Alternatively the vibration response of a system can be measured for a given time history to see if the response PSD falls within a product specification limit, like that shown in Figure 1. When collecting time history data, it is required that the sampling rate must be more than two times the analysis frequency [25-27], and the sampling rate must be greater than the maximum frequency present in the input PSD. The maximum of the input PSD is typically not known and is independent of the maximum analysis frequency, therefore in most cases is taken from a low-pass anti-aliasing filter at or near the maximum analysis frequency [25]. Both sampling rules are used to avoid aliasing, when signals are masked as other signals out of phase, based on Shannon's Theorem. This theorem states the minimum sampling rate to avoid aliasing is defined as a frequency above one half the sample's peak frequency. This is so that the collected sample does not have any signal loss and the so the signal is not being reintroduced and super imposed upon itself by folding about the Nyquist. One half of the samples peak frequency is defined as the Nyquist frequency [28]. This can be simply stated by Shannon's sampling theorem in Equation (16) [25-27] and Equation (17) [25].

$$\min(\text{sample rate}) \geq W * \max(\text{Analysis Frequency}) \quad (16)$$

$$\min(\text{sample rate}) \geq M * \max(\text{Input PSD}) \quad (17)$$

For Equation (16) it is suggested by Shannon that W is 2 for the frequency domain and 10 for the time domain [28]. Although a higher sampling rate is better, an excessive sample rate will generate enormous data sets such that the analysis can become computationally cumbersome. Shannon suggested a value of $W = 2$, while Irvine considered $W = 3.3$ to be a conservative and safe approach [25]. For Equation (17) guideline values in the frequency domain of $M=2$ and in the time domain of $M=10$ are from the Institute of Environmental Sciences and Technology (IEST) [25, 29].

The impact of aliasing can be seen in the following examples shown in Figure 5 through Figure 7, where 200Hz and 1800Hz sine functions are sampled at 2000Hz thus the Nyquist is 1000Hz. In the 200Hz function there are 10 sample points per period which is considered adequate for a sine function to be characterized, but in the 1800Hz function there are only 1.11 points per period. Taking the Fourier magnitude of both cases the 200Hz function will have a spectral spike at 200Hz as expected but, the 1800Hz signal will also have the spectral peak at 200Hz due to aliasing and a fold about the Nyquist, as shown in Figure 8. This becomes apparent when overlaying the signals at the 2000Hz sampling rate because the two signals appear the same disregarding the phase angle, as shown in Figure 7. This example highlights the importance of having a high enough sampling rate to correctly predict the spectral peaks when performing an analysis on time-history data

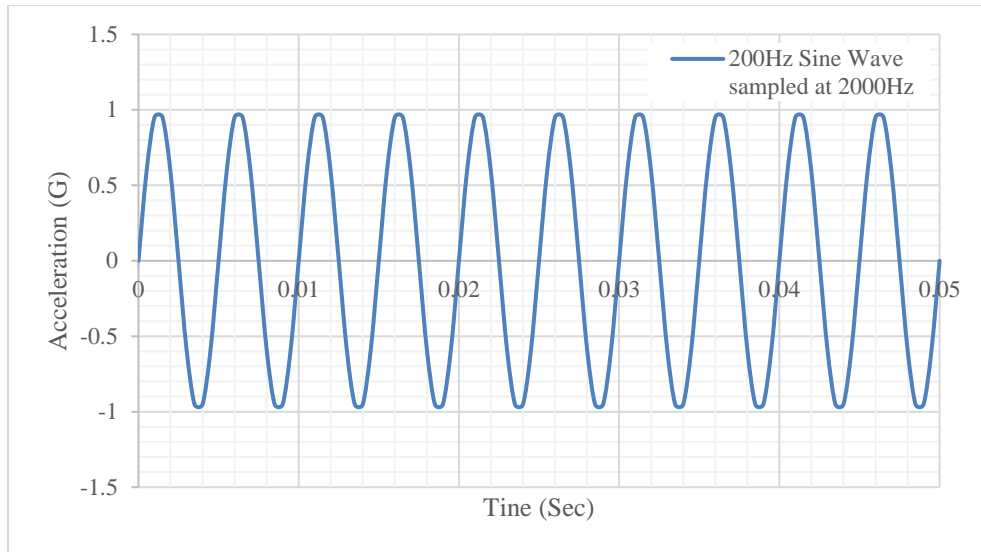


Figure 5: Example of a 200Hz sine function sampled at 2000Hz.

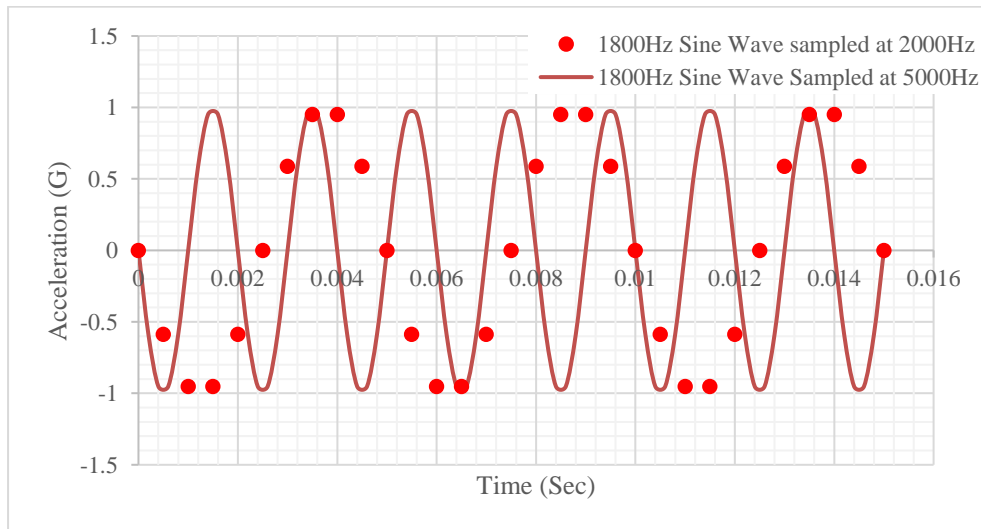


Figure 6: 1800Hz sine function sampled at 2000Hz.

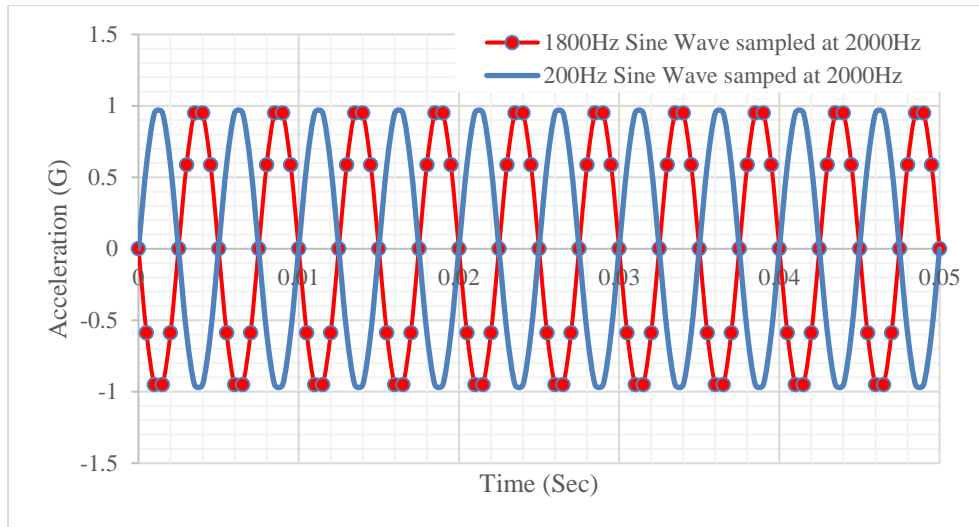


Figure 7: Aliasing overlay of 200Hz and 1800Hz signals samples at 2000Hz, signals are seen as identical with 180° phase shift.

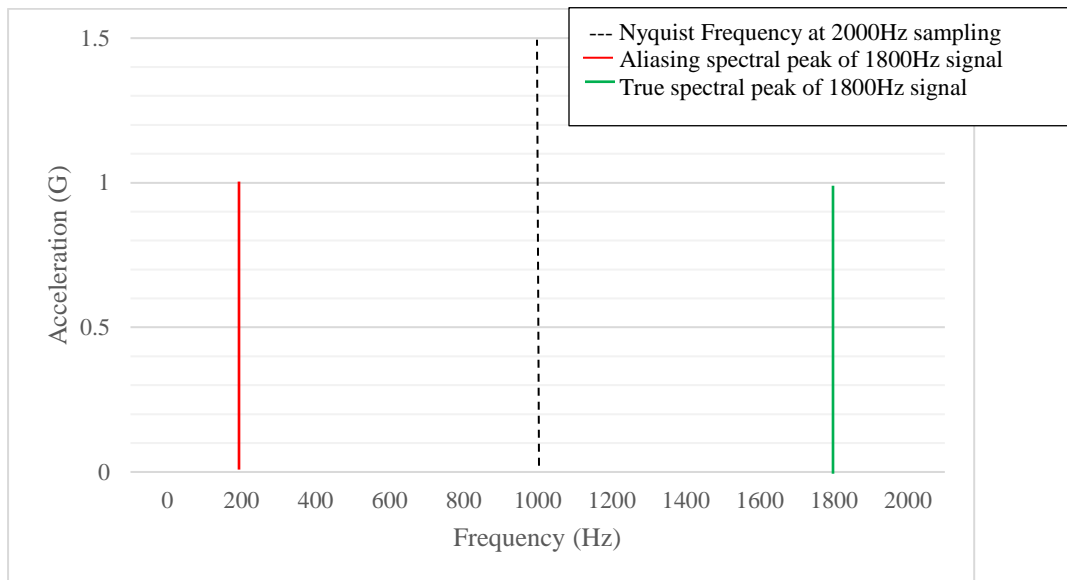


Figure 8: Fourier transform of 1800Hz signal sampled at 2000Hz showing a spectral peak at 200Hz due to aliasing

2.2.3.1. Leakage and Windowing

Another important topic in analyzing a time history in order to shift into the frequency domain and in creating PSDs is the topic of leakage, to ensure the energy inputs correctly correspond to the vibration inputs. When performing a FT, one of the errors induced is the smearing of energy throughout the frequency domain, this is what is referred to as leakage. Leakage occurs when the signal is taken over a finite time record, and the signal is non-periodic in a time record [30], as is the case in random vibration analysis.

A FT will assume the same signal continues forever so if a poor acquisition is completed the signal will be completely distorted. For instance a perfect sine wave sampled across its period will have a single spectral peak as seen in Figure 9. A poorly sampled signal is seen in Figure 10 and will have spectral smearing based on a non-integer sampling. These spectrums are for the same signal, but appear very different due to leakage. The true peak at 1Hz is not evident in the second sampling because the energy is smeared about the true 1Hz peak.

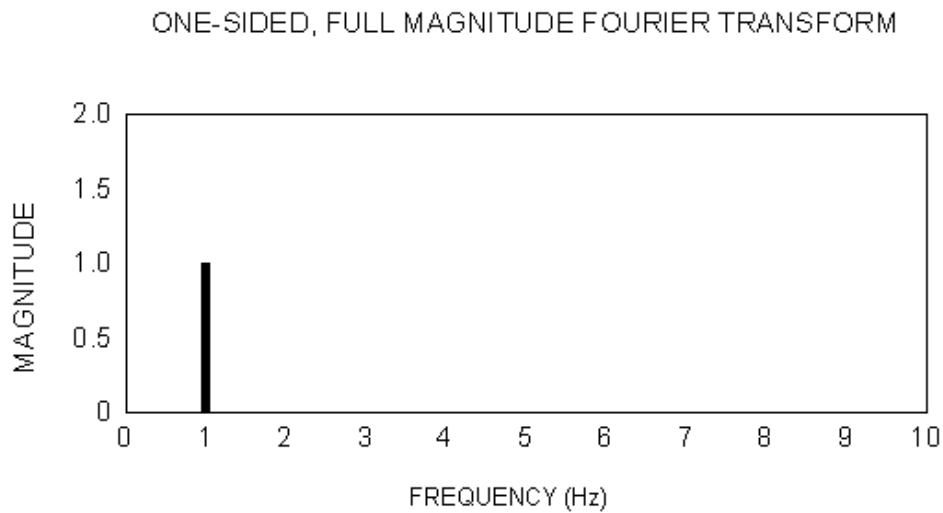


Figure 9: FT of well acquired signal giving spectral peak at 1Hz [30].

ONE-SIDED, FULL MAGNITUDE FOURIER TRANSFORM

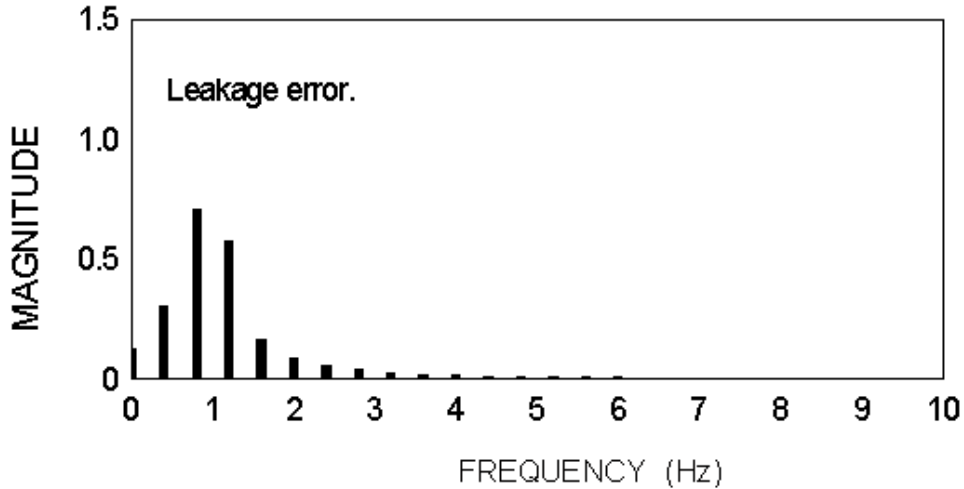


Figure 10: FT of poorly acquired signal with leakage about the 1Hz peak [30].

Leakage can be overcome through the use of windowing. This is where signal is broken into smaller windows and each window of data is overlapped upon itself to give a better representation of the true data. Two common methods are rectangular windowing and Hanning windowing. In rectangular windowing the data is left unmodified, whereas Hanning tapers the time history data so that the amplitude envelope decreases to zero at both the beginning and end of the time window [30]. The Hanning window is defined as $w(t)$ in Equation (18) [30].

$$w(t) = \begin{cases} 1 - \cos^2\left(\pi \frac{t}{T}\right), & 0 \leq t \leq T \\ 0, & \text{elsewhere} \end{cases} \quad (18)$$

Using windowing methods and analyzing the same time history at the non-integer acquisition from Figure 11, the spectral peak at 1Hz is evident, however, there still is some leakage as seen in Figure 11. Irvine's work shows the peak is seen at 0.945Hz with rectangular windowing and 1.05Hz with Hanning [30].

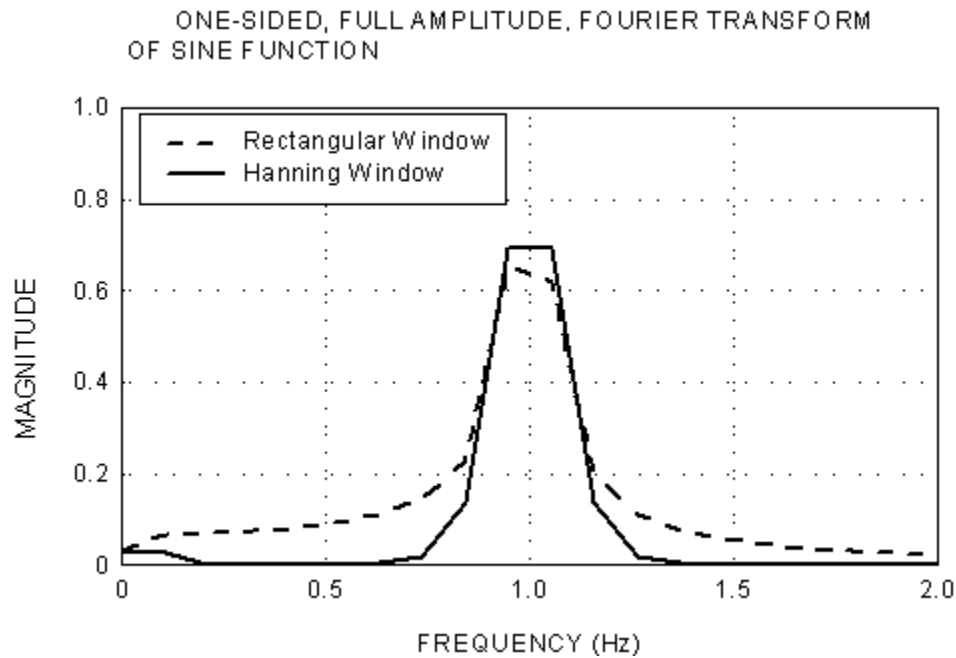
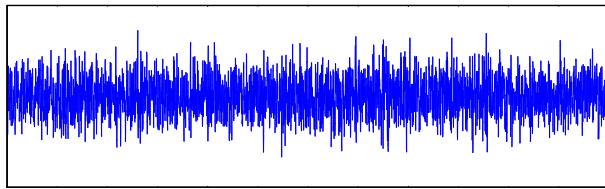
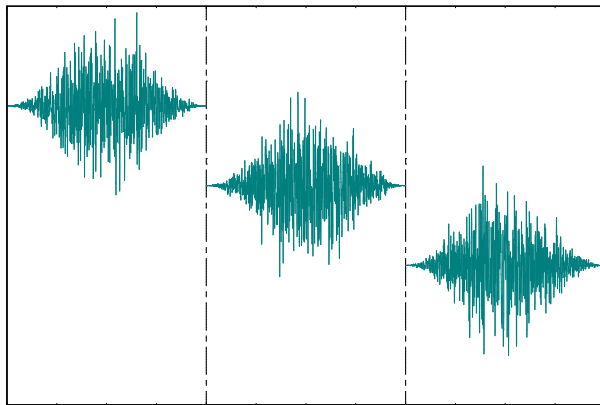


Figure 11: Implementation of windowing on time history to reduce leakage about the 1Hz spectral peak [30].

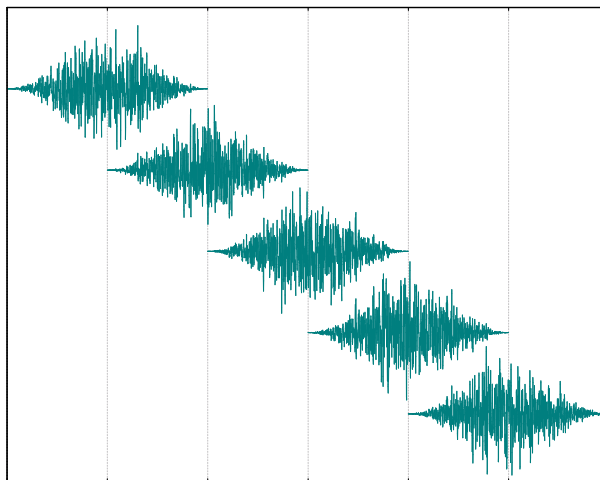
The use of windowing again is critical in evaluating time histories and creating reliable PSDs. As previously stated in Section 2.2.2.3, PSD Refinement, the more statistical DOFs the more reliable the PSD, although smearing begins to occur. To reduce this smearing from leakage, Hanning windowing can be applied to the time history. The use of windowing does come with its own penalties as some statistical DOF are lost and some data is lost [30], as illustrated in **Figure 12**. With the use of a Hanning window and 50% overlapping, approximately 90% of the statistical DOFs are recovered [15, 24] giving a reliable and accurate PSD based on time history data.



Original Time History



Segmented Time History Records with Hanning Window applied and no overlapping



Segmented Time History Records with Hanning Window applied and 50% overlapping

Figure 12: Windowing of time history segments, with no overlapping data is lost, with 50% overlapping 90% of time history is recovered and leakage minimized [15].

2.2.3.2. Displacement Time Histories

Often time series data is given in the form of acceleration per time based on the common practice of using accelerometers to collect data. However, there are instances where a velocity or displacement time series may be better suited. In the case of this research a displacement time series or displacement frequency series is the goal so that an input PSD directly from ground displacement data can be created. In other areas of research such as fatigue analysis due to random vibration the velocity time history is important. This research will focus on deriving a displacement time history so that a displacement PSD can be generated.

2.2.3.2.1. Integration

The first method to obtain a displacement time history from an acceleration time history is via integration, using a method such as trapezoidal integration. Historically it has been shown that direct integration can cause unrealistic drifts in the derived displacement [31]. In order to correct these drifts filtering and windowing must be implemented. The inherent relationships between acceleration and displacement is the starting point for this analysis, shown in Equations (19) - (22). Equation (19) determines the velocity from the integral of acceleration and then Equation (20) provides the displacement from the integral of velocity. Equation (21) and (22) are the discrete forms of the velocity and displacement determined using the trapezoidal integration.

$$\dot{x}(t) = \int_0^t \ddot{x}(t) dt \quad (19)$$

$$x(t) = \int_0^t \dot{x}(t) dt \quad (20)$$

$$\dot{x}(t) = \sum_{i=1}^N \frac{1}{2} (\ddot{x}(i-1) + \ddot{x}(i)) \Delta t \quad (21) \quad x(t) = \sum_{i=1}^N \frac{1}{2} (\dot{x}(i-1) + \dot{x}(i)) \Delta t \quad (22)$$

There are various methods used to correct the time history data as it is integrated such as work done by Boyce [32], Trifunac [33], Trujillo and Carter [34], Zhou [35], and Iwan [36]. For this research the Trifunac scheme was used, as this scheme has been developed as a standard procedure of strong motion data processing [37]. This is a processing scheme that uses multiple baseline corrections and high-pass filtering of the acceleration and velocity time series, which was shown to be largely independent of the sample length [31]. Using this knowledge, the following steps can be taken to determine the displacement time history from acceleration time history:

1. If the data does not have a mean value of zero a mean removal/shift is required

2. Use a high-pass filter such as a 6th order Butterworth filter used in this research with a cut off frequency to eliminate the noise in the acceleration time history
3. Integrate once to obtain velocity using the trapezoid rule as given in Equation (21)
4. Use a high-pass filter such as a 6th order Butterworth filter used in this research with the same cut off frequency to eliminate the noise in the generated velocity time history
5. Integrate again to obtain displacement, using Equation (22)
6. Detrend and perform mean removal of the data to eliminate the drift in the final displacement time history.

This displacement time history is then input into Equation (11) to effectively create a displacement PSD. This method of determining a displacement time history is sometimes referred to as the Double Integration Method.

2.2.3.2.2. Omega Arithmetic Method

The Omega Arithmetic method is another method to achieve displacement data given acceleration data. With this method either the frequency domain or the spectral density can be utilized. This method is referred to as the omega arithmetic version simply because the angular frequency denoted in Equation (23), is defined by the Greek symbol omega [38].

$$\omega = 2\pi f \quad (23)$$

If a simple sine wave is considered to represent the vibration then the following governing equations are obtained for displacement, velocity and acceleration, respectably, starting with a sine function where A is based on initial conditions.

$$x = A\sin(\omega t) \quad (24)$$

$$\dot{x} = -\omega A\cos(\omega t) \quad (25)$$

$$\ddot{x} = -\omega^2 x \quad (26)$$

Using Equations (24) to (26) as a base foundation for motion in a vibration analysis, a more rigorous approach can be taken in the frequency domain as seen in Equation (27) for velocity and Equation (28) for displacement [38, 39]. These equations represent the displacement and velocity in the frequency domain as a function of acceleration, and formally any signal can be represented exactly by its FT [38]. Thus these can be extended to random vibration and represented as Equation (27) and Equation (28).

$$\dot{X}(f) = \frac{\ddot{X}(f)}{j\omega} \quad (27)$$

$$X(f) = \frac{\ddot{X}(f)}{-\omega^2} \quad (28)$$

Low frequencies are a challenge with this method, because the angular frequency is in the denominator of Equation (28) and as frequency approaches zero $\dot{X}(f)$ and $X(f)$ become indeterminate. The lower cut off frequency (f_{cut}) is therefore important, and depending on the case, f_{cut} can range from 5-500Hz [40, 41] based on the sample frequency and the motion of interest. If the motion of interest is low frequency whole body dynamics then direct integration as described in Section 2.2.3.2.1 Integration is needed. Using direct integration at low frequencies results in the least error [38]. The following steps are used to determine the displacement time history from acceleration time history using the omega method:

1. If the data does not have a mean value of zero a mean removal/shift is required
2. Take the FFT of the acceleration time history
3. Convert the transformed acceleration to displacement data by dividing each element by $-\omega^2$, where omega is the frequency band
4. Take the inverse FFT to return to the time-domain
5. Detrend and perform mean removal of the data to eliminate the drift in the final displacement time history

This displacement time history is then input into Equation (11) to effectively create a displacement PSD. The transformations for the frequency and spectral domains are summarized in Table 4 and Table 5 respectively.

Table 4: Fourier transform Omega Arithmetic [38, 41].

Input	Output		
	$X(f)$	$\dot{X}(f)$	$\ddot{X}(f)$
$X(f)$	1	$\frac{1}{j\omega}$	$-\frac{1}{j\omega}$
$\dot{X}(f)$	$j\omega$	1	$\frac{1}{j\omega}$
$\ddot{X}(f)$	$-\omega^2$	$j\omega$	1

Table 5: Spectral density Omega Arithmetic [38, 41].

Input	Output		
	X_{PSD}	\dot{X}_{PSD}	\ddot{X}_{PSD}
X_{PSD}	1	$-\frac{1}{\omega^2}$	$\frac{1}{\omega^4}$
\dot{X}_{PSD}	$-\omega^2$	1	$-\frac{1}{\omega^2}$
\ddot{X}_{PSD}	$-\omega^4$	$-\omega^2$	1

2.3. Modelling Vibration

2.3.1. Analysis Type

Vibration can be analyzed as harmonic or random vibration, in both cases the same governing equation, Equation (2), applies. However the solutions are approached in a different manner. In a harmonic analysis an exact solution can be analytically determined whereas in a random vibration analysis only the probability to some statistical certainty can be solved for. The restrictions to a harmonic analysis are that the entire structure is given constant or frequency-dependent stiffness, damping, and mass effects. This means the stiffness of the structure will not change from initial conditions throughout the analysis. The entire analysis is assumed linear and transient effects cannot be determined. Lastly all acceleration, bearing and moment loading are assumed in phase and real. All other loading cases and displacements in a harmonic analysis vary sinusoidally at the same given frequency but are not required to be in phase [42].

The two methods of performing a harmonic analysis are a full harmonic response or modal super positioning [42]. When solving for a full harmonic response, FE software will use a static solver following Equation (29), where $\{F\}$ is the resulting

force and $\{x\}$ is the output displacement, both are harmonic with the input frequency.

$$\{F\} = [K] \{x\} \quad (29)$$

The method of modal super position can be understood by reviewing Section 2.1.2.1 Modal Super Position to Describe System Vibration. This is where the response is expressed in linear combinations of each mode shape. In the solver the modes are normalized to the mass matrix of the structure thus Equation (1)a applies, and then the summation of all modes is completed to determine the final output of the entire structure. An example of this is given in Figure 13, where the summation of shapes 1 through 3 produce the final resulting shape.

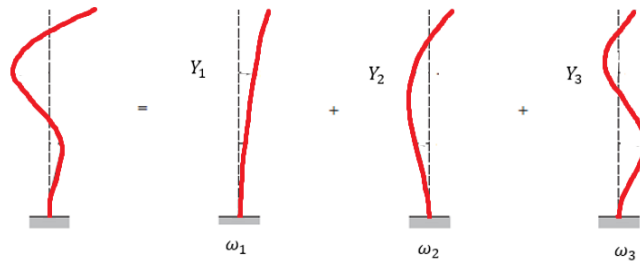


Figure 13: Modal super position of 3 mode system providing full system deformation.

In a random vibration analysis such as a component subjected to white noise, or a vehicle driving over a wash board road the input and outputs cannot be determined as easily as harmonic situations. In order to characterize random vibration it must be represented as a PSD where the total frequency range is split into individual ranges or bins [43]. The restrictions to a random vibration analysis are that the structure has no random properties. For example, the stiffness, damping and mass do not vary with time, nor do any forces, displacement conditions, pressures, or temperatures. Lastly the damping is lighter/less than the inertial and elastic forces [43]. In ANSYS a modal analysis is required to perform a random vibration analysis as this predicts the natural frequencies of the structure. To determine the rover's interaction with the terrain, the displacement or acceleration time histories are needed. Then an input PSD is generated and properly windowed to retain vibration magnitudes. The response PSD to 1σ can be determined through the FE simulation.

Since the FE software outputs a response PSD of 1σ and a mean removal is completed automatically, the 3σ response can easily be determined by multiplying

the results by three. The true field response of a structure can be approximated as being within or under this energy band at a given frequency in the 99.7 percentile. It should be noted though that there is a 0.3% probability of occurrence exceeding the calculated response in field with structures that will be regularly introduced to random vibration. Since the 3σ value will be exceeded at some point, a factor of safety should be applied. A more conservative approximation for determining the maximum response amplitude of the PSD would be to determine the crest factor (CF).

The CF is the absolute highest PSD value divided by the 1σ PSD and can be determined directly from the PSD with Equation (30). For a SDOF system, the Rayleigh distribution can be used to determine the CF as shown in Equation (31) [44, 45].

$$CF = \frac{\text{Peak Absolute of } PSD_{\text{response}}}{1\sigma \text{ of } PSD_{\text{response}}} \quad (30)$$

$$CF_{\text{approx}} = \sqrt{2\ln(f_n T)} + \frac{0.5772}{\sqrt{2\ln(f_n T)}} \quad (31)$$

2.3.2. Performing and Interpreting Structural Dynamic Analyses

Most often, physically measured data is used for performing a vibration or a dynamic analysis. This data can be collected in the form of displacement, velocity or acceleration, but could also be collected as strain information. The most common method for quantifying vibration or dynamic motion is with an accelerometer. These accelerometers can be piezoelectric, piezoresistive or variable capacitance [41]. All of the rover's motions were recorded using piezoelectric accelerometers.

As briefly discussed in Section 2.2.3.1 Leakage and Windowing, velocity data is better for fatigue analysis due to vibration as it was found by Gaberson, that dynamic stress is directly proportional to modal velocity [46]. Velocity measurements can be taken with a Doppler laser or geophone, but lasers can be costly and the geophone is not practical for vibration analysis of systems like the rover because of its size. A geophone is typically used in seismic measurements [41]. Displacement data can be measured directly with a Linear Variable Differential Transformer (LVDT) which can use contact, probe, or non-contact lasers or sensors.

2.3.2.1. Interpreting Response PSD

Looking at Figure 14 from Irvine's work the root mean square of the area under the PSD (GRMS, Gravitational Root Means Square) of a structures response to a $6.06 \frac{G^2}{Hz}$ input is $11.2 \frac{G^2}{Hz}$, when the quality factor $Q=10$, which is equivalent to 5% damping. The 3σ or maximum expected peak is $33.6 \frac{G^2}{Hz}$ but, when using a Rayleigh distribution the true expected peak is at 4.47σ correlating to $49.9 \frac{G^2}{Hz}$ [41]. This same peak error translates in the velocity and displacement outputs as seen in Table 6, where the maximum expected is determined at 4.47σ . In each case that is an approximately 40% increase in the maximum case versus the assumed maximum from just reviewing the 3σ values as peak. This is critical in considering the rover's design as using 3σ could lead to premature failure of the rover during the mission, so the rover's should be more than 3σ below the CSA limits outline in Figure 1.

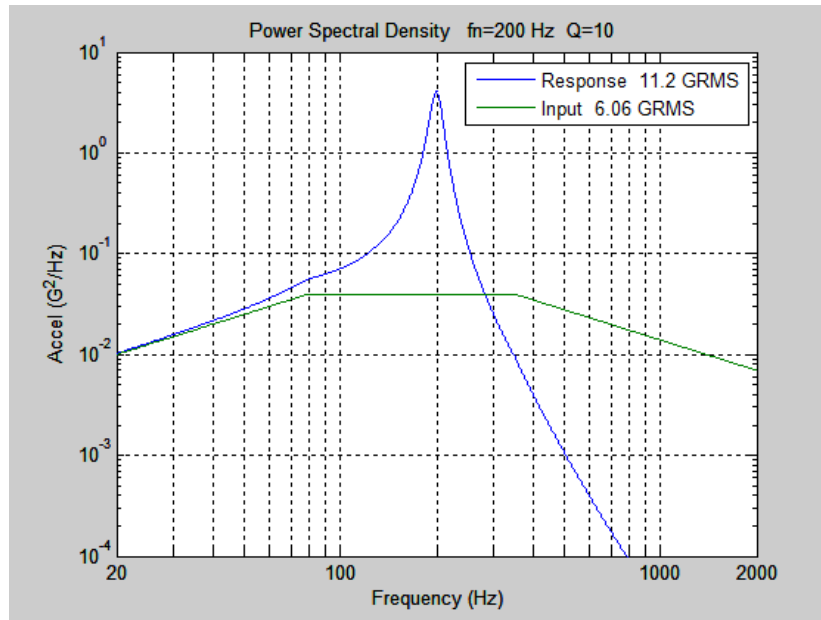


Figure 14: Response PSD from NAVMAT P-9492 input PSD specification [41].

Table 6: Peak output from PSD NAVMAT [41].

Output PSD Type [RMS]	3σ	Maximum from Rayleigh Distribution
Acceleration [G]	33.5	49.9
Velocity [m/s]	0.259	0.388
Displacement [mm]	0.207	0.307

Figure 14 can be used to demonstrate three distinct regions of a PSD; unity gain, excitation to a natural frequency and attenuation. On the first 3dB rise there is unity gain, meaning the input spectrum and output spectrum are equal resulting in a gain of 1. Then there is a rise to the structures natural frequency at 200Hz, followed by attenuation, or damping of the output spectrum as the response has a lower magnitude than the input. The point of cross over from the output excitation to attenuation can be defined by Equation (32) for a SDOF system.

$$Intersection = f_n \sqrt{2} \quad (32)$$

2.3.2.2. Analyzing PSD Curves for Dynamic Motion

When scrutinizing a PSD there are distinct spectral peaks at each mode of the structure. This section reviews dynamic testing performed by Irvine [47] on a vehicle using a single accelerometer to generate the response PSD as it was driven at 105km/hr (29166.7 mm/sec) for a 10s duration. Figure 15 shows the response PSD generated with distinct peaks noted at 1.5Hz, 14.65Hz, and 29.3Hz.

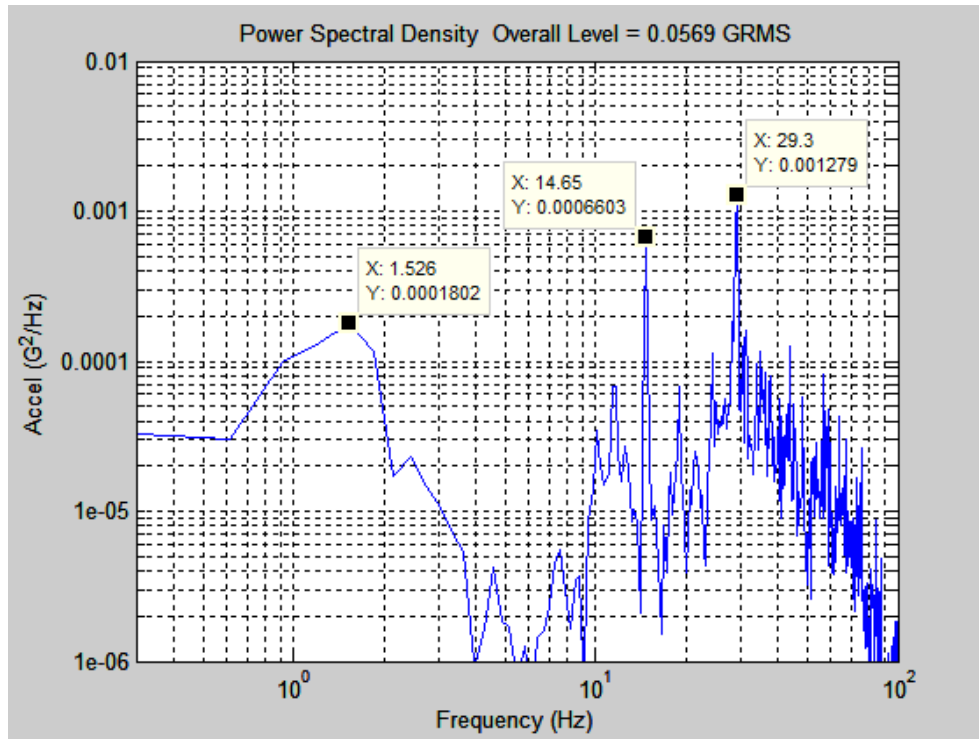


Figure 15: Vehicle response PSD, highlighting three spectral peaks due to input PSD [47].

The first low frequency is considered the fundamental frequency of the vehicle, which is the full body motion. Typical values for vehicles are summarized in Table 7, and are affected by the suspension system of the vehicle. Since Juno does not have a spring damping system for suspension, it has rigid wheels and drive arms locked to the chassis, it is expected that its fundamental frequency will be much higher than a typical vehicle.

Table 7: Automobile natural frequencies [47].

Vehicle	Fundamental Frequency
Passenger Car	1 to 1.5 Hz
Sports Car	2 to 2.5 Hz
Hummer	4.5 Hz

The second peak is the tire imbalance frequency:

Tire diameter = 635mm

$$C_{tire} = \pi 25 = 1994\text{mm}$$

$$f = \frac{\text{Vehicle Velocity}}{C_{tire}} = \frac{29166.7[\frac{mm}{s}]}{1994[\text{mm}]} = 14.6\text{Hz}$$

That means these spectral peaks would be directly impacted by the vehicles speed, and tire selection. This same analysis can be performed on Juno to see which response excitations are speed dependent. The third peak is the second harmonic of the second peak, since it is exactly two times the frequency.

2.3.3. Testing Standards

Figure 16 is an example of a test specification in the form of a PSD. When evaluating the design of a structure or system's response to an input PSD the response must be a PSD value below the curve. It can be seen that the starting frequency of the specification is 20Hz, as this was chosen to be the lower cut off frequency so that data below this response frequency was ignored. Cut off frequencies are used because at the low frequencies there is potential for very high displacements and noise being induced based on the FFT of the data. The overall RMS of the system is typically an overall acceleration in gravitational units (G) expressed as GRMS. This is the square root of the area under the curve; however simple geometry relationships cannot typically be used as the standard format of a PSD plot is a log-log format, as shown in Figure 16. The overall GRMS is the total response vibration the system will see and what the system will need to be less than the structures limits. The magnitudes of the response PSD (y-axis Figure 16) do not directly give the acceleration at a specific frequency, but they are used to give an idea of which frequencies will have higher accelerations. These response PSDs are directly compared to the limits such as Figure 16, to ensure a system can handle given input vibrations.

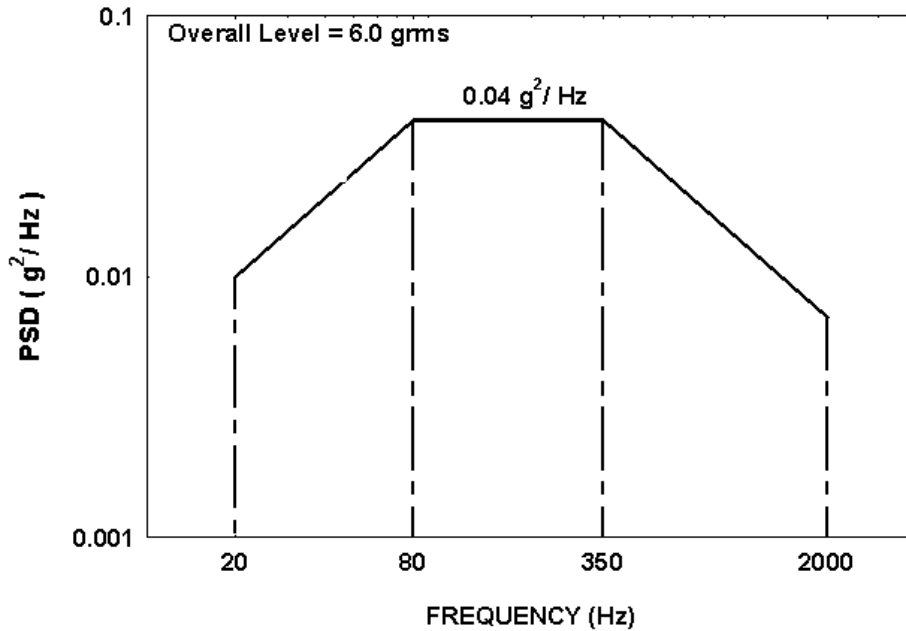


Figure 16: Sample PSD test specification profile for Naval shaker table capabilities [48].

It is important to note that the frequency on the y-axis and the frequency on the x-axis are not the same. The frequency on the y-axis (1/Hz) is a narrow frequency band that the PSD has been calculated for with a mean shift to zero such that the RMS and standard deviation are equivalent [15].

2.3.3.1. Military Standards

Most of the design limits and base input vibrations have been determined over time through physical testing or knowledge grandfathered in by previous developments. The naval, space and military standards hold much of this information with specifications for vehicle dynamics, electronic device vibration limits, and payload vibration limits.

MIL-STD-810 specifically outlines the input and response limits for a 2 wheeled vehicle, and outlines the military standard for cut off frequencies in land vehicle vibration to be 5Hz for the time history transformation [40]. Additionally the peak velocity of 50 in/sec is considered as the shock severity threshold for military components [41]. Section 7 of MIL-STD-1540C outlines the general acceptance test for temperature, humidity and vibration cycles for a space vehicle [49]. The

minimum acceptable random vibration PSD input for a component less than 23kg is shown in Figure 17.

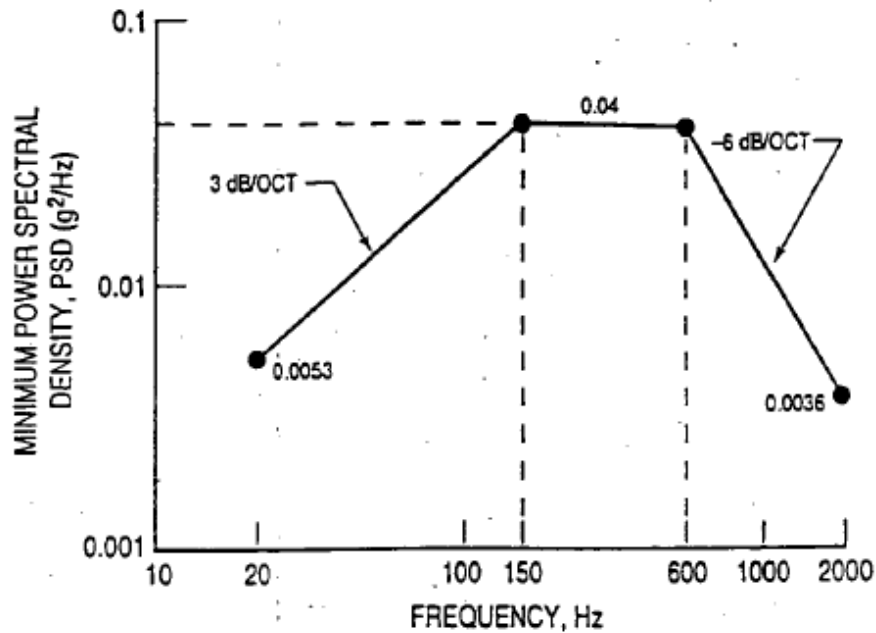


Figure 17: MIL-STD-1540C Section 7 Minimum Random Vibration Spectrum – Unit Test [49].

In 1957 the Advisory Group on Reliability of Electronic Equipment (AGREE), created in 1952 by the Department of Defense Research and Development Board to "monitor and stimulate interest in reliability and recommend measurements", published results on establishing environmental test profiles to be used during reliability demonstration testing [48], such as seen in Figure 16 and Figure 14. Figure 18 depicts the same base input specification from NAVMAT P-9492 but in acceleration, velocity and displacement PSD formats to clearly show the equivalent inputs through different formats.

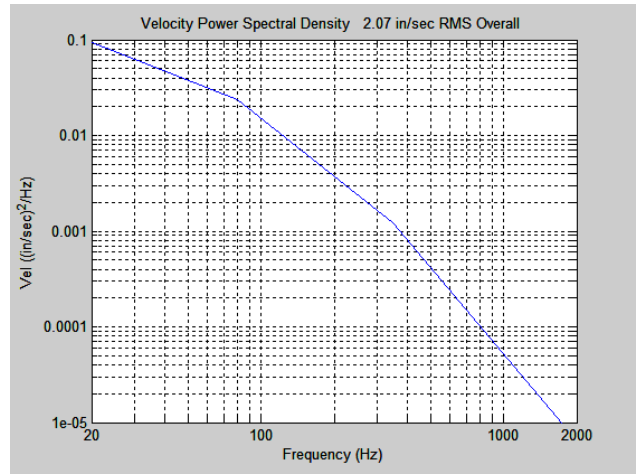
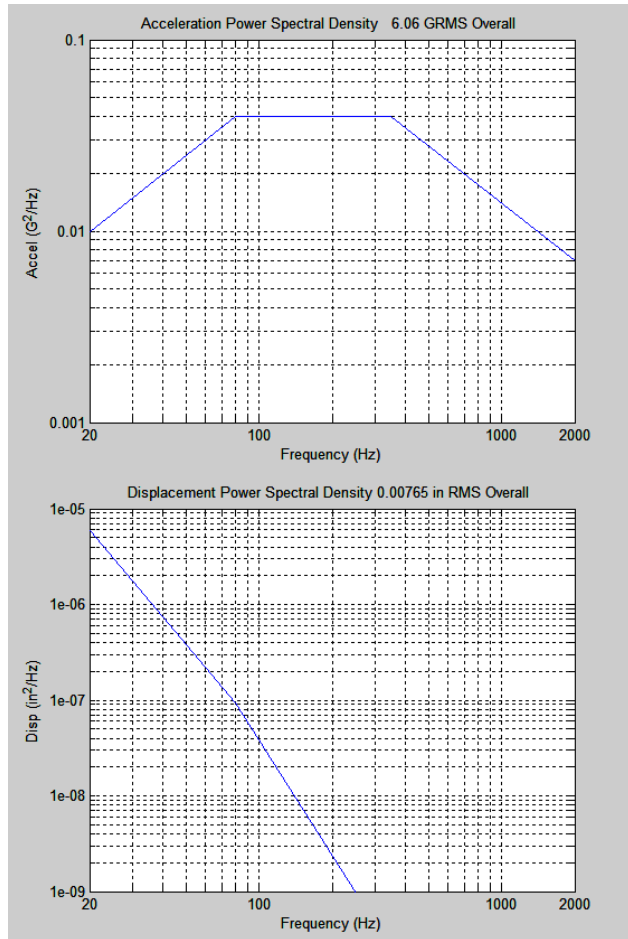


Figure 18: Equivalent acceleration, velocity and displacement NAVMAT input PSD for electronic component testing [48, 50].

2.4. Ground Vehicle Vibration Analysis and Simulation

The majority of ground vehicle dynamics are on long haul trucking, farming equipment and trains focusing on whole body vibration. The study of whole body vibration is a focal point in these industries as this is the vibration affecting the human passenger. However, the same principles can be applied to the rover's vibrations, replacing the passenger with the rover's onboard systems. In the passenger industry ISO 2631 is applied to set vibration exposure limits [51] in the same fashion that Figure 1 is implemented by the CSA for rover vibration limits. Through Hall's work on train and ground vibration simulation it was found that 3D simulations were the most effective way to use an FE model to simulate a response vibration [52]. Although 2D models could be used to represent certain phenomena of train induced vibration on the track and ground, only with 3D modelling could the correct magnitudes and trends be obtained [52]. In both the study of trains and farming equipment the standards were set using the same approach as the CSA by using test tracks to determine the input over a known ground [51]. This leads way to the objective of this research to determine standard PSD inputs for a given ground topology to reduce physical testing required.

It was found by Park that point contact models can produce good predictions of light vehicles on paths where the soil is not deformable [53]. This allows single point inputs to be used in the FE model representing the rover as the bedrock terrain is compacted aggregate [54]. It was additionally found that the tire deformation is less significant with rigid ground [54]. This in turn removes the obligation to include the steel wheels within the rover's vibration analysis.

2.5. Areas for Further Research (Vibration Response Spectrum)

The focus of this research is to determine an input PSD as a function of the ground topology and an FE simulation to match the response PSD of the rover with experimental results provided by the CSA. To determine the effect of the onboard instruments and payloads, it is important to understand the inherent limitations and next steps. When designing a system and reviewing the response PSD to a base input such as MIL-STD-1540C (Figure 17) the overall RMS of the response is considered, to see the total energy the system or component will need to withstand given some band of natural frequencies as shown in Figure 19.

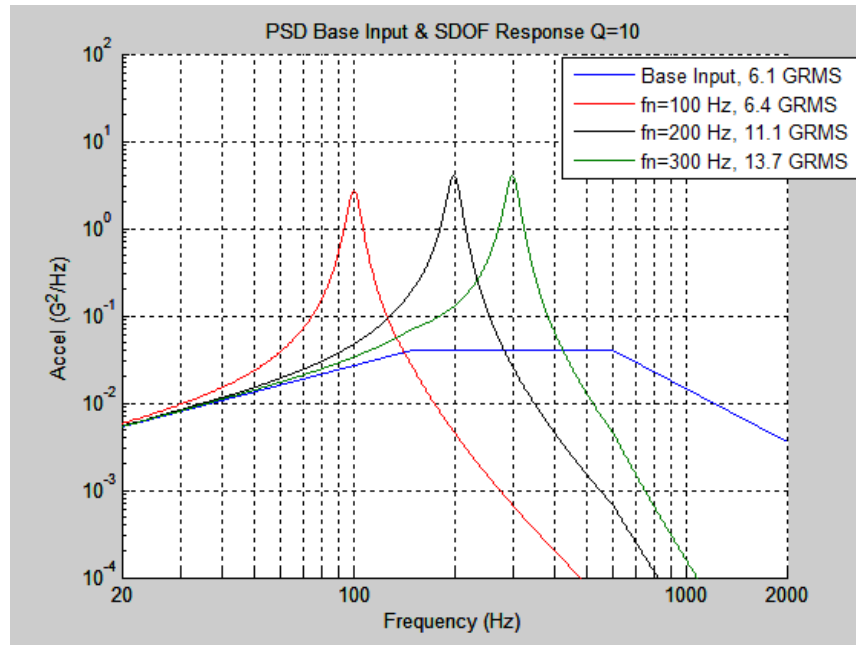


Figure 19: Example of response PSDs based on varying natural frequencies to a base input per MIL-STD-1540C [55].

Converting Figure 19 into a vibration response spectrum (VRS), Figure 20, it can be seen that at less than 600Hz lower acceleration levels are seen, so soft mounting is better as this will lower the natural frequency and reduce the overall GRMS, but relative displacement increases so clearance and sway space become important [55].

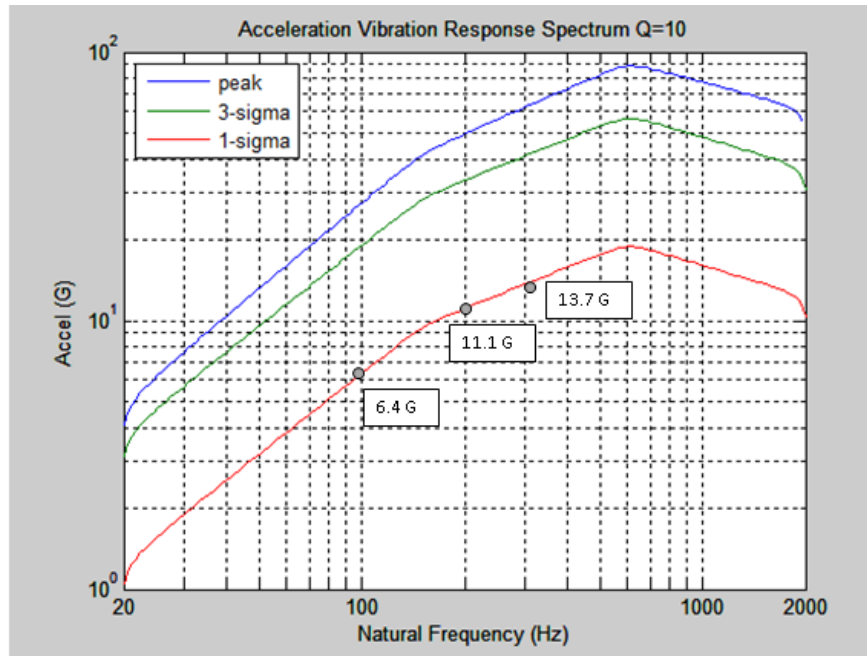


Figure 20: VRS example from MIL-STD-1540C base input, validating that peak responses are not exceeded based on response PSD [55].

Using the VRS the response energy of a component on board the rover can be evaluated given the different mounting stiffness's used on the component plus the different mounting natural frequencies. This is useful to ensure the overall energy on a component does not exceed the component's limit, the fatigue characteristics are not exceeded, and the likelihood of vibration affecting functional performance is avoided through proper damping over the driving range and fundamental frequencies of the rover.

In the 1990's flight data was measured on a prototype test aircraft with an accelerometer mounted near a component in flight. The aircraft was flown through harsh maneuvers to test the aircrafts transponder response to the input vibrations. The PSD for the collected data overlaid onto the specification limit is shown in Figure 21. The specification PSD for the flight has an overall level of 7.8 GRMS, which is higher than the measured flight level of 2.9 GRMS. However, the specification limit does not contain all the spectral peaks measured. Most notable are the peaks at ~870Hz and ~330 Hz. These peaks could even be more extreme depending on flight configuration and flying pattern [56].

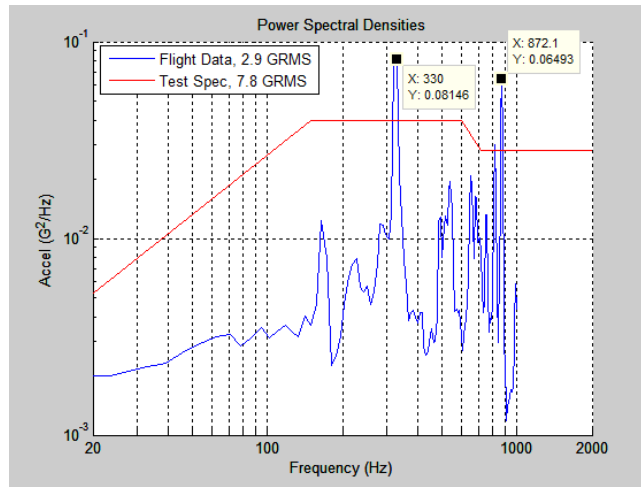


Figure 21: Flight data PSD and specification limit showing two spectral peaks above the PSD test limits [55].

Using the VRS it can be seen that the test specification is sufficient as the test specification creates a higher response than the flight data across all natural frequencies, with margin to spare as seen in Figure 22. This again leads to the VRS being the next step in analyzing the rover to determine component damping and suspension systems to ensure the weight of the rover and cost spent on damping and vibration control can be minimized and is not purely based on the overall RMS of the response PSD to a base input.

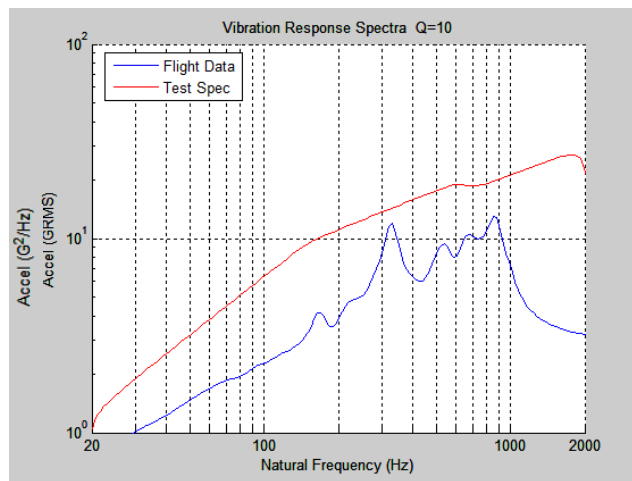


Figure 22: Flight data VRS and specification limit showing that the vibration in flight does not exceed the test limit specifications [34].

3. Methodology

3.1. Introduction

Juno is one of the CSA’s lunar test rovers. The Juno rover has a U-shaped design, built by Neptec and is intended to carry science instruments and payloads [57].

Juno weighs 300kg with a maximum payload capability of 275kg and is approximately 1.38m wide by 1.6m in length. A brief summary of the rover specifications can be found in Table 8 and one of the rovers configurations can be seen in Figure 23.

Table 8: Juno rover overview [57].

Item	Value
Approximate Dimension	1.38 m x 1.6 m x 0.75 m
Mass	300kg
Maximum Payload	275kg
Maximum Speed	12km/h
Power Source	Lithium-Ion batteries
Suspension Style	Rocker-bogie



Figure 23: Juno Rover with rubber tires.

One of the key features Juno offers is the ability to easily swap out many types of wheels on the same drive platform. With the ability to have rubber tires, metal tires, Iring wheels, or even a belt driven system, Juno can be used in a variety of terrains.

At the CSA’s outdoor MET, Juno was driven in two different states; with and without a payload. This study focuses on the rover’s vibration while the payload, represented by a dumbbell, was mounted to the front plate as seen in Figure 24.

Within the outdoor terrain there is a section of rock beds highlighted in Figure 25. This study focused on rock bed D (BR5), which is one of the four sections as described in Table 9.

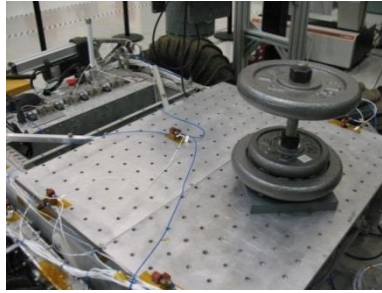



Figure 24: Payload configuration [58].





Figure 25: CSA MET, with Rock Bed area highlight in red box [54].


The rock bed area is split into four sections with each section having different aggregate sizes, as shown in Table 9. Each section of rock bed is 6.0 meters wide by 15.0 meters long. The rock beds are 0.3 meters deep, with the top layer of rocks at a uniform size; clean crushed stones with diameters of 20 mm fill the remainder of the depth. Each rock bed is enclosed by a wooden border that keeps them separated from each other and the surrounding sand.

Table 9: Rock Bed details [57].

Rock Bed	Surface Rock Avg. Diameter (mm)	Surface Rock Depth (mm)	Picture
A (BR2)	20	300	

Rock Bed	Surface Rock Avg. Diameter (mm)	Surface Rock Depth (mm)	Picture
B (BR3)	50	50	

Rock Bed	Surface Rock Avg. Diameter (mm)	Surface Rock Depth (mm)	Picture
C (BR4)	100	100	

Rock Bed	Surface Rock Avg. Diameter (mm)	Surface Rock Depth (mm)	Picture
D (BR5)	200	200	

Juno was instrumented with 23 accelerometers in various locations, outlined in Figure 26. Each accelerometer location is noted by the orange bubble with the accelerometer number and corresponding detection direction indicated by x, y, or z. For the purpose of this research the focus was only on z-axis vibration, reducing the number of accelerometers to 11. This includes accelerometers 1Z, 3Z, 5Z and 7Z which are located on the motors that are hard mounted to the wheel hubs. For these locations the CSA provided the raw response acceleration with no payload present and the generated response PSD with the payload present. The remaining 7 accelerometers of interest are 11Z and 12Z at the rover's corners, 9Z and 10Z at the drive arm connection points, 15Z at the structures center of gravity, 28Z where the DAQ was mounted and 29Z where the payload was mounted. The generated response PSD for each of these locations, except 28Z, was provided by the CSA. Due to accelerometer malfunctioning the field data collected at 28Z was inaccurate. All of the PSD data is from field testing as the rover drove over BR5, 200mm aggregate with the payload attached at the dummy mass location.

The provided response PSDs were used for verification of the finite element models as well as for evaluation of the input PSD that was developed in this study. Verification of the FE models was performed by using the response PSDs from the wheels as the vibrational input loading and comparing the predictions with the provided response PSDs at other locations on the rover. The raw accelerometer data at the wheel hubs was then used to generate a displacement input PSD. The omega and integration methods were used to obtain a displacement time history and then an input PSD was generated by filtering of the low frequency noise below 5.12Hz. This is further discussed in Section 3.3. High frequency noise from the accelerometers was not filtered out so that geometry impacts of the FE model could be realized. However, to focus on the body motion of the rover a band filter could be applied with a lower cut off of 5.12Hz and an upper cut off of 80Hz for the Baseline FE model.

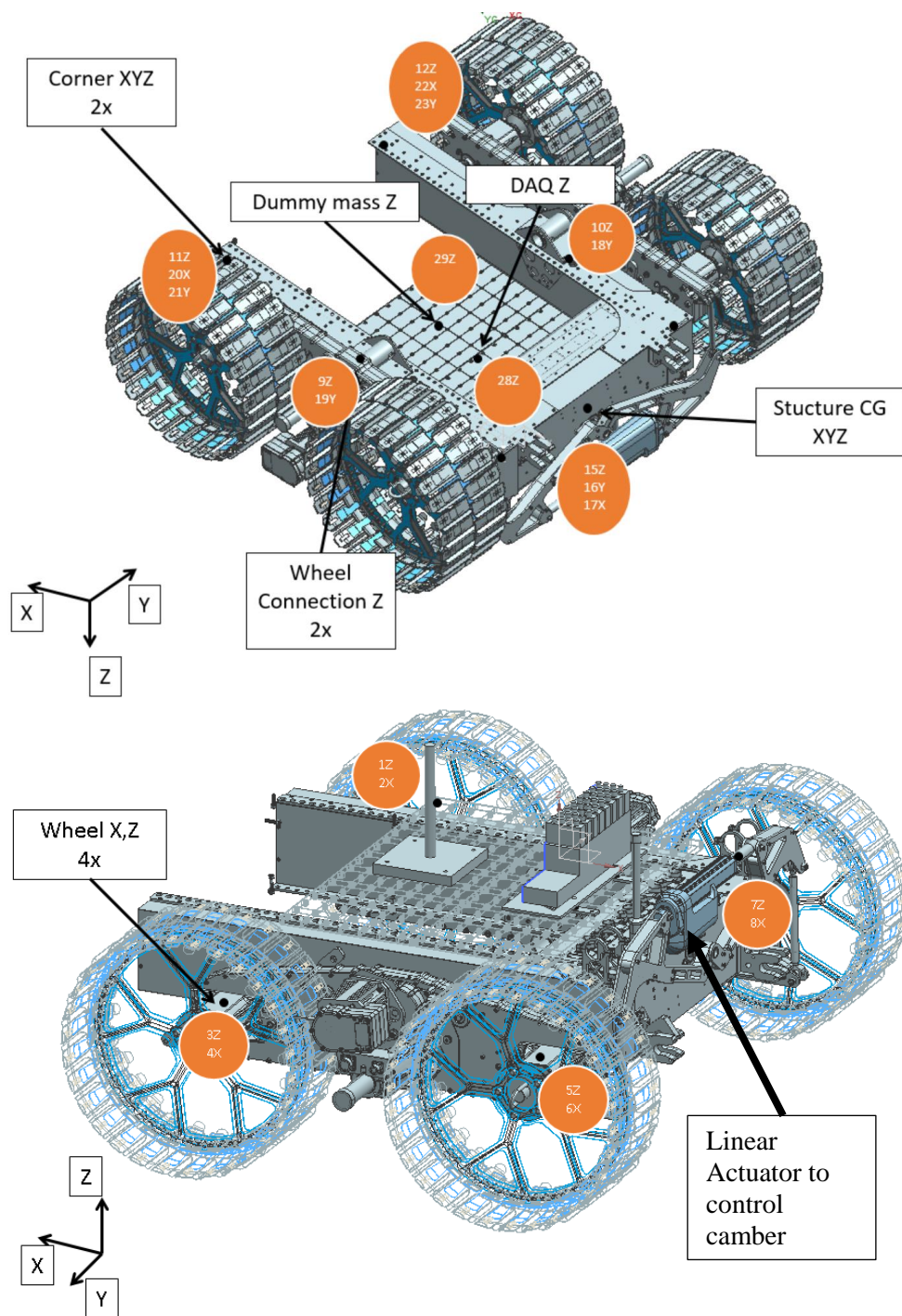


Figure 26: Accelerometer placement on Juno, adapted from CSA [5].

Figure 27 is a graphical representation of the response PSD data provided by the CSA in the form of 25,000 points for each of the 23 accelerometers over a 2560Hz range. The data provided was exclusively for BR5 (D), and was measured experimentally by driving the rover over this section of rock bed. In Figure 27 the z-axis response at accelerometer 11z, located at the corner of the chassis, is given with the 37kg payload mounted to the chassis. The CSA used a sampling rate of 5120Hz and a frequency resolution of 0.1Hz. The sample rate is aligned with Shannon's sampling theorem in Equation (16), with $W=2$, as the maximum frequency analyzed was 2560Hz over a period of 360 seconds. These sampling and analysis rates also ensure that the effects of aliasing, as described in Section 2.2.3, Analyzing Time History Data are mitigated.

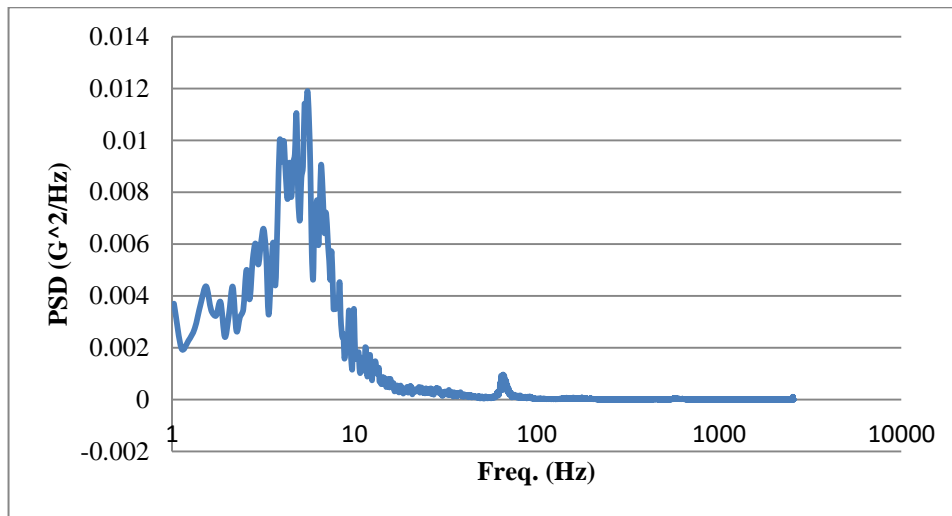


Figure 27: CSA field data response PSD at location 11 in the Z direction, as Juno drove on BR5 with payload mounted.

Figure 28 is a graphical representation of the raw accelerometer data from the wheel hub attachment point at 5Z. This data was collected without the payload present and was exclusively for BR5 (D).

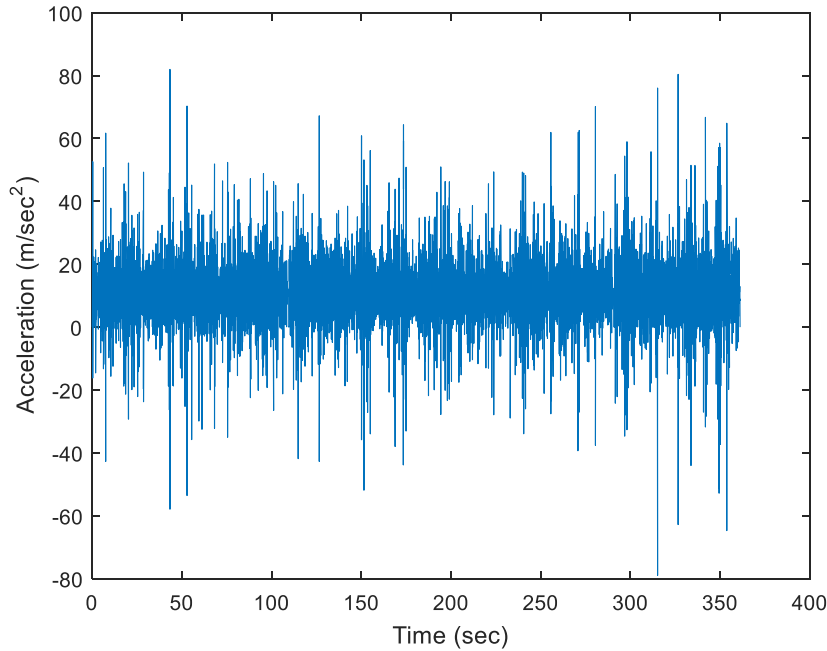


Figure 28: Raw accelerometer data from CSA accelerometer 5Z.

3.2. Model details

An FE model was built in order to determine the validity of the ground input PSD created in this research to represent 200mm aggregate terrain, through comparison with the field test response PSD. The FE model is also required to fulfil the longer term goal of this research, which is to have the ability to evaluate a rover's response to various terrain types without physical prototypes and to design a rover's drive system to match the planets terrain it will encounter. The FE model of the CSA's Juno Rover was built through verification using the provided PSD response probes at different locations on the rover's chassis. Comparisons against the field data are required to determine which features to include in the FE model in order to create an accurate simulation of the rover. ANSYS Mechanical version 15.0 was used throughout this study.

3.2.1. Rover Geometry

Two versions of the rover geometry were created. An Initial model of the rover with a simplified chassis and a Baseline model with the chassis and the drive arms included. The Initial model was used to verify the required geometrical detail and material selection for the random vibration analysis while the Baseline model was

used to evaluate the geometry interface of the connection axle with drive arms, the effectiveness of the input PSD and required damping of the FE model.

3.2.1.1. Initial Rover Geometry

The Initial model of the rover included a simplified representation of the chassis without the drive arms and without any internal supporting walls in the U-shaped body as shown in Figure 29. A dimensioned drawing of the components can be found in Figure A1 in Appendix A. The payload was modelled by a 37kg point mass but the moment of inertia and geometry of the payload were ignored. The point mass was a direct attachment to the vertex point defining the middle of the front mounting plate of the rover. The coordinate point of the mass is 7961.51mm, 0mm, 216mm (X, Y, Z), where the origin is on the chassis' front bottom edge on the line of symmetry seen in Figure 30. Details such as the data acquisition system and antennas were ignored as they have minimal to no impact on the overall rover stiffness or the accelerometer readings as they are relatively light. Each attachment and fastening point was considered to be an ideal, fully bonded joint represented by using common nodes between surfaces. In Figure 29 it can be seen that bodies of the rover were divided to enable controlled meshing of the geometry.

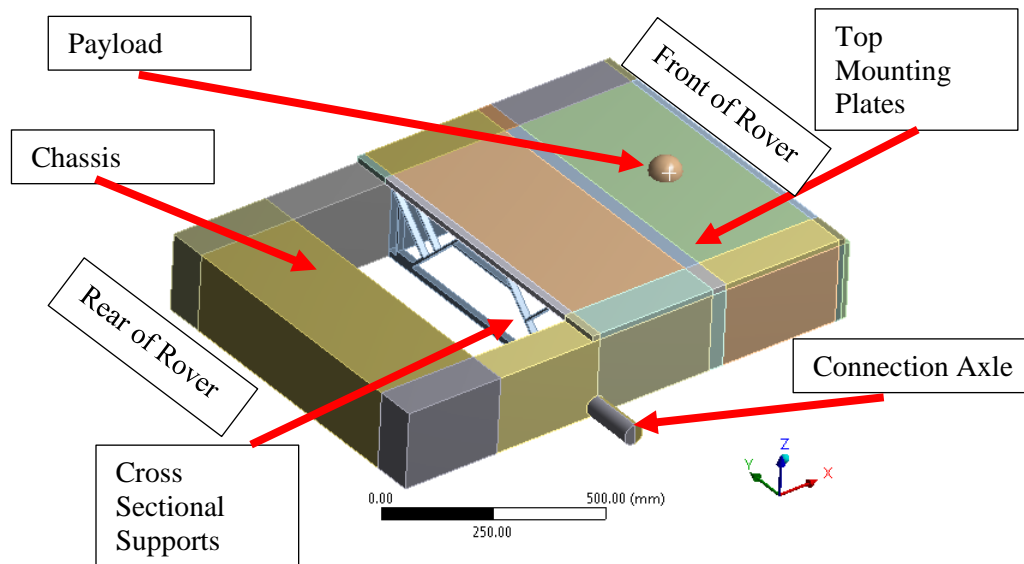


Figure 29: Initial rover geometry ANSYS divisions for meshing.

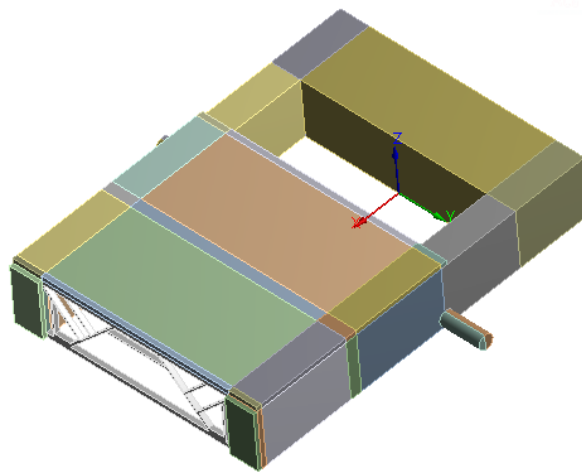


Figure 30: Location of FE model origin.

Figure A1, of Appendix A, shows the dimensions of the simplified U shape chassis with the top mounting plates and cross sectional supports, as well as the axle mating to the drive arms. When first evaluating the model, the cross section supports outlined in detail A, Figure 31, were not included. With the cross sectional supports removed, the absolute motion of the rover at frequencies under 10Hz and above 20Hz was reasonable compared to the field data. However, simulation data between these frequencies was four orders of magnitude higher than the field data. This was due to excessive flexibility in the U-shaped chassis. Once cross sectional supports were included, the predicted response PSD was more representative of the field response PSD.

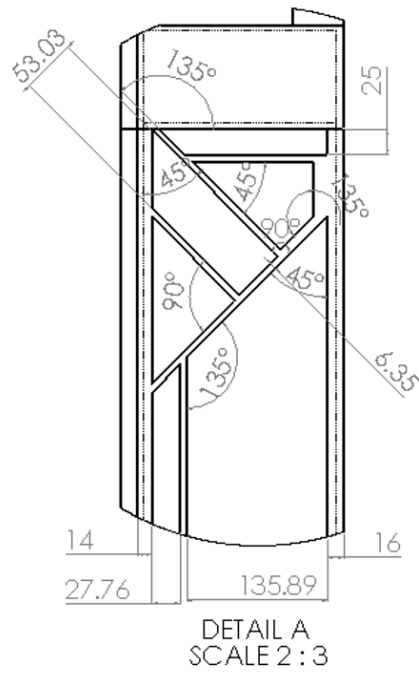


Figure 31: Detail A - Chassis Cross Sectional Supports

3.2.1.2. Baseline Rover Geometry

The Baseline model includes the drive arms, shown in Figure 32, and applies the input PSD through the motor arms directly to determine the required damping and effectiveness of the generated PSDs.

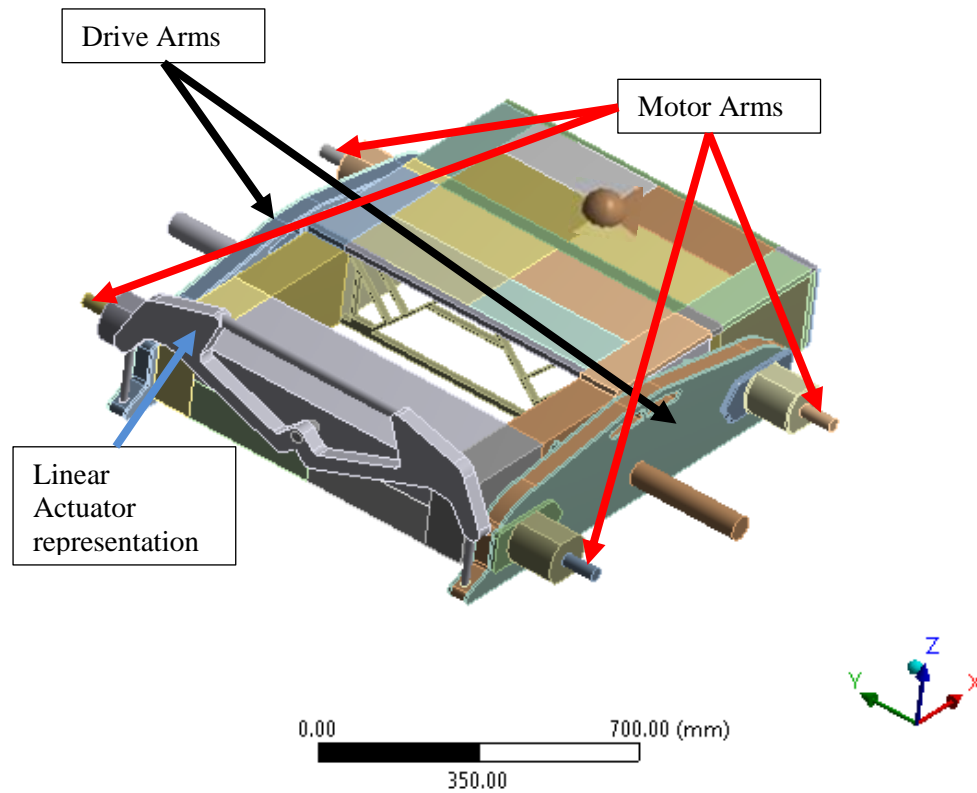


Figure 32: Baseline rover geometry showing divisions for meshing.

Figure A2, of Appendix A, gives the detailed drawing for the Baseline model with only the dimensions that were changed from the Initial model shown. It was determined that the swash plates, shown in Figure 33 and the general geometry of the linear actuator, Figure 26, were necessary in order to obtain the same trend as the field response PSD. When the drive arms were initially included without the linear actuator and swash plates, the response PSD was four orders of magnitude greater than the expected response in the 15-50Hz range as the model's stiffness was too low and allowed excessive deformation. During field testing, the connection axle and the linear actuator were all in a locked position constraining the drive arms so that the chassis, drive arms all moved without large relative displacement. The rover was effectively in a “rigid state”, with no relative motion of the drive arms. This required the FE model to use these features to obtain the correct structure stiffness. The swash plates shown in Figure 34 are used to minimize the motion of the drive arms relative to the U-chassis, and act as a bonded surface between the chassis and the drive arms. These swash plates restrict

the relative motion of the front and rear of the chassis with the drive arms, shown as detail G of Figure A2, Appendix A, also provided in Figure 33 and highlighted in Figure 34.

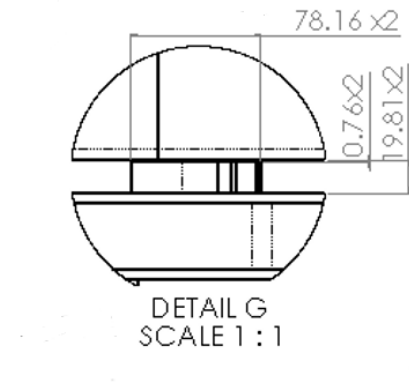


Figure 33: Detail G - Swash Plate Geometry

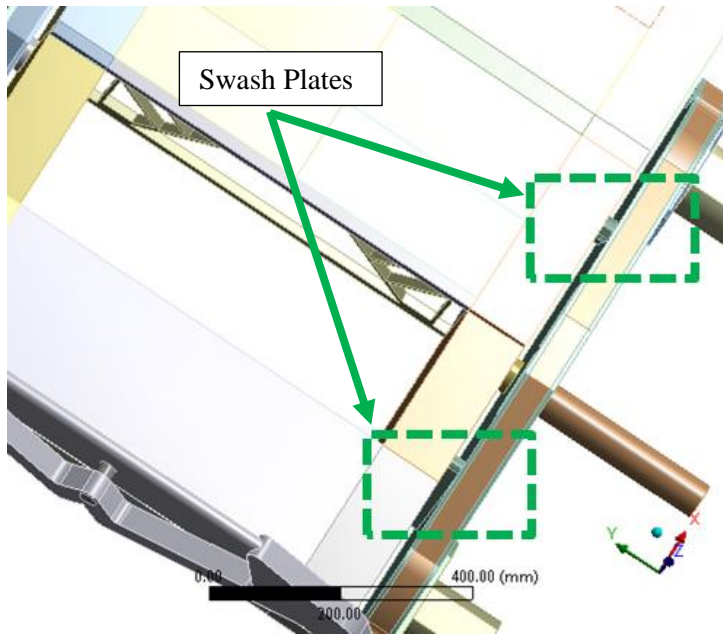


Figure 34: Baseline rover geometry - Swash Plate are highlighted by the green boxes.

With the more realistic representation of the drive arm to chassis connection, the simulated response PSD aligned with the field data for frequencies up to approximately 40Hz and over 60Hz. Within the 40 – 60Hz range, two modes still produced results two orders of magnitude greater than the field data. This was due to the motion of the drive arms as a result of rotation about the y-axis. The linear actuator seen on the right hand side of Figure 26 at the rear of the rover was in the locked position during the entire field testing, and used to apply a neutral camber to the wheels. A rough approximation for this subassembly was added to the rover as seen on the left hand side of Figure 32, which was sufficient to align all response PSD data in the model with the field data.

3.2.2. Material Properties

The true material information for many sections of the rover could not be shared by the CSA, but the mounting plates which had the largest mass were made of 6061 aluminium alloy. It was therefore assumed that the entire rover structure was made of 6061 and represented by an isotropic material model with the properties outlined in Table 10. The FE model assumes a flexible body, rigid material and rigid body assumption were not used in the analysis. Based on the response PSDs generated, this was a reasonable assumption.

Table 10: Material properties.

Property	Value	Units
Density	2770	kg/m ³
Young's Modulus	7.10E+10	Pa
Poisson Ratio	0.33	
Bulk Modulus	6.96E+10	Pa
Shear Modulus	2.67E+10	Pa

3.2.3. Mesh

The rover was separated into several geometric subsections to improve mesh control and to utilize a sweep mesh of hexahedral elements in as many locations as possible. It was ensured that all parts of the geometry had three elements through the thickness and that triangular elements maintained a 20-120 degree angle and

quadrilateral faces maintained a 35-145 degree angle. The Baseline model with the rover's final mesh can be seen in Figure 35. The total number of elements in the mesh is 21,624 with 97,287 nodes. A study on the impact of the mesh density is discussed in Section 3.2.3.1, Element Type and Mesh Density Study.

Mesh

18/03/2019 9:17 PM

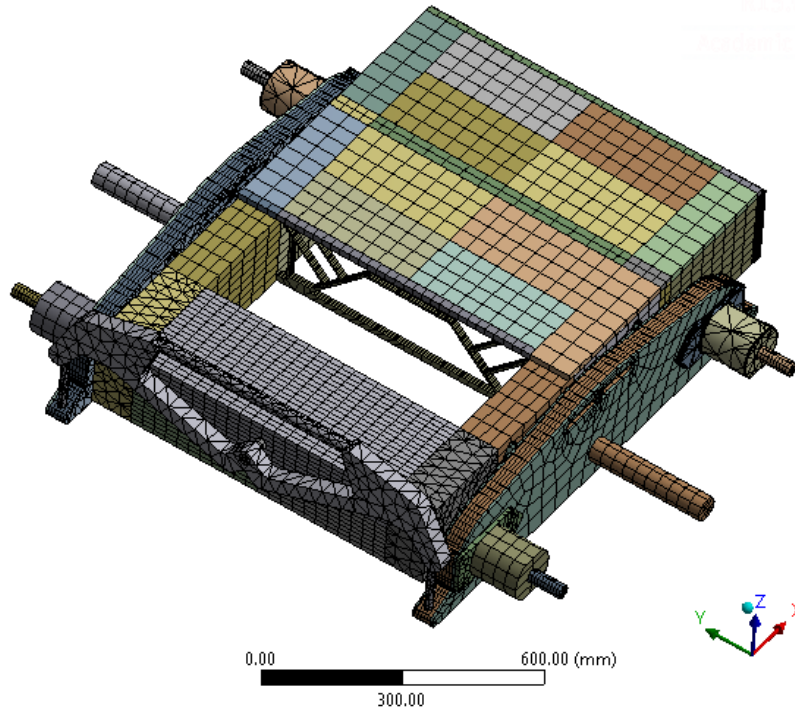


Figure 35: Fully meshed Baseline rover.

Since this research is focused only on the vibration response and not the stress induced by the vibration, the element density does not have as significant of an effect on the results. The elements only need to represent stiffness, proper mass and predict displacements so the critical role is purely to represent the geometry of the structure.

3.2.3.1. Element Type and Mesh Density Study

This study was performed to determine the impact of mesh density on the response PSD of the rover. First, lower and higher order elements were compared. Figure 36 shows the response PSD predicted by the Baseline FE model for both high and low order elements compared with the field test response PSD for the rover. The generated response PSDs are all plotted directly as outputs from the FE model probes as 1σ results. When lower order elements were used, the low frequency

response matches with the general trend of the field data, however the peak around 70Hz is completely missed. When higher order elements were used, the response PSD shows that entire range of frequencies is captured.

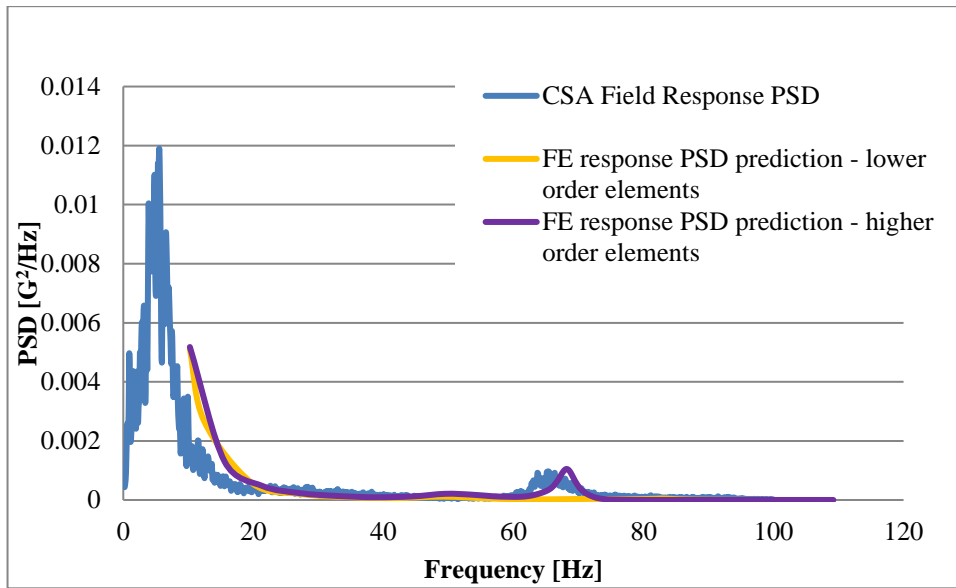


Figure 36: Comparison of higher and lower order element response PSD with 2.5% damping against field data response PSD at location 11Z.

The response PSD from Figure 36 shows that the spectral peaks are captured and that the GRMS is approximately equivalent above the 10Hz cut off when using higher order elements. To understand why the response PSD from a model meshed with lower order elements did not align with the experimental PSD results, the modal results were reviewed. Table 11 shows that the natural frequencies of the first 10 modes are higher for the lower order mesh. This implies that the structure is stiffer than when meshed with lower order elements, this is likely due to Shear Locking. Shear Locking is due to the linear interpolation functions of the lower order elements stiffness matrixes. The linear interpolation does not model the curvature of elements so with lower order elements additional shear stress enables elements to meet equilibrium with smaller displacements [59]. The shear strains should be negligible, but the inconsistent terms in the interpolation functions of the low order model cause non-zero artificial shear strains which absorb energy making the element stiffer [60]. Note that only one rigid body motion mode (mode

1), is present because the boundary conditions in the FE model only allowed motion in the Y direction.

Table 11: Modes of lower order and higher order FE models at 2.5% damping.

Mode	Frequency (Hz)		Percent Difference $\left(\frac{ Lower\ Order - Higher\ Order }{Lower\ Order}\right)$
	Lower Order	Higher Order	
1	1.82E-03	1.14E-03	
2	82.55	66.91	23%
3	102.40	68.94	49%
4	164.22	92.60	77%
5	201.95	125.35	61%
6	215.20	144.44	49%
7	232.29	150.19	55%
8	233.22	199.10	17%
9	236.10	200.64	18%
10	239.10	216.70	10%

The effect of mesh density is shown in Table 12 through a comparison of the total CPU time from preprocessing to solution generation and GRMS between a coarse, nominal and dense mesh with 79252, 97287 and 194165 nodes respectively. The mesh density does not have a significant impact on the systems response GRMS. The difference between the GRMS predicted using the coarse and the dense mesh is only 3.9%, the sum of the percentage difference column under Random Response Output PSD of Table 12. The CPU time to extract the first ten modes takes a 20.5% increase in the CPU time required from the coarse to nominal model, but is a 89.9% increase in time from nominal to dense. This indicates that the number of nodes has a significant impact on the modal analysis computing. However, the number of nodes has a much smaller impact on the random vibration analysis. The dense mesh took 48.0% of the computing time as the nominal mesh random vibration analysis.

Table 12: Mesh density comparison using higher and lower order elements with input PSD generated from CSA raw acceleration data.

Model	Modal Analysis total CPU		Random Response total CPU		Random Response Output PSD	
	Time [s]	Percentage Difference	Time [s]	Percentage Difference	GRMS [G]	Percentage Difference
Coarse (79252)	51.1		14.1		0.20884	
Nominal (97287)	64.3	20.5%	16.6	15.1%	0.20989	0.5%
Dense (194165)	638.9	89.9%	31.9	48.0%	0.21727	3.4%

The nominal and the dense mesh showed no significant differences in predictions of the modal frequencies, with the largest difference being 5.15% at the second mode, given in Table 13. It is therefore reasonable to use the nominal mesh densities as it is 89.9% times faster and the GRMS is within 4% of the dense mesh results. This is especially important as this CPU time will increase in the future if the model was to include more details such as on board instruments

Table 13: Modal result comparison for nominal and high density mesh.

Mode	Nominal	Dense	Percentage difference
1	0	0	
2	68.32	64.97	5.150%
3	69.75	68.30	2.132%
4	93.92	90.13	4.204%
5	126.11	123.93	1.759%
6	145.54	142.73	1.969%
7	150.64	148.80	1.237%
8	199.50	196.37	1.594%
9	201.09	197.33	1.905%
10	216.69	216.30	0.180%

This study confirms that the nominal mesh shown in Figure 35 minimizes the discretization error while reducing the run time by 89.9%, from the dense mesh.

3.2.4. Loading and Boundary Conditions

The model was defined so that the motor arms, attached through the wheel hubs of the rover as shown in Figure 37 were constrained in the X and Z directions but were free to move in the Y direction. This constraint is required because the input PSDs can only be applied through a constrained direction. Fixing the z-axis allowed the PSD to be applied in the Z direction and allowed simulation of the vertical movement of the rover based on the terrain. The x-axis was fixed to allow future work on input PSD's in this direction.

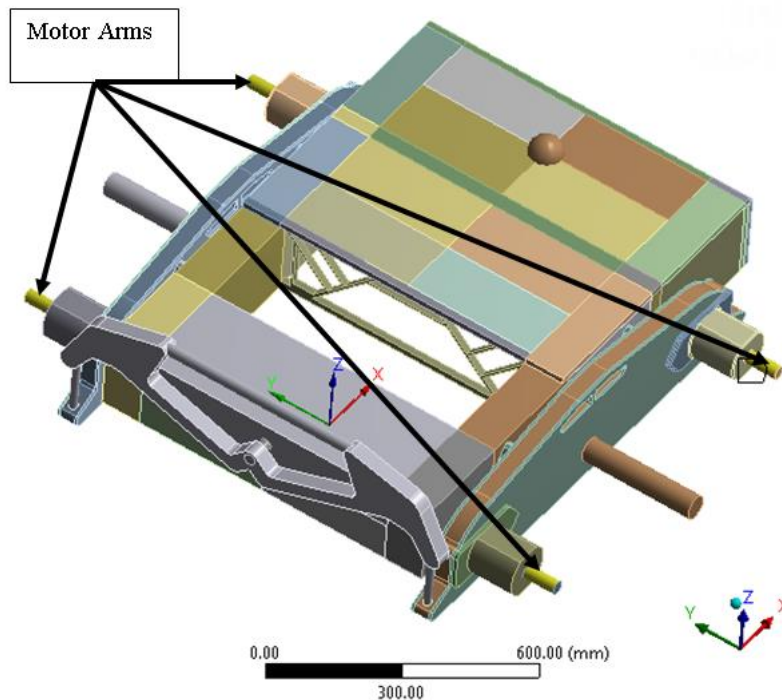


Figure 37: Boundary conditions with motor arms constrained ($U_X = 0, U_Z = 0$).

The loading was applied to the FE model in the form of PSDs. The input PSDs were applied through the motor arms and not through the wheels as they were rigid structures that provided minimal damping effects. The PSDs were input as a series of 25,000 points at given frequencies, and then a best fit was performed internally in ANSYS to create a continuous line, as seen in Figure 38. The FE model used the response PSD from the CSA as an input or used the input PSDs developed in this study to predict the response PSD through the rover structure, as described in Section 3.3. First, the FE model was verified using the PSD provided from the field data at either the axle or the motor arms. Then an input PSD was determined using the accelerations at the wheels measured in the field.

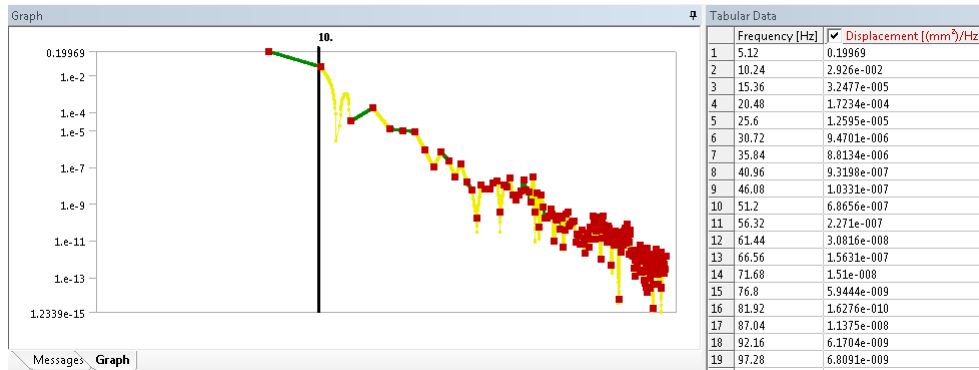


Figure 38: ANSYS best fit of displacement PSD data

3.2.5. Solution

Random vibration analysis in ANSYS is a 2 step process, first a modal analysis is performed without loading applied to obtain the natural frequencies of the assembly. Then these results are input to a random vibration analysis with an applied input PSD. In the modal analysis the first 20 modes of the structure were output and the associated natural frequencies and deformations reviewed to identify the mode shapes. The FE solution included the absolute motion which is the motion of the entire structure due to and including the input surface for the PSD, relative to the ground. Only the first mode, when frequency is 0Hz, represents rigid body motion.

The same point load was used to represent the payload and the same boundary conditions were applied to all random vibration analyses as in the modal analysis. The input PSD was applied to the motor arms in the z-axis. The acceleration output PSD was generated by ANSYS for selected nodes using probes at positions corresponding to each accelerometer location. The probes used the absolute reference and not relative motion to the location of the input PSD and output the response PSD in G^2/Hz .

3.3. PSD Generation

The only method currently used to determine the response PSD for different rover designs is to perform a field test, measure the accelerations and then convert the data to a PSD. Ultimately being able to generate an input PSD from the topology or aggregate size of a terrain will reduce the investment required for field testing and prototype manufacturing. Two methods for determining the input PSD were compared. The omega arithmetic method and the method of double integration were both used to determine the displacement PSD from the raw accelerometer data. The input displacement PSD could also be generated knowing the aggregate size to determine the surface roughness of the terrain. However, the results will be

similar since the acceleration data used does not have any system damping between the ground and the accelerometers used.

MATLAB R2015b was utilized to generate the input PSD from the accelerations measured at the rover's wheels. For this research an acceleration time history in gravitational force equivalent units (G's) from the accelerometer data at the wheel motors was provided. Each generated PSD used MATLAB's Pwelch function with a defined lower cut off frequency. The process for determining the representative input PSD was completed in three steps as follows:

1. In order to verify the process of creating a PSD from raw accelerometer data, the accelerometer data from the wheel location (5Z) was used to create an acceleration PSD. This acceleration PSD was applied to all four of the motor arms on the Baseline FE model and the predicted output PSDs at the wheel connections (9Z, 10Z), chassis (11Z, 12Z), payload (29Z) and center of mass (15Z) were compared to those provided by the CSA.
2. The omega arithmetic method was used to create the input displacement PSD from the accelerometer data from the wheel location (5Z). The effectiveness of this method was evaluated by applying the input PSD to the motor arms on the Baseline FE model and comparing the predicted output PSDs at the wheel connections (9Z, 10Z), chassis (11Z,12Z), payload (29Z) and center of mass (15Z) to those provided by the CSA.
3. The double integration method was used to create the input displacement PSD from the accelerometer data from the wheel location (5Z). The effectiveness of this method was evaluated using the same method as in step two and the input PSD was also compared to the one generated in step two.

3.3.1. Acceleration PSD Generation from Accelerometer Data

In order to verify the process of creating a PSD from raw accelerometer data, the accelerometer data from the wheel location (5Z) was used to create an input acceleration PSD. Figure 39 provides the time history data for location 5Z as the rover drove for 360 seconds over BR5, 200mm aggregate. Figure 39 shows the average acceleration due to vibration seen on the motors that are hard mounted to the wheel hubs was 10m/s^2 . A maximum acceptable ride intensity for vibration in passenger vehicles is 2m/s^2 [51, 61], but this is on relatively smooth roads and includes the vehicle suspension. As the rover has no suspension and is travelling over a 200mm aggregate, this average intensity of 10m/s^2 is reasonable. The peaks up to 8Gs (80m/s^2) are due to shock and impact vibration as the rover "lands" and

impacts with high laying aggregate. This acceleration time history is specific to this particular driving speed, suspension, vehicle stiffness and weight.

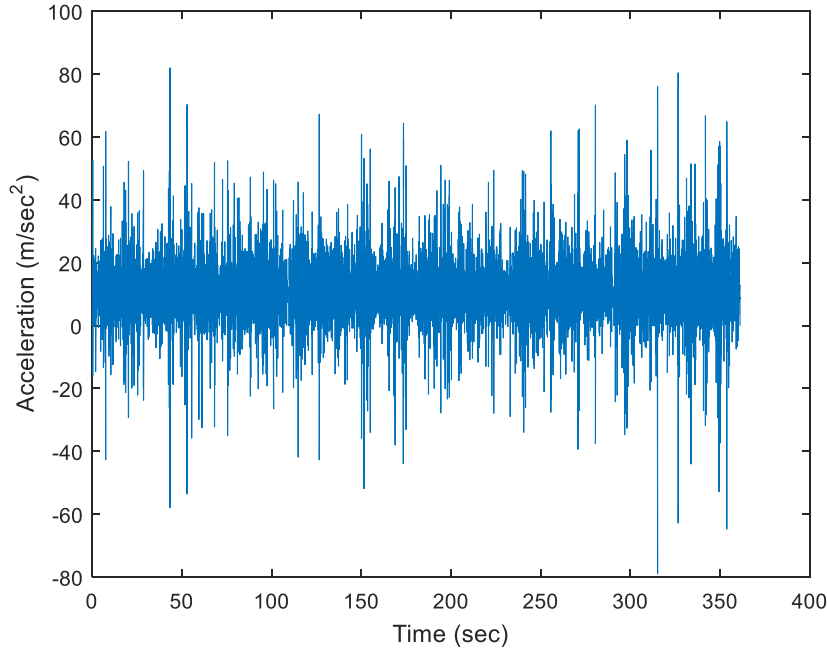


Figure 39: Raw accelerometer data from CSA accelerometer 5Z.

In order to generate the acceleration input PSD from the raw accelerometer data shown in Figure 39, Welch's approach given in Equation (13) from Section 2.2.2.2 was used with a 10.24Hz low cut off frequency to remove all noise from the acceleration vibration spectrum.

$$\hat{X}_{PSD}(f) = \frac{1}{L} \sum_{l=0}^{L-1} \frac{1}{S} \left(\sum_m x[m] (w[m]) e^{-j2\pi \frac{lm}{M}} \right) \quad (13)$$

Signal x is the acceleration data with a mean removal. The windowing function $w[m]$ is a Hanning function dividing the signal into segments of equal length (M) to give an integer value (L). The number of segments (S) is based on the overlapping specified, in this case 50% so that $S = 0.5M$. The signal length in this case is 1,849,000 and it was chosen to use $M = 1,849,000$ such that $L = 1$ and each point of the signal is 50% overlapped with the $l \pm 1$ point of the signal. Having M equal to the signal length was used in order to have a high resolution PSD generated and the 50% overlapping was chosen to contain 90% of the original signal as described in Section 2.2.3.1. The resulting acceleration PSD is shown in

Figure 40 as compared to the PSD provided by the CSA at the wheel hubs (5Z). The PSD generated from the raw acceleration data follows the overall shape of the one provided by the CSA. Differences are due to the 10% of data lost in the approximation of the PSD and the smoothing of the CSA data. The CSA field data was smoothed as 25,000 data points were collected, making the graphical representation difficult to interpret and compare. The generated PSD used 290 points and did not require smoothing to compare against the field data.

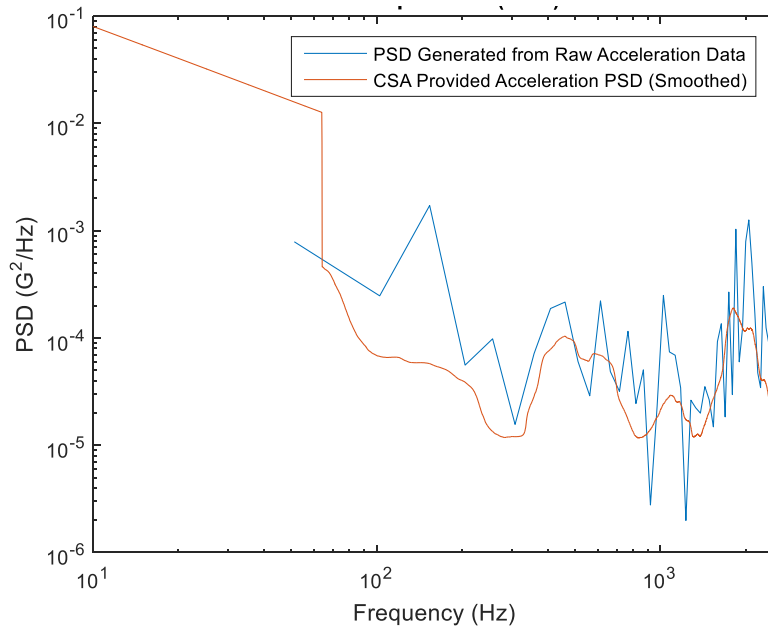


Figure 40: Generated PSD from 5Z accelerometer data without payload present against CSA provided PSD with payload present, log-log format.

The CSA provided PSD shows a much larger spike near 60Hz due to the presence of the payload, as the payload was not present during collection of the raw accelerometer data. The generated PSD has a peak near 150Hz corresponding to a natural frequency of the rover which is due to the payload mounting not being present as it was in the CSA response PSD. All higher frequencies of the field data align with the 1σ input PSD generated with the raw acceleration data, as the smoothed trend line of the CSA response PSD is the mean value of the generated PSD. Based on Figure 40, it can be concluded that the generated acceleration input PSD represents the vibration input for 200mm aggregate terrain.

3.3.2. Omega Method

The omega method was one of the two methods that were compared for generating the displacement input PSD for the 200mm terrain (BR5). The omega arithmetic method outlined in Section 2.2.3.2.2 was used to directly convert the raw acceleration time history data from Figure 39 to displacement time history as shown by the transformation outlined below. Then the displacement time history was used to determine the input displacement PSD using the Welch method.

$$[x(t) = -\omega^2 x(t)] \xrightarrow{FFT} [\ddot{X}(f)] \left(\frac{\ddot{X}(f)}{-\omega^2} \right) \xrightarrow{iFFT} [X(f)] \xrightarrow{iFFT} x(t)$$

First, an FFT was used to convert the acceleration time history into a frequency domain data set, with all values of $\ddot{X}(f)$ squared to speed up the computational process. Once this frequency domain data was determined each element of the array was divided by the negative square of the angular frequency to give displacement frequency data for the rover. The inverse FFT of the frequency data was taken to give the displacement time history of the terrain.

The transformation resulted in the displacement time history given in Figure 41. Based on the transformation, the peak magnitude of vibration displacement of the rover's 5Z accelerometer due to the 200mm aggregate was approximately 40mm. Based on the rover's top speed being 3.2km/hr and average speed being 0.15km/hr during a 360sec run there should not be extreme bouncing occurring which allows the rover to cover the terrain without large displacements. The peak displacements of the rover appear to be periodic which is likely due to the rise and fall of the rover as all four wheels peak on the terrain and then drop to a valley or nominal height. This rise and fall motion would be captured in the low frequencies of the rover's response PSD but, would not impact the generated input PSD as a 5.12Hz cut off frequency was used on all displacement PSDs.

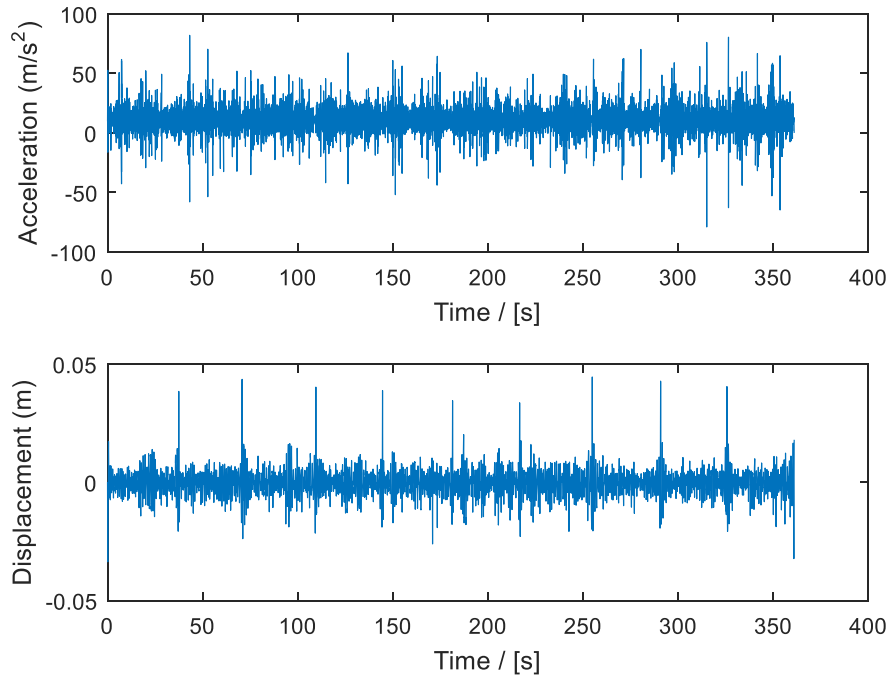


Figure 41: Raw acceleration data from 5Z and displacement data generated using Omega Method.

The Welch method described in Section 3.3.1 was applied to the displacement time history from Figure 41, to create the displacement PSD shown in Figure 42. Hanning windowing was used with 50% overlapping to retain 90% of the segmented data, and the data up to 2560 Hz, the Nyquist, was retained for the displacement PSD. The frequency cut off for the PSD generated with the displacement time history was set to 5.12Hz to align with MIL810 and to provide the most confident results as low frequency noise could risk error propagation.

The displacement energy input for 200mm aggregate can be said to be roughly evenly distributed in the positive and negative Z direction, as the amplitude of displacement is relatively symmetrical about the mean in Figure 41 indicating there is no system damping. In Figure 42 the displacement PSD is decreasing linearly with frequency on a log-log plot. This decrease is likely due to the displacement of vibration being smaller as frequency increases, giving a reduced normalized magnitude of vibration input. The fact this is a linear decay on a log-log plot means the input PSD is an exponentially decaying input.

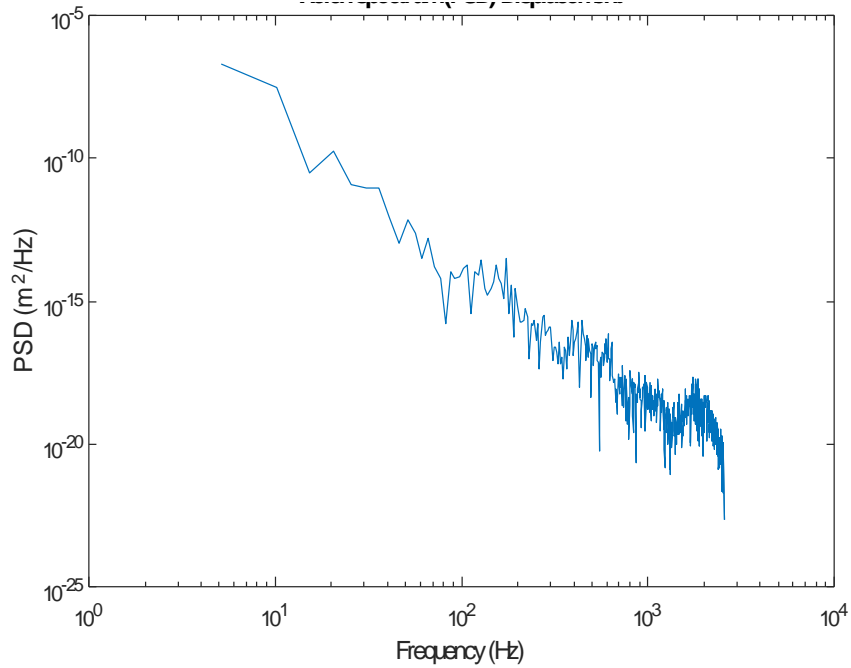


Figure 42: Displacement PSD generated using the Omega Arithmetic Method, in log-log format from CSA 5Z accelerometer.

3.3.3. Integration Method

The method of double integration was the second of the two methods that were compared for generating the displacement input PSD for the 200mm terrain (BR5). Double integration, described in Section 2.2.3.2.1, was used to directly convert the raw acceleration time history data from Figure 39 to displacement time history as shown by the transformation outlined below using cumulative trapezoidal integration. Then the displacement time history was used to determine the input displacement PSD using the Welch method.

$$x''(t) \xrightarrow{\left(\sum_{i=1}^N \frac{1}{2}(\dot{x}(i-1) + \dot{x}(i))\Delta t\right)} x'(t) \xrightarrow{\left(\sum_{i=1}^N \frac{1}{2}(\dot{x}(i-1) + \dot{x}(i))\Delta t\right)} x(t)$$

The acceleration time history was put through a Butterworth filter such that frequencies above 1Hz were able to pass through. Then using the cumulative trapezoidal method the acceleration time history was integrated to produce the velocity time history shown in Figure 43. The velocity was then de-trended with a mean removal to reduce drift error. Drift error is when the inputs of a system are constant but between device measurement error such as the accelerometer and propagation error such as rounding cause the results to drift from the actual value in the integration calculation. One particular issue with double integration from

acceleration collected from an accelerometer is an error in orientation causes an incorrect projection of the acceleration signals and acceleration due to gravity can no longer be removed from the acceleration due to vibration [62].

As discussed in Section 3.3.2 there appears to be a periodic sequence every 40 seconds which is likely due to the rise and fall of the rover as all four wheels peak on the terrain and then drop to a valley or nominal height. This rise and fall motion would be captured in the low frequencies of the rover's response PSD but, would not impact the generated input PSD as a 5.12Hz cut off frequency was used in the PSD generation. The two large peaks at 175 seconds and 360 seconds are most likely a hard impact that occurred possibly due to an imbalance on the rover as it is also periodic occurring every 175 seconds.

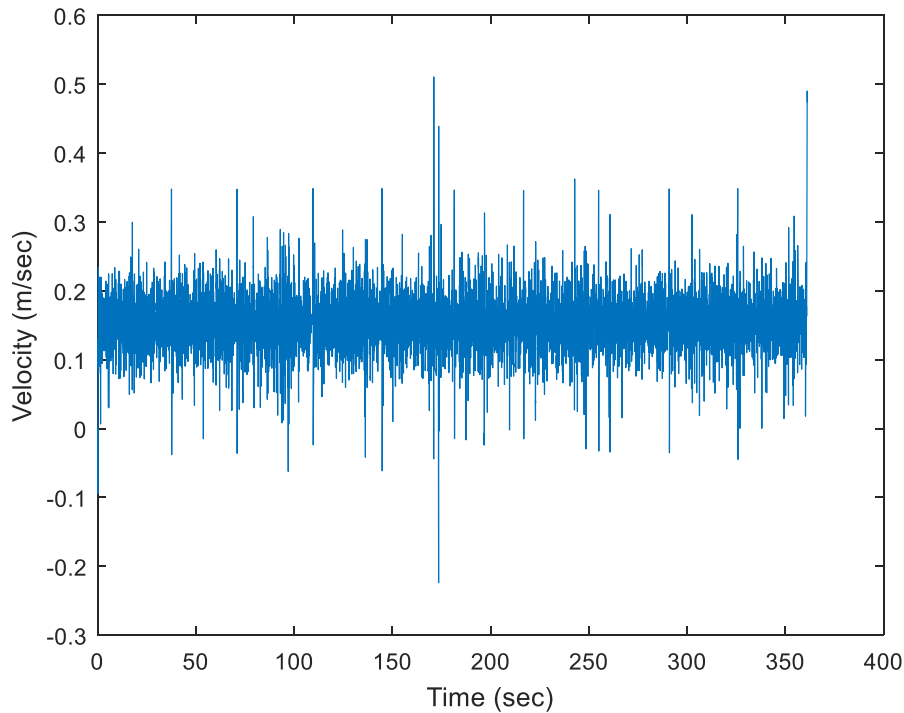


Figure 43: First integration of accelerometer 5Z data to generate velocity data.

The displacement time history determined using the integration method, was detrended, giving a displacement representing the terrain's topology in Figure 44. The time history shows the maximum displacement at accelerometer 5Z to be approximately 6mm, while the omega arithmetic analysis gave a peak displacement of 40mm. Even though there is a large discrepancy between the peak values of the

two methods, likely due to drift error in the integration method, this has minimal impact on the input displacement PSD as a cut off frequency of 5.12Hz was implemented. These large displacements are seen at frequencies less than 0.025Hz.

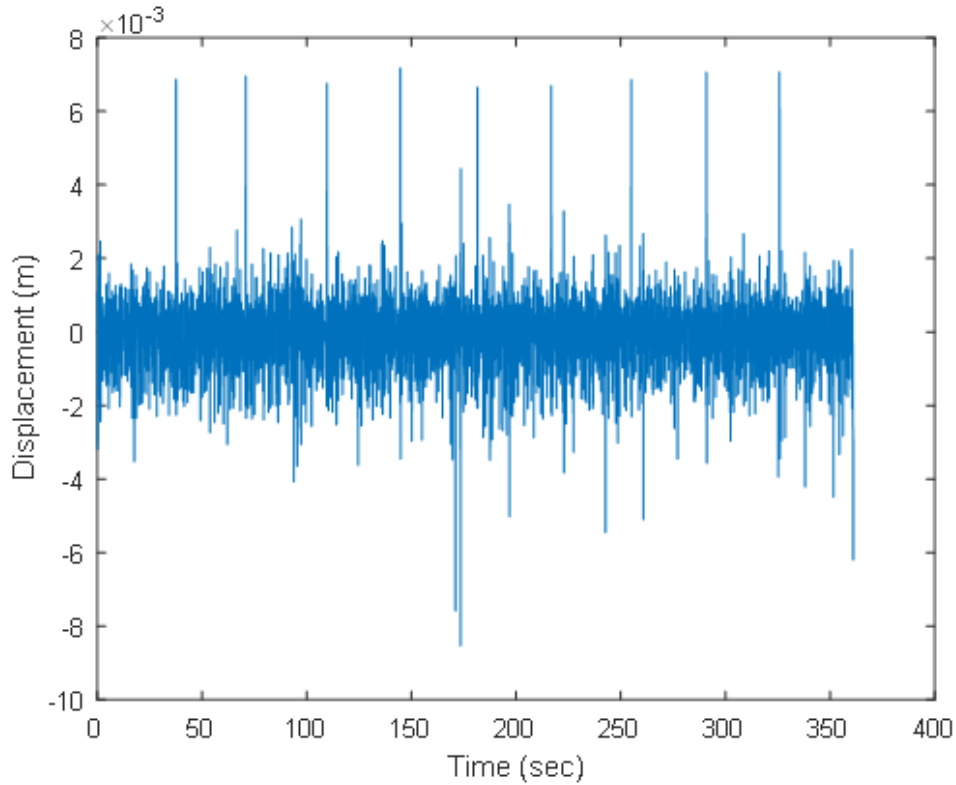


Figure 44: Double integration of accelerometer 5Z data to generate displacement data

The displacement time history seen in Figure 44 was converted to a PSD using the Welch method as discussed in Sections 3.3.1 and 3.3.2 as shown in Figure 45. A frequency cut off of 5.12Hz was used with a 50% overlap Hanning window. Using the double integration technique yields an exponential decaying input PSD similar to the omega arithmetic displacement PSD. These methods are further compared in Section 4.2.

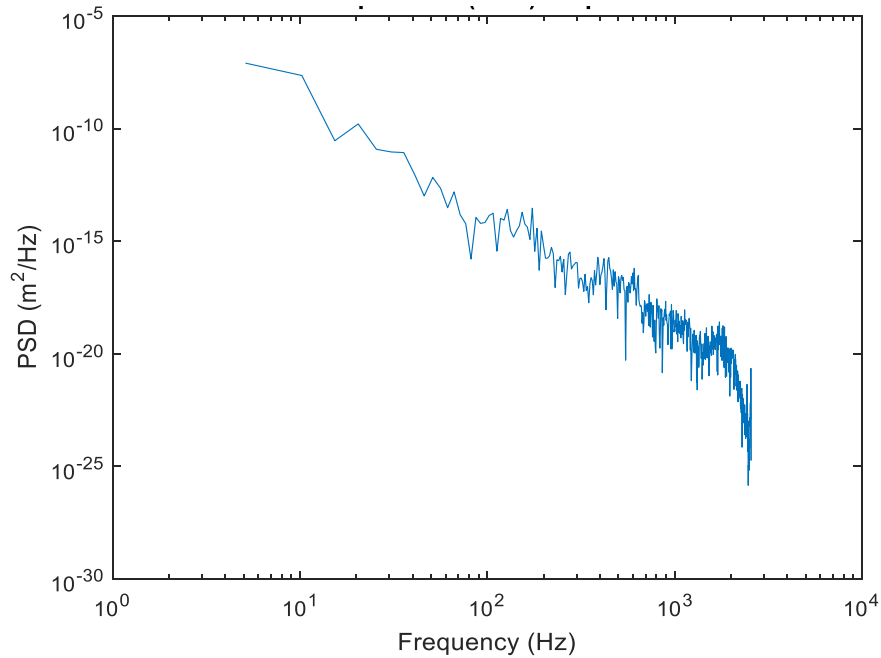


Figure 45: Displacement PSD generated with Welch Method from Double Integration using log-log format.

3.4. Damping Effects on Vibration Response

Damping has a direct effect on the response PSD of a system, the higher the damping the lower the response magnitude. In order to determine what damping coefficient should be used in the finite element simulations, the effect of system damping on the response PSD of the rover at 11Z (chassis) was analyzed using the Baseline FE model. The acceleration, and two displacement PSDs generated at the motor arms were input. Figure 46 shows a plot of the 1σ predicted response PSD of the system damped at 1% for the three methods as compared to the field data. At the low frequencies $<50\text{Hz}$, the damped response is statistically probable but above this frequency limit the system is clearly under damped at the 1σ response. The predicted PSDs are orders of magnitude larger than the true system response, and as this is with mean removal, the 3σ response would be three times larger yet.

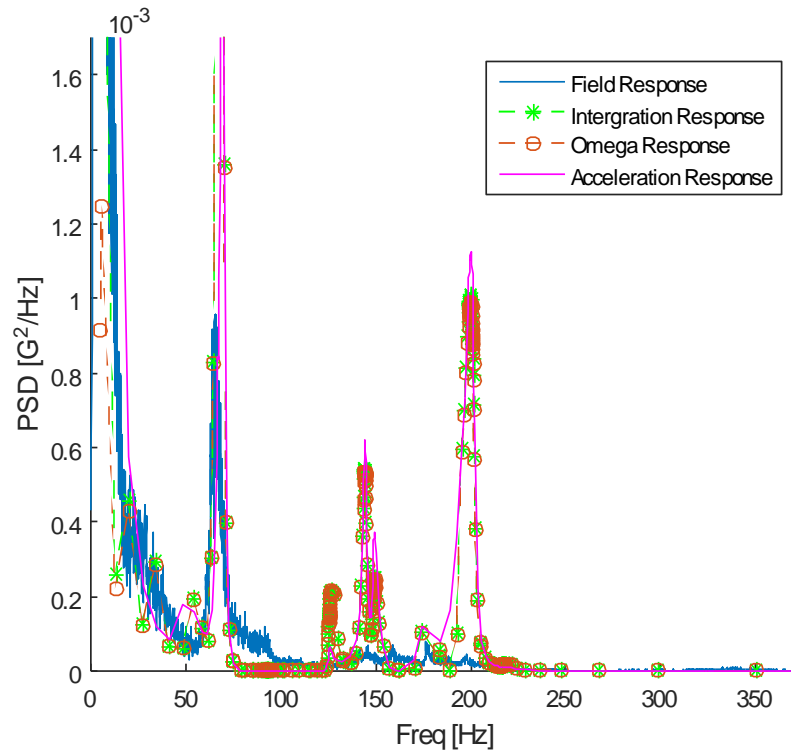


Figure 46: Output PSD for sensor 11Z field versus simulated response PSD at 1% damping.

ANSYS standard damping is 1% and in static structures such as sky scrapers the rule of thumb is 5% [7, 13]. At 1% the finite element predictions were underdamped at all frequencies less than 250Hz as seen in Figure 46. At 5% damping the response PSDs were over damped at all frequencies compared to the field output. Figure 47 shows that using 2.5% damping in the finite element model provides reasonable predictions of the 1σ response magnitudes for all three methods. The response PSD from the input acceleration PSD generated is aligned with the field results but under predict above 250Hz. The displacement PSDs (omega and integration response) have the correct trend but under predict above 250Hz and still have some excess spectral peak at the natural frequency between 60-70Hz. This frequency represents the attached payload. Above 70Hz the rover is under damped and the omega arithmetic method over predicts the response due to the payload, the reasoning for this is further discussed in Section 4.2.1. Figure 48 compares the difference in the response PSD values for the omega and the integration displacement methods. This comparison is evidence that the omega displacement PSD over predicts the response more than the integration PSD at frequencies less then 250Hz.

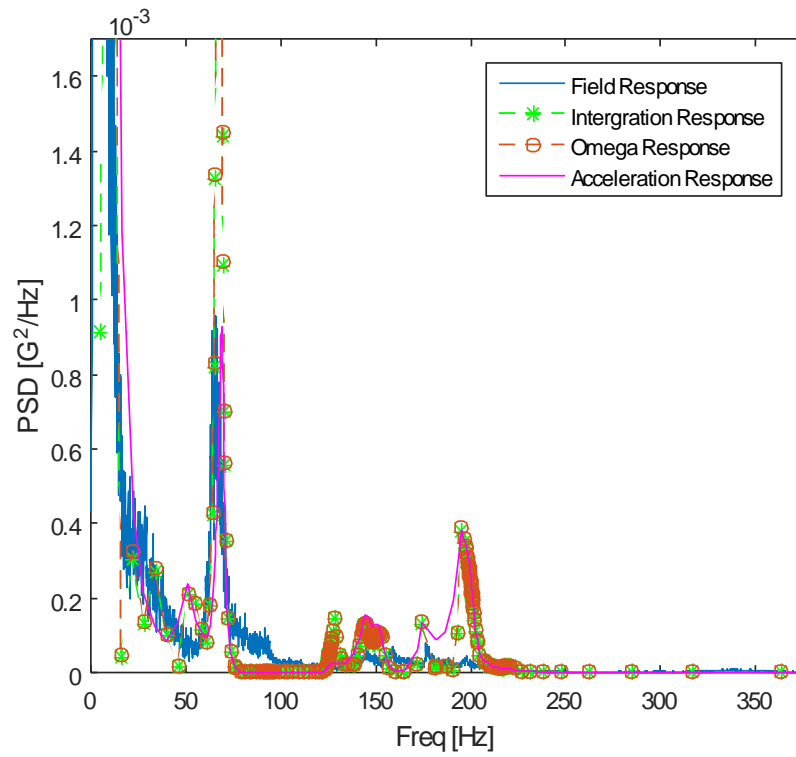


Figure 47: Output PSD for sensor 11Z field versus simulated response PSD at 2.5% damping.

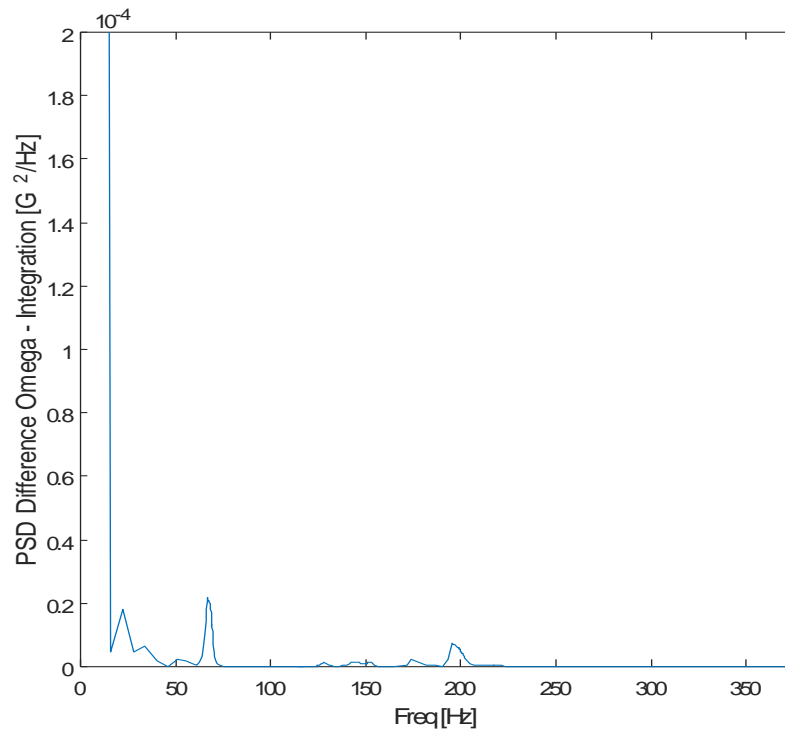


Figure 48: Difference in Output PSD magnitude for 11Z omega method versus integration method generation

The general trend in all simulations and the field data is the same but it can be seen that the magnitude of the simulation peaks are greater than the field data. This is due to the fact that the FE simulation predicts and outputs the 1σ response PSD of the rover. This means it is expected that the actual response PSD would be within or below the FE simulated results 68.3% of the time. The goal of the generated PSD and FE model is to have a 3σ response PSD that contains 99.7% of the field data. If the FE model was able to predict the response perfectly, there would only be 75 out of 25,000 points from the field data that are higher than the predicted response PSD. The FE results being higher than the field data means that the predicted response PSDs are conservative using 2.5% damping. The only downside of this is that the rover would be overdesigned at these frequencies.

It is difficult for finite element simulations to accurately represent damping of a structure as one constant damping value is applied to the entire model. The individual damping that is different for each component and interface cannot be represented in the model through system damping. While low frequencies are able to be addressed through system damping, damping at the higher frequencies would need to be addressed through geometry refinement. Low frequency modes are the main structure vibrations and movement, and high frequency modes are affected by the vibrations of the on board components such as fasteners, brackets and the DAQ system. Without these additional fasteners and brackets, discrepancies in the response PSD of the FE model versus the field data are expected. For this research, these geometric details were not included, but they could be added to the Baseline Model in the future for higher fidelity simulations. For this study the Baseline model used 2.5% damping, however to further develop the model more work on damping is required.

4. Results

The results are presented in two main sections; FE model verification and input PSD evaluation. The FE model verification looks at the effectiveness of the model geometry and ability to use the wheel hub output PSD as an input. This includes the comparison between the FE baseline model response PSD and the field response PSD. The input PSD evaluation assesses how effective the developed input displacement and acceleration PSD is in predicting the response PSD of the rover.

4.1. FE Model Verification

To ensure that the Baseline FE model was able to predict the random vibration response of the rover a known response PSD provided by the CSA for the wheels (1Z) was applied. The predicted response PSD was compared to the field data response PSD at other locations on the rover's chassis. Comparing a location that is the furthest away from the input point (11Z) on the chassis it was verified that the response PSD trend and magnitude aligned with the field data response PSD. The predicted modes of the rover were also compared against the generated response PSD to determine the speed and geometry dependent spectral peaks.

4.1.1. Input for Model Verification

The model's geometry could be verified using the accelerometer's data directly at the wheel hubs (1Z, 3Z, 5Z and 7Z), shown in Figure 49 as an input since all other accelerometer locations are secondary vibration path locations. Since a PSD is a statistical probability of vibration's magnitude, the same PSD can be used as input for all 4 wheels. For this reason it was a valid starting point to use the acceleration PSD from the 1Z accelerometer at the wheels provided by the CSA given in Figure 50, in which the payload was present on the rover for data collection unlike in the raw data used to generate the acceleration PSD from Figure 39 of Section 3.3.1.

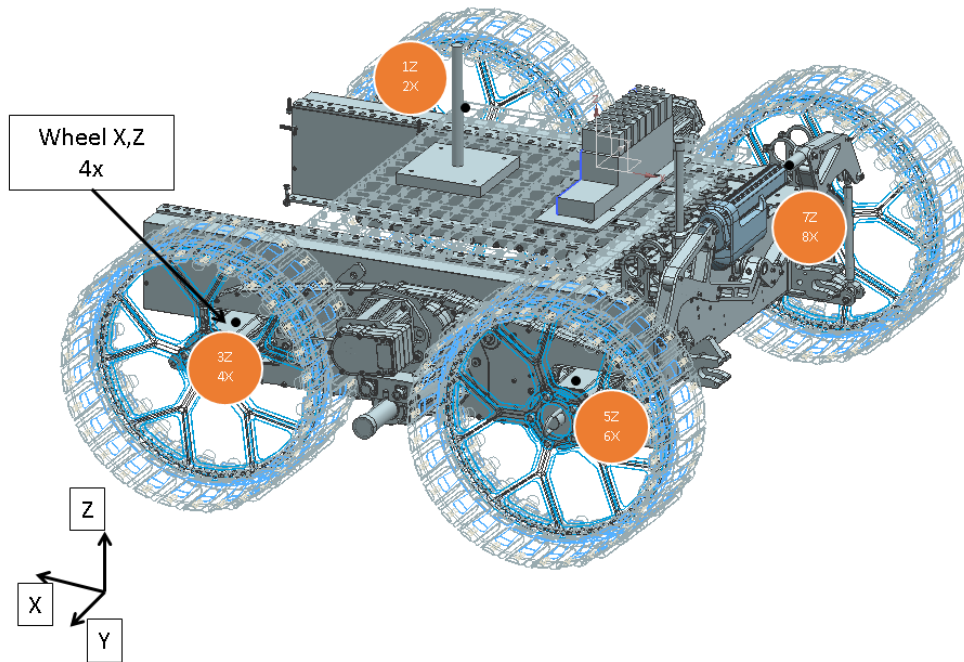


Figure 49: Base accelerometer locations on Juno's wheels, adapted from CSA [5].

Figure 50 shows large spectral peaks that are below the 5.12Hz cut off frequency that is applied to the generated displacement and acceleration input PSD. These large peaks are most probably a function of the rovers speed. The low 0.025Hz was discussed in Section 3.3 as the rise and fall of the rover over the 200mm aggregate. The peaks at 0.5Hz and 5Hz are most likely due to the rover's wheel diameter at 575mm and a maximum travelling speed of 3.2km/hr (889mm/s). As described in Section 2.3.2.2 the frequency is a function of the wheel diameter and speed.

$$f = \frac{\text{Rover Max Velocity}}{C_{tire}} = \frac{889 \left[\frac{mm}{s} \right]}{3612 [mm]} = 0.25Hz$$

This would indicate the second harmonic of the wheels is 0.5Hz at the rover's max speed of 3.2km/hr. The amplification at 5Hz could be due to the 10 spoke rims amplifying this harmonic.

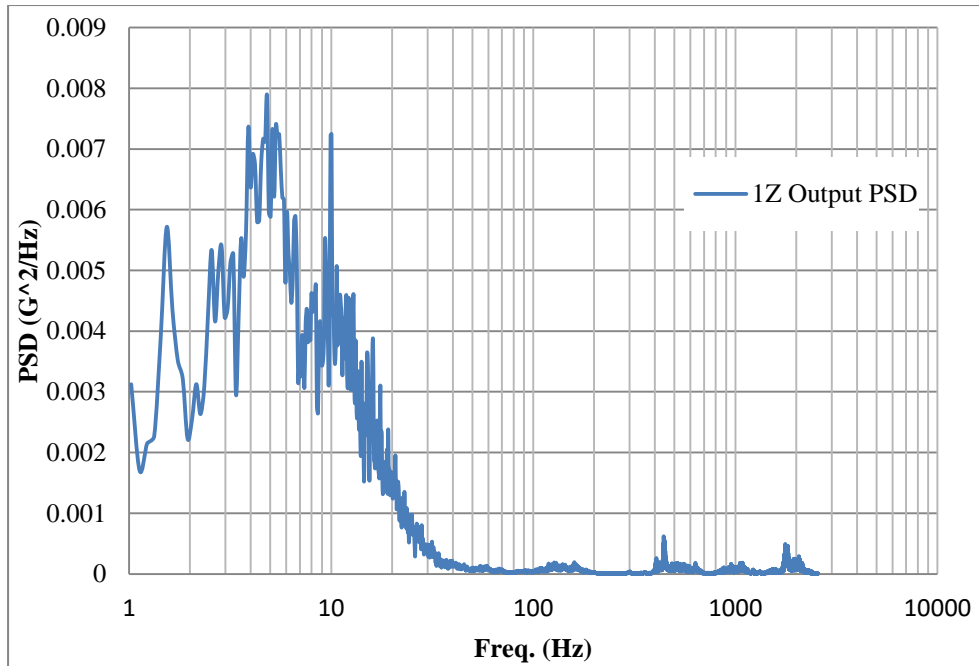


Figure 50: 1Z output PSD provided by CSA from BR5 (D) [5]

Since the CSA output can be understood it is acceptable to use the 1Z provided output PSD as an input, knowing the limitation that at the low frequencies less than 5.12Hz there is noise introduced by the rotation of the wheels and the periodic motion of the rovers full body rise and fall as a function of speed, which can be filtered out using a lower cut off frequency. Additionally the magnitude of the response PSD at locations secondary to 1Z, 3Z, 5Z, and 7Z, may be skewed by using 1Z as an input but the general trend and shape should be the same.

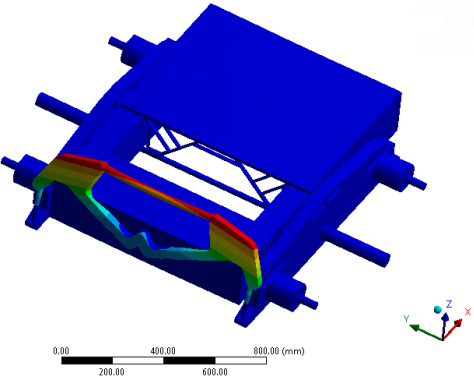
4.1.2. Baseline Model Analysis

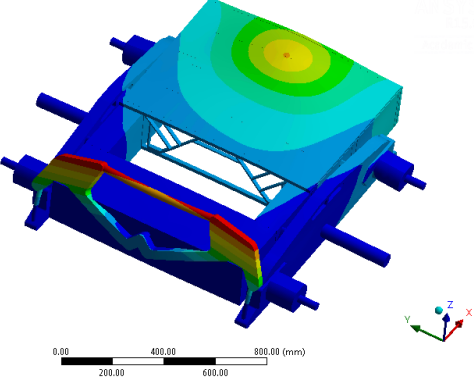
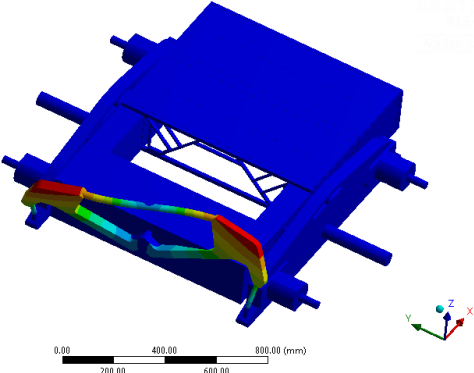
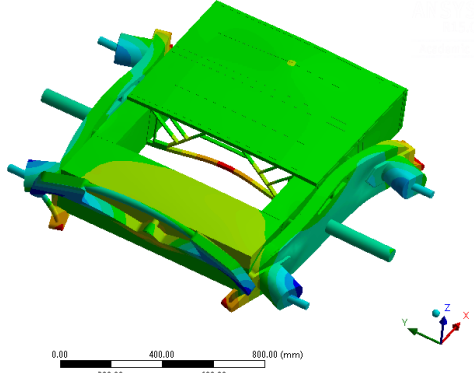
To verify the Baseline FE model the predicted natural frequencies from the modal analysis were compared against the spectral peaks of the generated response PSD and the generated response PSD compared against the field data. The first 20 modes predicted from the Baseline FE model are listed in Table 14. Table 14 was generated by restricting the wheel interfacing shafts to zero DOF in the z and x direction. The first mode is the rigid body motion of the rover, in the unconstrained y direction with an expected value of zero.

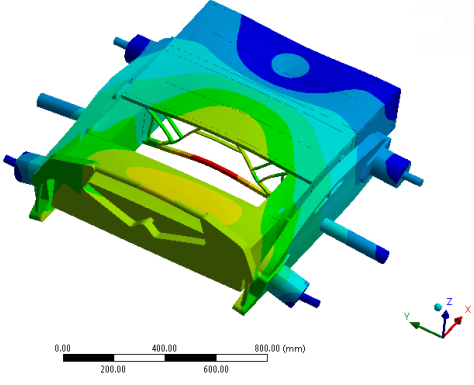
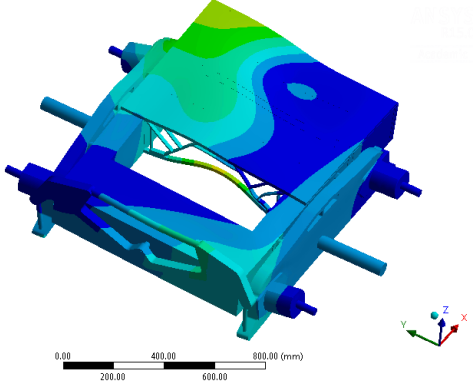
The second mode is the motion of the actuator mounted to the rear of the rover. This second mode could be refined through perfecting the actuator geometry but

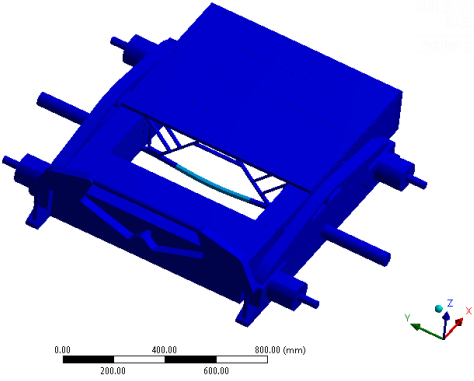
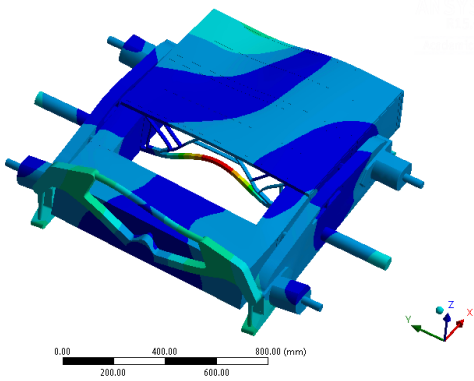
since there are no accelerometers or vibration readings taken near this section of the rover improving the accuracy of the geometry would not significantly affect the measured response PSDs. The third mode of the rover is due to the payload mounted to the mounting plates, and is visualized in Table 14. Mode 4 is the rotational motion of the rear actuator about the z-axis putting a torsional load on the joints mating to the drive arms. More significant motion occurs at modes 5, 6, 7, 8, and 14. These modes are where the wheel motor moves out of the z-x plane and the body of the rover acts like a flat plate under free vibration. Modes 5, 6, and 7 are also the modes seen in Figure 50, the CSA response PSD, as spectral peaks from 125-150Hz. Modes 5 and 7 are the torsional motion of the suspensions arms in the z-axis with a motion of the wheel motors in and out of the z-x plane. Mode 6 is the motion of the entire rover acting like a plate in free vibration and the front mounting plate and the rear of the chassis move in on out of the x-y plane 180° out of phase with each other. Mode 8 and 9 show the torsional motion of the entire rover about the x-axis. Mode 15 is the twisting of the chassis from corner to diagonal corner, all other modes within the first 20 where the motion of the cross sectional supports or the rear actuator.

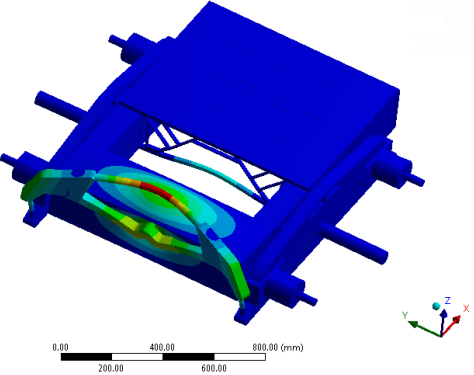
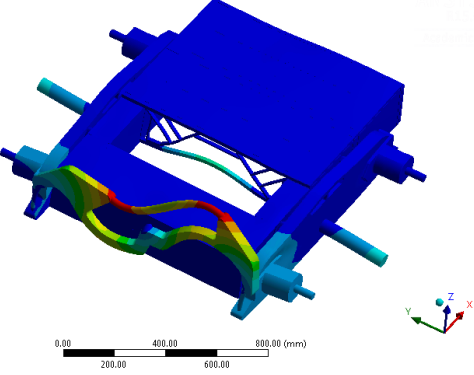
Table 14: Juno rover modal analysis 8x Scale.

Mode	Frequency [Hz]	Deformation	Motion
1	0.001137	Rigid Body Z	Full body.
2	66.913		Rear actuator about y-axis.

Mode	Frequency [Hz]	Deformation	Motion
3	68.94		Payload motion in z-axis. Rear actuator motion about y-axis.
4	92.603		Torsional motion of rear actuator along z-axis.
5	125.35		Torsional motion along z-axis, for drive arms.

Mode	Frequency [Hz]	Deformation	Motion
6	144.44		<p>Torsional motion along x-axis, for drive arms. Plate buckling under payload motion.</p>
7	150.19	Similar to mode 5	Torsional motion along z-axis, for drive arms.
8	199.1		Torsional motion along x-axis.
9	200.64	Similar to mode 8	Torsional motion along x-axis.

Mode	Frequency [Hz]	Deformation	Motion
10	216.7		Cross section supports bending.
11	219.14	Similar to mode 10	Cross section supports bending.
12	219.35	Similar to mode 10, 11	Cross section supports bending.
13	221.28	Similar to mode 10, 11, 12	Cross section supports bending.
14	225.51	Similar to mode 8 and 9	Torsional motion along x-axis.
15	257.45		Twisting of main body.

Mode	Frequency [Hz]	Deformation	Motion
16	258.34	Similar to mode 10, 11, 12, 13	Cross section supports bending.
17	262.27		Rear chassis buckling. Rear actuator bending.
18	273.82	Similar to mode 10, 11, 12, 13, 16	Cross section supports bending.
19	277.8		Torsional motion of rear actuator along x-axis.
20	282.05	Similar to mode 10, 11, 12, 13, 18	Cross section supports bending.

To verify the FE model the main modes that are identified by the field data PSDs must also be seen in the FE model response PSD. Comparing the response PSD from the field data at location 11Z on the chassis to the FE predictions in Figure 52 the FE model is valid. Location 11Z on the chassis was chosen because it has the farthest path for the vibration to travel as it enters the model at the wheel hubs, then travels along the drive arms through the drive shaft and along the outer frame of the chassis as depicted in Figure 51. This path is important because any deformation and modes along that path will show up in the response PSD output from the FE model.

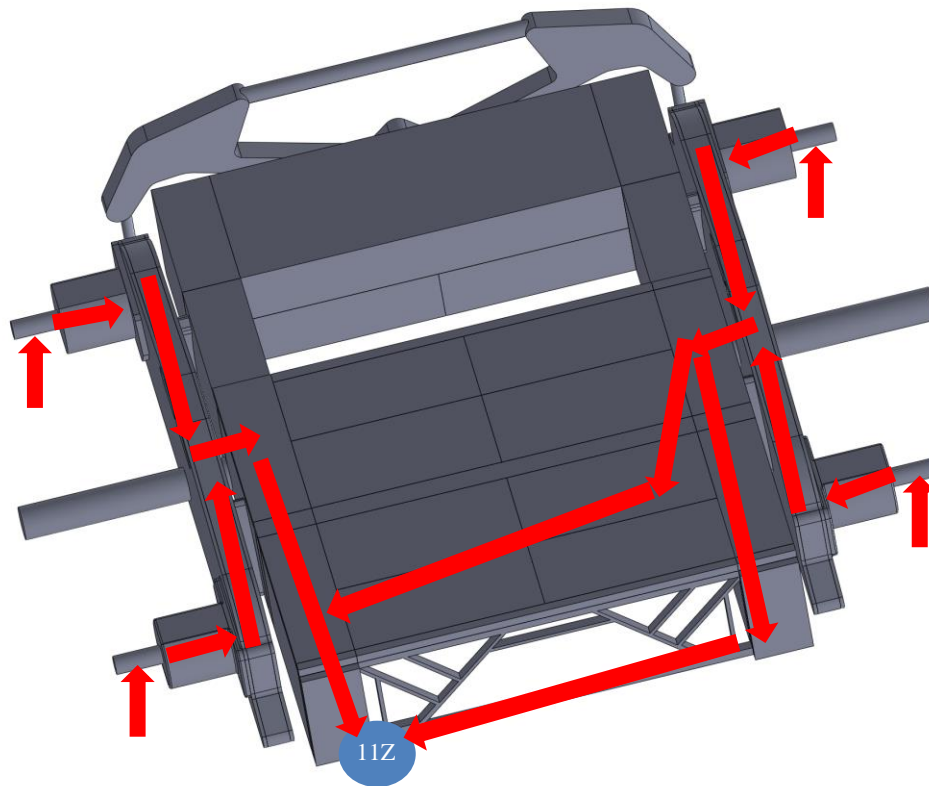


Figure 51: Visual representation of vibration path to location 11Z on chassis

The payload motion is a spectral peak in the response PSD between 60-70Hz, shown in Figure 52. The response PSD curves for the Baseline model created in Figure 52 are the 1σ curves taken directly from ANSYS output with 2.5% damping applied to the rover. The higher modes are the movement of the drive arms, the rear actuator and the full body plate like motion of the rover. Reviewing these

higher frequencies, the model is under predicting the magnitude of the response but, the general trend can still be seen above 84Hz. This is likely due to geometry simplifications in the area around 11Z as fasteners and brackets are not accounted for and would be the components that have a response to these higher frequency excitations. Additionally note that the FE model response PSD does not start until 10.24Hz due to the lower cut off frequency used to generate the acceleration PSD. This was to avoid the spectral peak around 5Hz due to the wheel rotation as a function of speed as discussed.

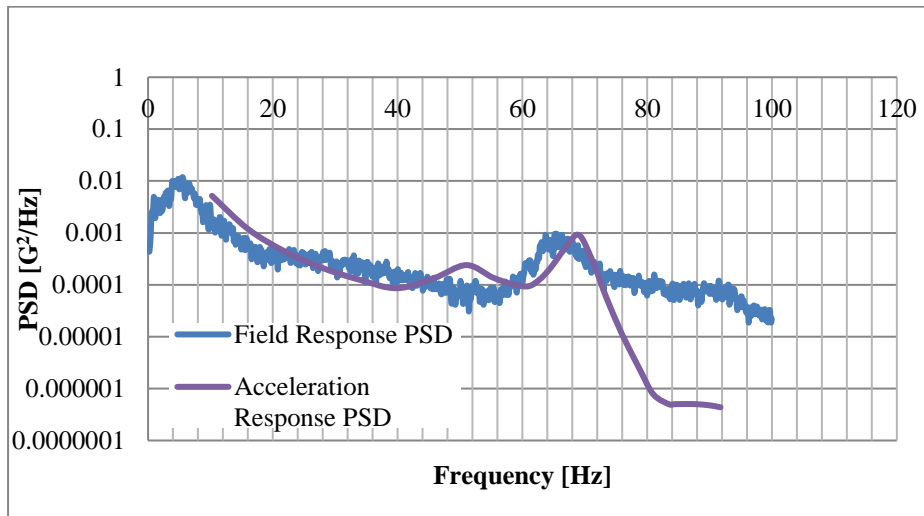


Figure 52: Comparison of field data to simulated data at chassis location 11z.

In summary, based on the FE model response PSD using the raw acceleration data from 5Z to generate an input PSD the FE model is able to accurately model the magnitude and trend of frequency vibration and large body motion, as the maximum difference in simulation to field results under 70Hz is $3.6 \times 10^{-3} \frac{G^2}{Hz}$ for the 1σ results at 10.24Hz. At higher frequencies the model is able to provide accurate trends for the response PSD but the magnitude of the response is skewed due to geometry simplifications. In Section 4.2 more location's response PSDs will be reviewed with each of the input PSD types to see the validity of the input PSDs. This study will also show if locations closer to the input vibration or further from small components (components more easily impacted by high frequency vibration) will have a more accurate response at the higher frequencies.

4.2. Input PSD Evaluation

The effectiveness of the input displacement PSDs that were developed in Sections 3.2 and 3.3 were evaluated through comparison between the predicted response PSD from the Baseline FE mode and the field response PSD at six locations on the rover. When performing a random vibration analysis, ANSYS outputs the 1σ response PSD with mean removal. Since a mean removal is used, the 3σ response graphs shown in this section were determined by multiplying the ANSYS output by three. Referencing Figure 26, the probes at 10Z and 12Z are not shown as they are approximately equal to 9Z and 11Z respectively. This is due to the rover being symmetrical and driving over level terrain all of equal sized aggregate. The joint location of the drive arms to the rover frame are represented by 9Z, 11Z represents the front frame of the rover body which is the furthest measurements from the input vibration as described in Figure 51, 29Z is at the location of the payload and 15Z is the center of gravity of the rover.

Reviewing Figure 53 the response PSD for each of these locations against the field data shows that the field data is reasonably contained within the 3σ for all input methods up to 200Hz which is representative of the rover absolute motion. This means the large body motions and impacts of the rover are captured. In the frequency band from 80-120Hz there is some under prediction by the FE model on locations 11Z and 12Z. Similarly the band from 80-90Hz is under predicted at locations 9Z and 10Z. Predicted response PSDs from the FE model match up with the general trend of the expected response from the CSA field data, except probe 29Z shown in Figure 54.

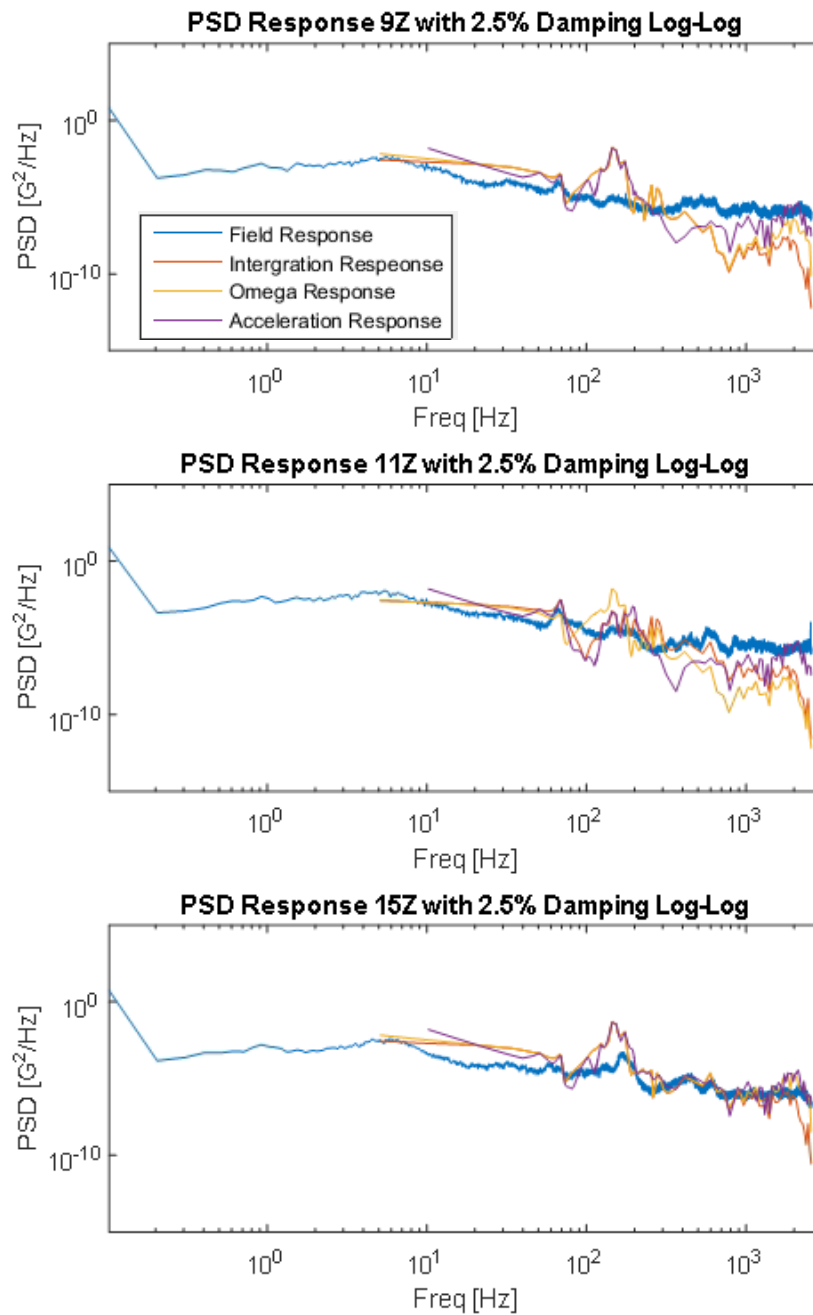


Figure 53: Z-axis 3σ simulated response PSD comparison with field data generated response PSDs with 2.5% damping used in the FE modelling.

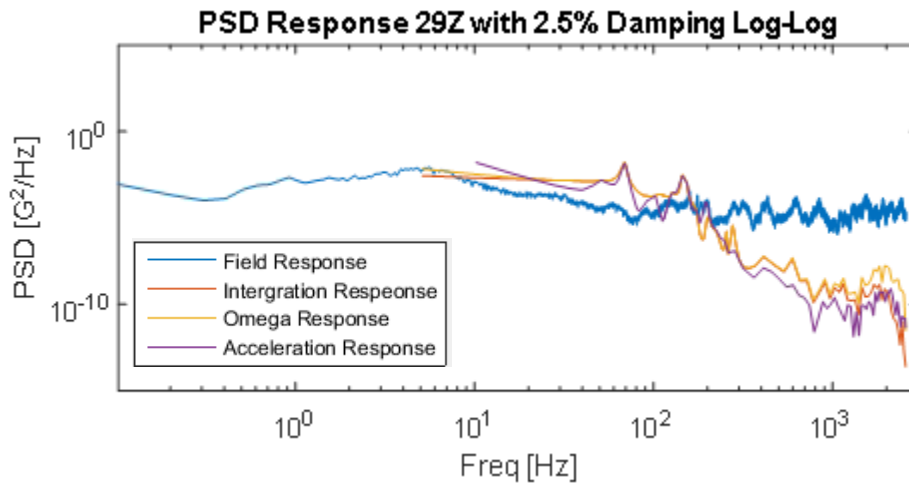


Figure 54: Payload Z-axis 3σ simulated response PSD comparison with field data generated response PSDs with 2.5% damping used in the FE modelling.

More carefully analyzing the response PSD at 9Z the under prediction of the vibration at 80-90Hz is likely due to the simplified actuator. The joint between the actuator and the drive arm, highlighted in Figure 55, is represented by a single cylinder. In reality there is a gas spring making the connection between the actuator and the drive arm, this would apply a continuous force against the drive arm at the rear stiffening the structure. This increased stiffness and applied force likely loads the drive shaft and increases its response to an applied vibration. For similar reasons a spectral peak is seen around 150Hz. Modes 5, 6, and 7 are all in the 125-150Hz range and are the motion of the drive arm about the drive shaft where probes 9Z and 10Z are located. In the FE model the drive is connected directly to the chassis whereas in fact there is a mounting joint that connects the drive shaft to the chassis and supports it, this comparison is shown in Figure 55. The model creates a false freely cantilevered cylinder that would over predict the effects of vibration in this area, making the model conservative.

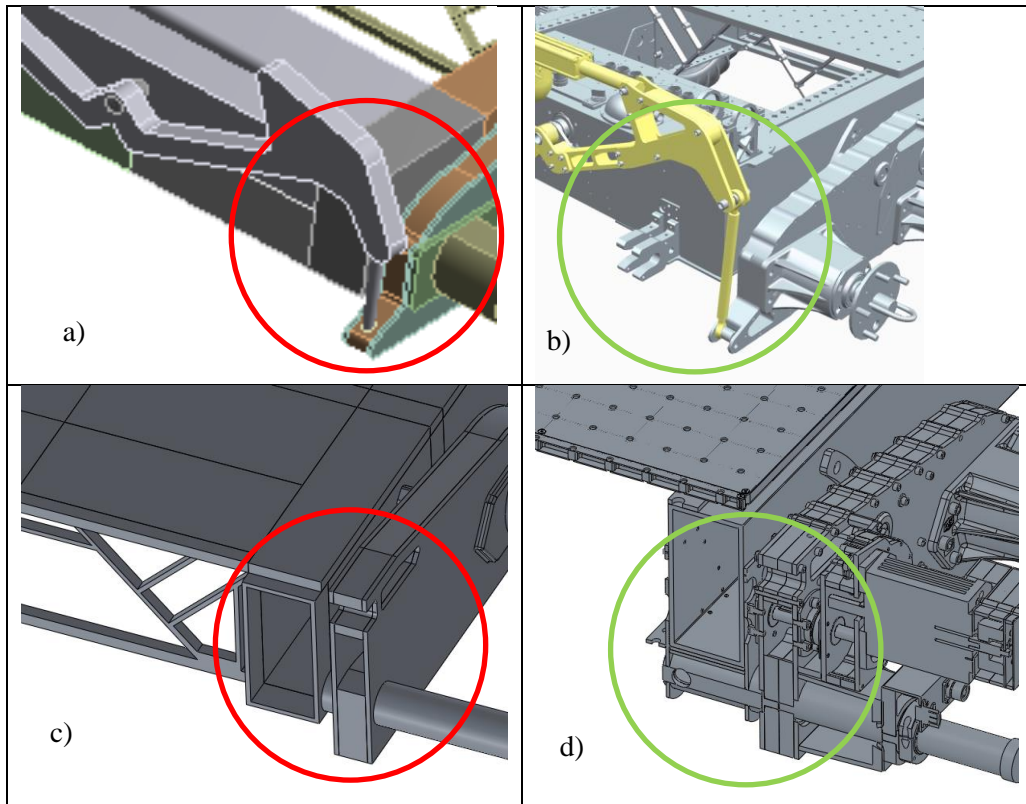


Figure 55: Actuator mounting point to drive arm actual comparison to FE model simplification provided in a) and b), connectional axel joint simplification provided in c) and d).

As touched on in Section 4.1.2, 11Z at the corner of the rover's chassis under predicts the response PSD. This is likely due to geometry simplifications in the area around 11Z as fasteners and brackets are excluded. The FE model treats the rover's chassis as one uniform 6.35mm (1/4") thick aluminum shell. This makes the body less prone to high frequency excitations, and modes 4 and 5 are the two main contributors to this frequency band which are the motion of the drive shaft and drive arms. With the chassis as a single solid shell the vibration energy in the FE model is damped. In the field it is more likely that given the bottom and sides of the chassis are fastened together with many brackets and the mounted cross sectional supports the vibration would play a greater impact.

As the frequencies exceed the absolute motion of the rover, and become the relative motion of component's to the rover's vibration a deviation with probe 29Z, the payload location, can be understood. The fundamental frequency impacting this location is at mode 2, 68Hz. This is where the payload begins to flex the mounting plates like a trampoline, at this low frequency the payload does not "pull away"

from the plate, but moves up and down with it. At 125Hz (Mode 4) the payload area is again impacted by the vibration and treats the plate like a trampoline. The reason the FE model deviates and under predicts the response PSD at this point is because in the simulation the payload is a direct attached point mass moving with the plate in unison. In the field the payload was a 37kg dumbbell mounted to the front plate of the rover.

At these higher input frequencies above 125Hz the dumbbell would begin to vibrate out of phase with the mounting plate. This produces a secondary input vibration from the payload due to relative motion between the mounting plate and payload. This secondary input would be based on the inertia and geometry of the payload plus the fastening of the payload. Depending on the damping and torque of the fasteners there would be additional vibration energy. These factors lead to the poor predictions of the FE model at frequencies above 125Hz at location 29Z.

As a final check to confirm the models validity the data from the accelerometer at the center of gravity, 15Z, is compared against the simulated data, and shows that the accelerometer data is within 3σ for values less than 1000Hz as seen Figure 53. This point on the rover is able to align the field and simulated data even at the high frequencies because in reality there are no components mounted near this area that would have modes at the higher frequency adding additional vibration energy.

As random vibration can only be described in terms of probability it is not expected that the field data will look identical to the simulated data or that two field runs would look identical. It can be expected that there is a spectral peak at each mode and using the simulated response PSD with 3σ probability level that 99.7% response PSD would be equal to or less than the simulation's response PSD. The probes at 9Z, 10Z, 11Z, and 12Z all follow the general profile of the field data, but with 25000 sample points only 75 points should be expected to exceed the simulated response, if the model was a perfect representation of the field test. As the model did not contain fasteners, thin and slender geometry or attachment points the simulation is under predicting the magnitude of the response PSD. Since the center of mass, 15Z, shows very probable results it can be said the input PSDs are valid and the geometry limitations are the source of the high frequency limitations of the predicted response.

4.2.1. Generated PSDs

The two displacement PSDs that were generated using the Omega Method and Double Integration Method were shown in Figure 42 and Figure 45. They are both created using the same raw accelerometer data and both show the same general decreasing trend in magnitude as frequency increases. As discussed previously in

Section 4.2, and seen in Figure 54 both methods can reasonably represent the 200mm terrain. The output PSDs generated by the two methods are compared in Figure 56.

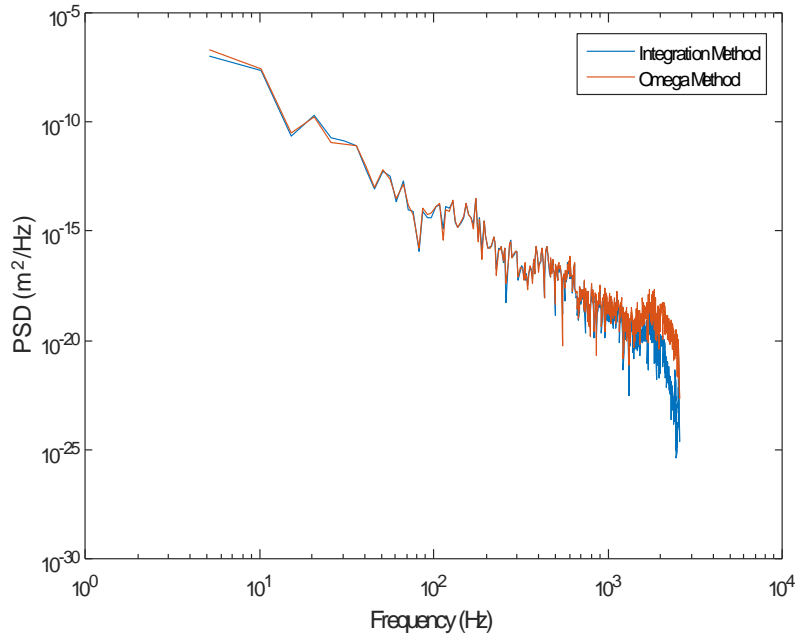


Figure 56: Generated input PSD comparison between Double Integration Method and Omega Arithmetic Method of displacement

Both methods are in agreement until the 1000Hz range when the omega method has GRMS values in the $10^{-22} \frac{m^2}{Hz}$ range whereas the integration method is in the $10^{-25} \frac{m^2}{Hz}$ range. The order of magnitude is very small however, this is due to the vibration energy being small. The rover is driving slowly over a well compacted terrain. If the rover were seeing more violent vibrations at high frequency the three orders of magnitude difference in the input PSD would have major impacts on the rover's response PSD and change the rover's design requirements. An example of when these higher frequencies would have a more significant magnitude would be launch and landing on the planet, or when rovers begin to travel at higher speeds such as cars on the highway.

The difference in magnitude is likely due to the integration method breaking down at the higher frequency ranges as numerical drifting occurs. It is recommended that for frequencies below 1000Hz the integration method be used and for frequencies

above this range the omega arithmetic method used. This is recommended because the omega arithmetic method is mathematically more intensive than the double integration method. Additionally with the omega method as ω^2 gets smaller noise is generated, because ω^2 is in the denominator driving the displacement to infinity at low frequencies. This is mitigated by using an effective lower cut off frequency but can still be seen in Figure 56 as the omega method PSD increases more rapidly than the integration method PSD. With this combination of methods the degradation of the double integration method is avoided and the noise generated by the omega arithmetic method does not occur giving a consistent and reliable input PSD.

5. Discussion

5.1. Additional Model Evaluation

In order to verify the general functionality of the rover simulation the effects of geometry, loading, boundary conditions and mass distribution needed to be evaluated. The specific studies performed in the next three sub-sections are to verify the effects of geometry, loading, boundary conditions and mass distribution on simple body simulations to gain this knowledge.

5.1.1. Effect of Geometry on Response PSD

It was shown for the Initial and Baseline FE models that altering the geometry has a significant effect on the predicted modes and the response PSD. In order to understand the effects of how geometry impacts the response PSD to a given random input, a constant material was used with a white noise input spectrum shown in Figure 57 so that the effects under purely random vibration could be seen. The effect of the shape of a component was determined by considering three different shapes with constant volume and mass. The same white noise input, constant PSD, was used for each geometry; a cylinder, cube and rectangular prism. The geometries are shown in Figure 58. The red surface being the fixed surface the input PSD was applied to, and probe locations 1-8 identified.

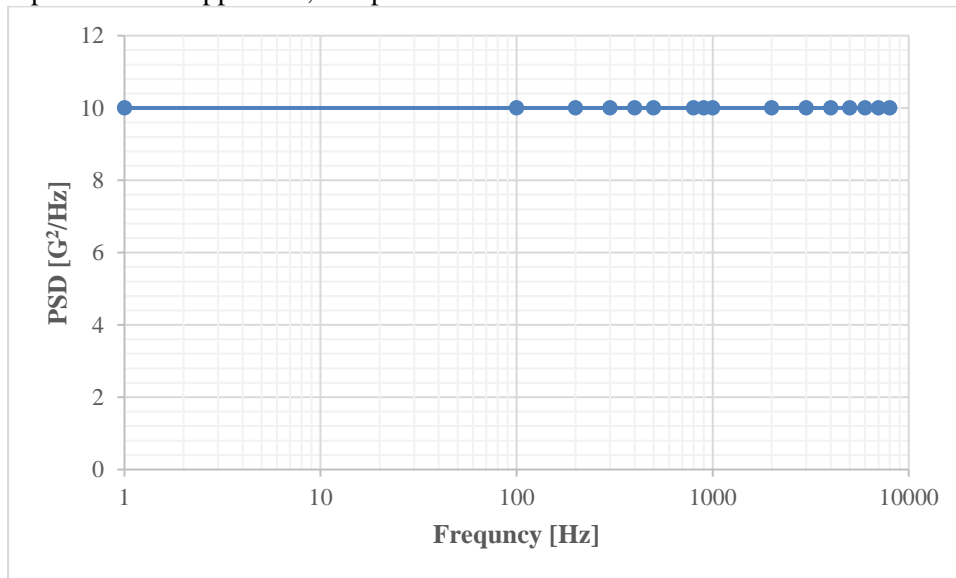


Figure 57: Constant PSD input (White Noise vibration input) at $10G^2/Hz$

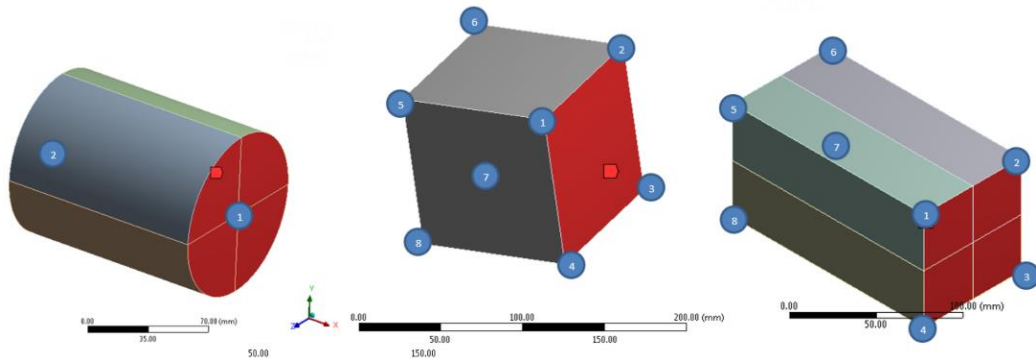


Figure 58: Geometry variation with approximately constant volume = $1 \times 10^6 \text{mm}^3$.

The first 5 modal frequencies are shown in Table 15 and the output acceleration PSD are given in Figure 59 for the three geometries. The first two modes of each geometry represented the bending modes about the Z and Y axes respectively. The third mode was torsional about the x axis, the fourth mode was compression along the x axis toward the fixed surface and mode 5 was the bending and flaring of the free end about the y axis for all geometries. The natural frequencies for the cube were the highest of the 3 geometries as it had the smallest length and the largest cross-section. The rectangular prism was the longest and had the smallest cross-section and therefore had the lowest natural frequencies.

The cylindrical model, looks only at the midpoint probes labelled as 1 and 2. This radial geometry causes many changes in the response but most important to consider is the drastic damping affect attenuating the response to a factor of 10^{-27} at low frequencies to a factor of 10^{-9} at peak. This attenuation is likely due to the cylinders smooth surface, the vibration carries differently across the surface of the cylinder because there are no concentration points generated by the 90° edges introduced by the cube. Even with this radial geometry the spectral peak can be seen, Figure 59, as the first and second modal frequency are approached $\sim 3500\text{Hz}$, Table 15, as well as the rise to mode 3 at 6160Hz and then continued increasing response as it approaches $10,000\text{Hz}$ but is cut off at the 8000Hz point due to input PSD.

The cube shows a unity gain in Figure 59 until a large spectral peak at mode 1 and 2, at 5300Hz . Mode 3 does not actively appear in the response PSD but this could be due to the response at 7293.5Hz being very small and the larger response due to mode 1 and 2 overwhelming the systems response. The rectangular prism with the same volume shows that as the first two modes are reached there is a spectral peak

in Figure 59. However, as mode 3 is approached at 5600Hz, from Table 15, that its spectral peak is relatively small in comparison to modes 1 and 2. This is because the third mode is a torsional motion, as shown in Figure 60, with small displacement effects relative to the input vibration. Again after mode 4 the response PSD begins to rise as it approaches mode 4, 5 and 6 which are above the 8000Hz input cut off. The rectangular prism is unlike the cube as it attenuates the vibration, because it does not have the rigidity of the cube which provides a unity gain.

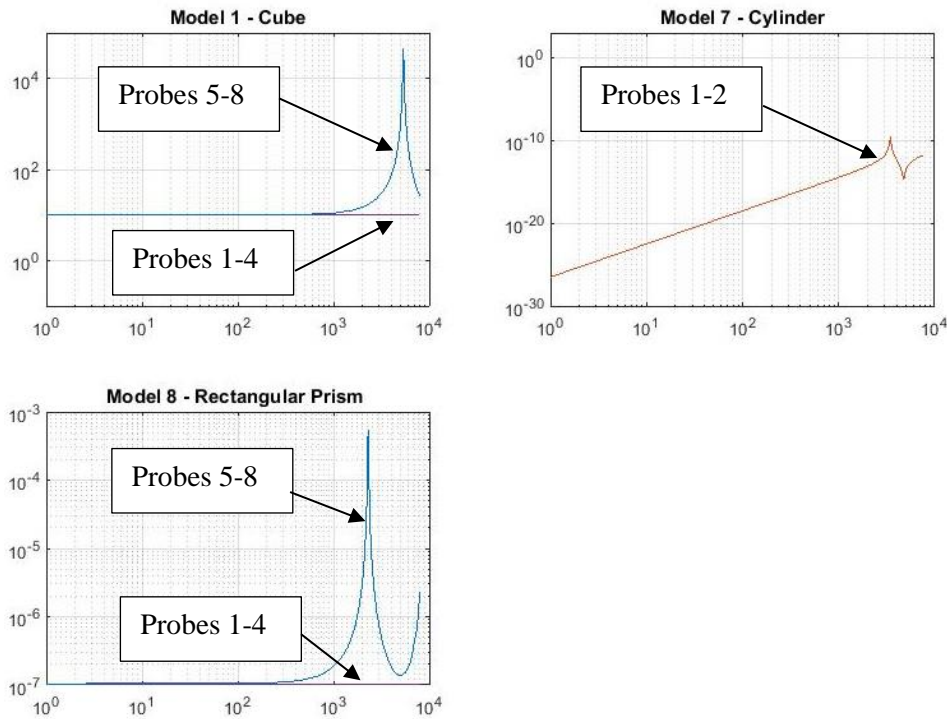


Figure 59: Response PSD spectrum for constant geometry, volume model and input PSD with different loading cases.

Table 15: Modes of simulated geometries.

Model	Cube	Cylinder	Rectangular Prism
Mode 1 [Hz]	5365	3459.4	2306.4
Mode 2 [Hz]	5365.9	3459.4	2306.4
Mode 3 [Hz]	7293.5	6162.2	5689.2
Mode 4 [Hz]	12822	10071	9770.3
Mode 5 [Hz]	14192	11196	9770.5

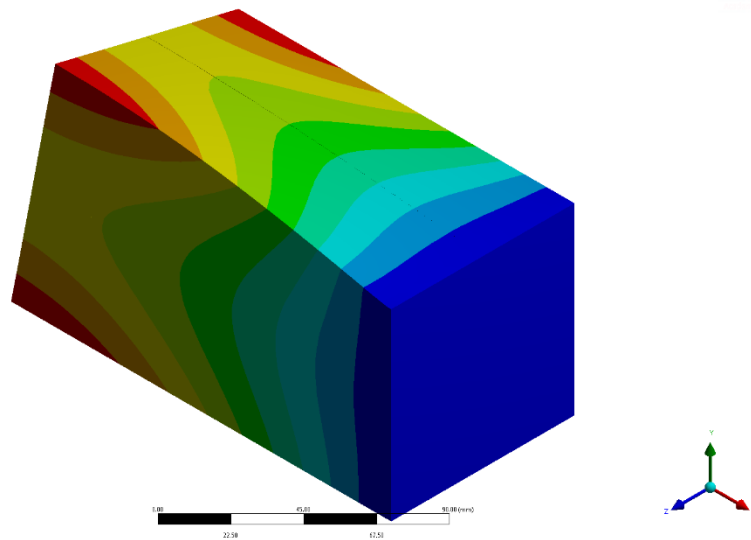


Figure 60: Model 8 mode 3, torsional deformation. Red represents areas of large displacement, and dark blue indicates zero displacement.

It is apparent from this study that the geometry of the structure has a direct impact on the response PSD. This is largely due to the modal frequencies based on the structure and the frequency band of the input PSD. In addition to this, the geometry impacted the structures stiffness changing the response to a given input frequency. It is a key finding to see that the geometry can not only cause attenuation of the response PSD but can also drastically change the profile of the response when the structures material, volume and input PSD are held constant.

The geometry affects the magnitude of the natural frequencies and the magnitude, frequency and shape of the PSD. It is important to have the geometry detailed to match the fidelity of response PSD desired. The higher the frequency band of interest the more detail in geometry required, for lower base motion frequency many simplifications can be made. It is a good finding that when looking to damp

out vibration the use of cylindrical cross sections are more attenuating than rectangular. This could be used to benefit the rover by replacing the rectangular cross section with a cylindrical sections to reduce the impact of vibration input to onboard instruments.

5.1.1.1. Effect of Rover Geometry on Response PSD

Using the two main models described in 3.2.1 Rover Geometry, Table 16 shows a comparison between the GRMS. Using the displacement generated PSD's the Initial and Baseline models appear very comparable at the 1σ level, and as this is with mean removal can be considered based on the similar trends to be the same. However, looking at the direct accelerometer input response of the Initial model to the Baseline model there is approximately a factor of three difference in the response PSD GRMS. Also in the Initial model there is a factor of three difference in the accelerometer input to the displacement PSD inputs. This difference is likely due to the incorrect geometry and transfer of vibration energy from the ground to the rover's chassis. In reality the rover has two large masses, the drive arms, on either side of it which dampens some of the vibrational energy before entering the chassis. In the accelerometer input the response energy from the ground into the wheel motors is being directly applied to the chassis without the drive arms damping the input. Whereas in the Baseline model the energy seen at the wheel motors is properly transferred into the chassis. The displacement generated PSDs do not have the same anomaly because they are direct representations of the motion that the ground would apply to the chassis if the chassis was riding along the terrain surface. This shows the importance of model geometry to accurately simulate the system response is even more critical when using acceleration input PSDs.

Table 16: Overall GRMS comparison of Initial to Baseline model.

Input PSD	Response PSD GRMS	
	Initial Model	Baseline Model
Displacement Input from Omega Method	0.26619 G	0.24802 G
Displacement Input from Integration Method	0.18527 G	0.22639 G
Accelerometer Input	0.62155 G	0.20989 G

5.1.2. Effect of Loading and Boundary Conditions on Response PSD

By varying the loading and boundary conditions on models of identical geometry the effects of using different input surfaces and fixing different faces can be understood such that the most accurate model setup could be created for any input PSD. A solid steel cube with length= width = height =100mm was used to determine the effects of different loads and boundary conditions on the response PSD.

5.1.2.1. Boundary Condition Variation

Three boundary conditions were evaluated by applying an input PSD on the 1-2-3-4 and 1-4-8-5 surfaces. Model 1 fixes the 1-2-3-4 surface and applies the input PSD in the z direction on this face. Model 2 uses the conditions of Model 1 but, also fixes the 1-4-8-5 surface. Model 3 uses the conditions of Model 2 but, applies the input PSD to both of the surfaces 1-2-3-4 and 1-4-8-5 in the z direction. The modes and response PSD are given in Table 17 and Figure 62 for probes 1 through 8, for each model. When the cube is restricted on the secondary surface the first mode becomes the bending motion of the 6-7 edge about the diagonal of the x-z plane, as well as the fifth mode. The second mode becomes the elongation in the x direction, third mode is torsional motion about the x-axis and the fourth mode is compression of the 6-7 edge towards the 1-4 edge. From Table 17 the modes for models 2 and 3 are the same. This is because the modes are only impacted by the boundary conditions, such as giving the surface zero DOF. The resulting PSDs are different in Figure 62 because the input PSDs are different.

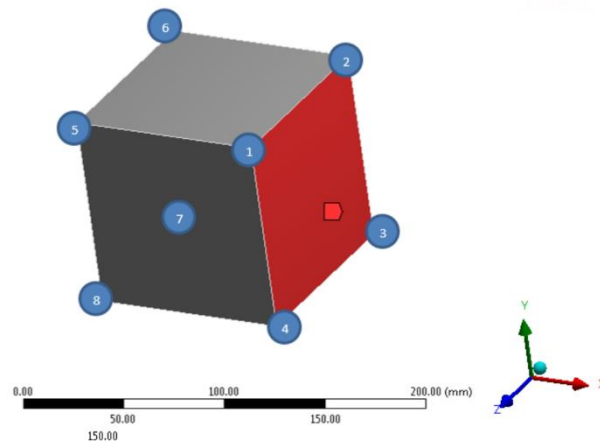


Figure 61: Solid steel cube with response PSD probes used to determine relationship between input and response PSD based on varying loading faces.

Table 17: First five modes due to varying PSD input on a constant geometry.

Model	1	2	3
Mode 1 [Hz]	5365	8141.1	8141.1
Mode 2 [Hz]	5365.9	12532	12532
Mode 3 [Hz]	7293.5	14429	14429
Mode 4 [Hz]	12822	15872	15872
Mode 5 [Hz]	14192	17346	17346

In Figure 62, the spectral peak near the 5300Hz for Model 1 is dominant as it is the fundamental frequency of the steel block and the first two modes are in this range, given in Table 17. This excitation is seen in probes 5 through 8 which a reasonable expectation as probes 1-4 are on the fixed face, shown in red of Figure 61, where the input PSD is being applied hence the unity gain so the response is the same as the input at $10G^2/Hz$.

In Model 2 when the 1-4-5-8 plane is also fixed with only an input applied to 1-2-3-4 face, damping and attenuation is induced in the response PSD by an order of magnitude from the unity gain location, Figure 62. Additionally because of the two fixed surfaces the mode frequencies of the Models 2 and 3 change and the fundamental frequency changes to approximately 8100Hz. Probes 6 and 7, the free probes, can be seen rising to a spectral peak when the new fundamental frequency is approached. The probes at 5 and 8 are not shown as they had zero response across all frequencies, this is because they are on a face edge held fixed relatively far from the input PSD. When the input PSD is applied to the 1-2-3-4 and 1-4-5-8 surfaces in Model 3 the attenuated response in probes 6 and 7 returns to a response rise, Figure 62, leading up to the first mode 8141.1Hz given in Table 17. The probes at 5 and 8 are also brought to unity gain as the 1-4-5-8 plane is now an input surface.

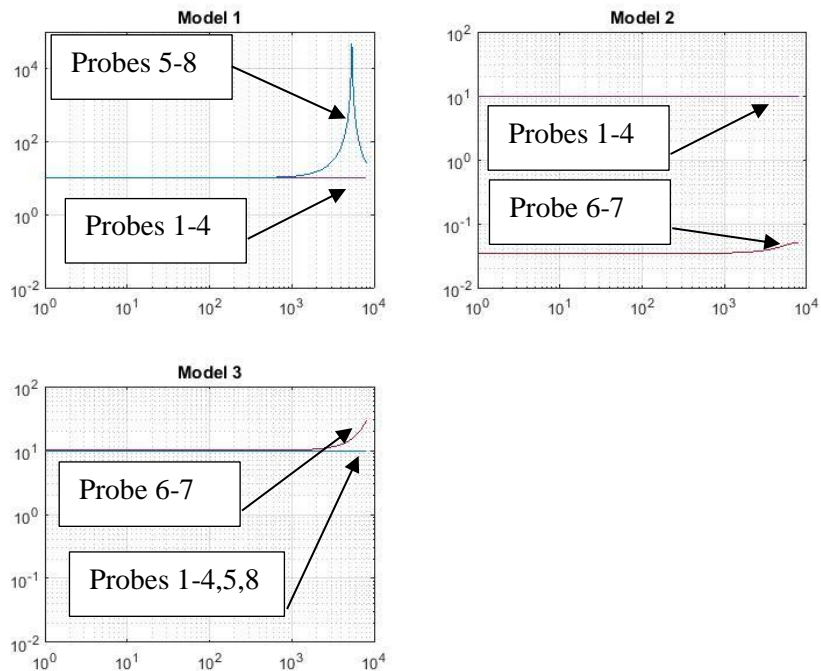


Figure 62: Response PSD spectrum for constant geometry and volume model with different input PSD variations.

From this study is understood that the free features of a structure are directly impacted by the input and fixed boundary conditions. Improperly fixing or bonding of a surface can lead to a response PSD spectrum of the wrong trend and magnitude invalidating the model results. For this reason it is not recommended to use symmetry to reduce computational time. The rover is symmetrical and could have been split along its center line and fixed at the middle, applying the input PSD to only the right or left side set of wheels. However, this would have induced a false damping at the mid-point of the rover and attenuated the vibration throughout. This attenuation would under predict the response PSD of the rover and if designed to this could lead to unexpected failures due to vibration levels tested in the simulation.

5.1.2.2. Loading Variation

Model 9 and 10 use the same boundary conditions as Model 1 from Section 5.1.2.1 by fixing the 1-2-3-4 surface and applying the input PSD in the z direction on this face. These models apply a deformable point mass offset to the cubes center line,

shown in Figure 63. This means the mass can move out of phase with the cube as the cube and mass vibrate due to the input PSD. Model 1 has no additional mass, Model 9 uses a 1kg load offset 25mm from the center of the cube in the Z direction, and Model 10 uses a 100kg point load offset the 25mm in the Z direction.

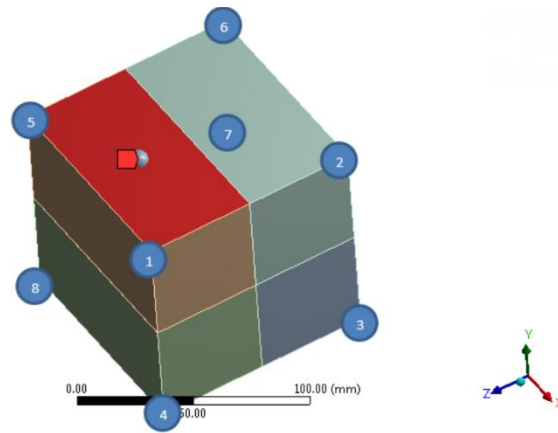


Figure 63: Solid steel cube with response PSD probes used to determine relationship between response PSD and unbalanced loading based on a point load.

The modes of the 1kg mass and the cube without a mass are near identical. The first two modes represent the bending modes about the z and y axes, the third mode is torsion about the x axis, fourth mode is compression along the x axis and the fifth mode is the bending of the free end about the y axis. When the 100kg mass is added to the cube the deformation and direction is heavily biased to the location of the mass. Modes one and two still represent bending but a twist is also present in the cube as a moment is generated by the mass. Mode three is the deformation of the mass into the cube, while four and five are the torsional motion of the cube about the x axis.

Model 1 and Model 9 have a very similar response PSDs as seen in Figure 64. This is due to the mass being relatively light. While graphically the two are similar with a peak around 5000Hz, Table 18 shows that Model 9 has a 300Hz reduction in the first two modes compared with Model 1. This shows that applying a mass to the structure will damp the response PSD. Additionally Model 9 has noise generated above the first mode as the mass begins to vibrate out of phase with the cube.

Model 10 has a drastic change in the mass distribution reducing the first two modes by a factor of more than 4. Even the higher modes are reduced by a factor of 1.2-2. This reduction of higher frequencies is due to the mass damping the systems

response. Spectral peaks in Figure 64 aligned with the first four modes given in Table 18 but significant attenuation can also be seen and is due to the unbalanced deformable load vibrating out of phase with the overall structure and the rotation deformation of the structure. This out of phase motion causes the structure at certain frequencies to damp out the input vibration.

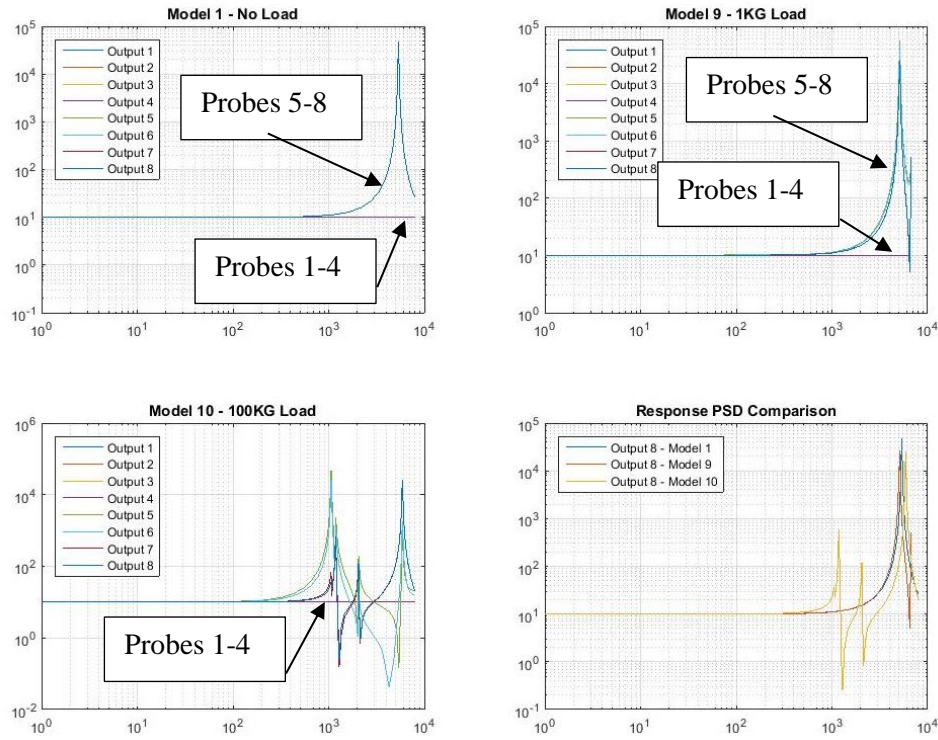


Figure 64: Response PSD spectrum for constant geometry, volume model and input PSD with different loading cases.

Comparing the output at location 8 for the three models against each other in Figure 64 shows that even with a large mass added to the structure the response PSD will follow the same general trend as the stand alone structure. Applying a mass will cause an additional spectral peak(s) and attenuation, and cause some frequency shift of the spectral peaks but the general trend can still be seen for the base structure. This is important to realize because it shows that the geometry of a structure and the input PSD have a more significant impact on the response PSD than the mass loading.

Table 18: First five modes with and without the presence of a point mass with constant geometry and volume.

Model	1	9	10
Mode 1 [Hz]	5365	5021.3	1062.6
Mode 2 [Hz]	5365.9	5111.8	1184.5
Mode 3 [Hz]	7293.5	6724	2054.6
Mode 4 [Hz]	12822	11593	5898.2
Mode 5 [Hz]	14192	13390	9794.4

5.1.3. Accounting for Payloads and Impact on Response PSD

A study was performed to determine what effect the payload had on the response of the rover and to show how various payloads can be accounted for by including or not including them in the FE model based on the input PSD used. This study will tell the CSA whether they can change the mass of the payload without affecting the response PSD and how they can account for a payload. Comparing the Baseline Model to a model which does not have the payload, determined the payloads effect on the response PSD.

The Baseline Model used a point mass representing the payload while another model that did not have a mass accounting for the payload was created. The response PSD from the probe on the chassis (11Z) was extracted as it was the furthest point from the input location and incorporates the effects of the vibration through the drive arms, main axle, and rover chassis

Table 19 shows that with the 37kg mass attached to the mounting plates, the overall GRMS of the response PSD was within $0.1 G^2/Hz$ for each of the three different generated input methods (omega, integration, acceleration). It can be seen that using the CSA provided output from the wheel motors as a direct input almost doubled the GRMS value. This is because the CSA provided response PSD contains the effects of the payload, and if this PSD is applied as an input the payload is effectively being considered twice in the analysis.

When there was no point load accounted for in the model the GRMS for the response PSD increased to 2.5x that of their values with the load, except the direct input model. Looking at the direct input model, without a point mass from Table 19 and comparing to the generated input PSDs with a point mass the overall GRMS within 12-19%. This is because in the case where the point load was added to the simulation the additional mass was accounted for in the response whereas the

direct input from real world testing the mass is accounted for in the input PSD and the mass can be removed from the model. However, with the approach of not including the mass in the model the simulations' modes will not align with the true rover. This will lead to incorrect response PSD values at certain frequencies even if the overall GRMS is correct.

Table 19: Output PSD with & without 37kg point load included in Input PSD.

Input PSD	PSD RMS Output with Payload [GRMS]	PSD RMS Output without Payload [GRMS]
Displacement Input from Omega Method	0.25833	0.73752
Displacement Input from Integration Method	0.24403	0.72915
Acceleration PSD Input	0.23822	0.55557
Direct Input from CSA PSD	0.41592	0.29281

The mode frequencies with and without a point load are shown in Table 20. Looking at Table 20 mode 2 is due to the linear actuator at the rear of the rover and mode 3 differs depending on the presence of the payload attached to the rover. When there is a payload there will be a significant spectral peak around the 66-70Hz range. When there is not a payload there will still be a peak seen at 67 Hz due to the actuator but it will be reduced and a mode will be missing. The higher frequency of mode 3 when no payload is present is due to no mass flexing the entire mounting plate at this mode which also gives higher GRMS as there is more energy per small frequency band.

Table 20: Mode 1-10 of model with & without Payload.

Mode	Frequency with Payload [Hz]	Frequency without Payload [Hz]
1	0.00	0.00
2	66.91	67.16

Mode	Frequency with Payload [Hz]	Frequency without Payload [Hz]
3	68.94	92.685
4	92.60	120.90
5	125.35	143.51
6	144.44	163.15
7	150.19	170.53
8	199.10	200.85
9	200.64	216.11
10	216.70	219.14

The effects of the payload can only be realistically predicted by including the payload mass in the finite element model. Including the payload effects as part of the input spectrum will give a GRMS that is similar to expected response, but the natural frequency associated with the payload modes will not be predicted, and the response PSD will not be accurate.

5.2. CSA Rover Analysis

The ultimate goal is for the CSA to use a topology reading from satellite images of a planet's surface to create an input PSD and simulate a rover's response, so they can design and build to a known response PSD. The goal of this thesis was to determine a random vibration input for simulation and lab purposes, to replicate the ground inputs to the rover to use during field operation. Based on data and simulations of the rover driving over 200mm aggregate, a model satisfying this goal was created. This research and model is one of the first steps in achieving the ultimate goal. The model created can be used as an initial simulation, and the PSD inputs for displacement can be used as 3σ approximations for the vibration input of 200mm aggregate.

The same process used to generate the 200mm terrain input PSD can be carried across to other soil/rock based terrains. The most critical step is generating a frequency domain history of the topology and then using the appropriate method to

create a displacement PSD. The data in the frequency domain must be generated using the appropriate sampling time and correct windowing used to give a higher number of statistical DOF without losing resolution of the obtained data for the terrain. This means implementing Shannon's Theorem as described in Section 2.2.3, and windowing with 50% overlapping to retain as much of the original signal (topology in this case) as possible. An effective cut off frequency must be used to remove low frequency noise. It was determined 5.12Hz was reasonable and aligned with MIL-STD-810 for two wheeled military vehicles. Furthermore it is suggested the work of this research be repeated for the other bedrocks at the MET to start a catalogue of terrain input PSDs.

It is recommended that the simulation results contain 4σ of the field results when testing based on the model presented. The current Baseline Model is able to meet 3σ for frequencies less than 80Hz, and for specific locations (such as the center of gravity 15Z) at higher frequencies. 4σ is based on historical data from McDonnell Douglas [63] (now Maxtar). NASA uses 3σ for space transport systems [63] but, as a rover needs to last multiple years in today's world extra reservations should be made.

Obtaining higher frequency response PSDs that meet the 4σ probability level require the rover's geometry to be refined to include fasteners, connection points, finer instruments and lighter/removable components. This will align all modes and allow the input PSD to accurately excite the model. The Baseline Model can be used as a template for the rover Juno and the CSA is now able to add instruments and components to it, or split the model to create contact points as a next step.

Following these steps and methods will create the FE model for the ultimate goal, and the catalogue of terrains from the MET will give a starting point for the satellite image topology. Taking images of the planet's surface and then overlaying the catalogued input PSDs will allow for a new input PSD to be generated that is a combination of the known PSDs to generate a PSD for the planets topology. Eventually using image recognition and the database of input PSDs a unique input PSD for ever satellite image of a planet's surface could be generated. These input PSDs could be directly applied to the FE model and using optimization techniques within the FE model the rover's driving systems, suspension, chassis, and component damping could all be designed to fit a specific missions requirements. Ultimately this would reduce cost by removing the need to over engineer and design while condensing mission times through reduced prototyping and physical testing.

6. Conclusions and Future Work

The input PSD in conjunction with the Baseline model of the rover was able to predict the response PSD to within 3σ for the majority of the field response measurements at the rover's center of gravity (15Z) taken during a 360 second interval on the 200mm bedrock of the CSA's MET. The double integration method is preferred for creating displacement PSDs at low frequencies below 1000Hz range and the omega method is preferred at frequencies higher than this based on the research performed. From these findings the FE model and method for terrain input PSD generation can be used as the initial model for future simulations at the CSA to reduce the cost of prototyping and increase the rate at which designs are tested based on different topologies.

6.1. Future Work

The next steps to improve the current base model are as follows:

1. Add geometry to the payload in the simulation, this way the inertial effects of the payload as the rover vibrates can be considered and in sloped terrain the effects of a cantilevered mass can be considered.
2. Refine geometry to get more accurate response PSDs at the higher frequencies, and obtain response PSDs that contain 4σ of the field data.
3. Add side loading from x and y axis using the accelerometer data using current numerical methods to get an input displacement PSD to further refine the response PSD.
4. Collect a surface roughness study on the ground terrain to define an input PSD directly, without the need for accelerometer data. Directly determining the input PSD will remove the need for numerical methods and errors due to assumptions. Using the surface "roughness" directly measured allows the general equation for motion to be used with displacement input as a function of the ground. The stiffness and damping matrix of the rover can be generated through lab testing or simulations of the rover.
5. Include the wheels to directly take the ground inputs, the wheels can be treated as a spring mass dampener and more conveniently be included in the model and analysis. This gives the CSA the ability to simulate different wheels as well as damping and suspension systems without the cost of prototypes, and allows a specific ground type to be simulated based on the intended location of travel.
6. Vibration Response Spectrum analysis to ensure protection of onboard components. A VRS gives the ability to compare the natural frequencies of the rover and its components simultaneous against the response PSD limits to ensure exceed the CSA response PSD specification limits.

To obtain the ultimate goal of taking a topology reading from satellite images of a planet's surface to create an input PSD, first a catalogue of ground PSDs needs to be generated, as was done in this thesis for a single ground type. Once this catalogue is created the surface topology can be assessed and the given input PSD for the specific region can be applied and the super position of these PSDs can be used in areas that encompass multiple terrain types. Next using a model of the rover's base frame with the key components and onboard instruments included, the suspension and drive system can be optimized in the simulation software such as ANSYS. Several iterations of suspension systems can be trialled using numerical FE optimization methods to obtain the best system response to the expected vibration during operation to ensure attenuation on the structure.

Reference

- [1] NASA, "Moon to Mars," NASA TV, [Online]. Available: <https://www.nasa.gov/topics/moon-to-mars/lunar-outpost>. [Accessed 2 April 2019].
- [2] S. Anthony, "China's space rampage continues," Extreme Tech, 14 Jan 2014. [Online]. Available: <https://www.extremetech.com/extreme/174615-chinas-space-rampage-continues-photos-from-humanitys-first-moon-rover-in-40-years>. [Accessed 2 April 2019].
- [3] SpaceX, "Becoming a Multiplanet Species," Hawthorne, 2017.
- [4] NASA/JPL/Caltech, "Artist's conceptual image of the 2020 rover," NASA, 10 January 2017. [Online]. Available: <https://mars.nasa.gov/resources/8223/mars-2020-rover-artists-concept/?site=insight>. [Accessed 2 April 2019].
- [5] F. Martin, "Rover FE Modeling," Canadian Space Agency - Personal Communications, Longueuil, Québec, 2017.
- [6] J. K. Vandiver, Composer, *Lecture 19. Introduction to Mechanical Vibration*. [Sound Recording]. MIT Open Courseware. 2011.
- [7] A. Inc., "Lecture 3 Damping," *ANSYS Mechanical Linear and Nonlinear Dynamics*, p. 24, 2016.
- [8] Inductiveload, "File:2nd Order Damping Ratios.svg," 19 May 2008. [Online]. Available: https://commons.wikimedia.org/wiki/File:2nd_Order_Damping_Ratios.svg. [Accessed 19 April 2019].
- [9] W. Unruh, "Modes of Vibration," UBC Physics 341 - Spring 2016, Kelowna (Okanagan Valley), 2016.
- [10] J. K. Vandriver, Composer, *Lecture 23. Vibration by Mode Superposition*. [Sound Recording]. MIT Open Courseware. 2011.

- [11] D. Steinberg, *Vibration Analysis for Electronic Equipment*, Wiley-Interscience, 2000.
- [12] E. Stamper, "How Do I Calculate Fatigue in a Random Vibration Environment? - Part 1," CAE Associates, 4 December 2015. [Online]. Available: <https://caeai.com/blog/how-do-i-calculate-fatigue-random-vibration-environment-part-1>. [Accessed 3 April 2019].
- [13] T. Irvine, "Random Vibration," *Vibrationdata*, no. 4, p. 33, 2014.
- [14] Siemens, "What is a Power Spectral Density (PSD)?," 17 August 2016. [Online]. Available: <https://community.plm.automation.siemens.com/t5/Testing-Knowledge-Base/What-is-a-Power-Spectral-Density-PSD/ta-p/360969>. [Accessed 5 January 2019].
- [15] T. Irvine, "Power Spectral Density Function," *Vibrationdata*, vol. 11, p. 22, 2014.
- [16] W. Thomson, *Theory of Vibration with Applications*, Second Edition, New Jersey: Prentice-Hall, 1981.
- [17] C. Chatfield, in *The Analysis of Time Series - An Introduction*, London, Chapman and Hall, 1989, pp. 94-95.
- [18] E. Hannan, "Stationary Time Series," in *Time Series and Statistics*, London, Macmillan Reference Books, 1987, pp. 271-272.
- [19] MATLAB, "MATLAB Help," MATLAB, 14 12 2012. [Online]. Available: <http://www.mathworks.com/help/signal/ref/dspdata.ps..>
- [20] J. Otis M. Soloman, "PSD Computations using Welch Method," United States Government, Livermore, California, 1991.
- [21] C. H. & R. Randall, "Chapter 13 Vibration Measurement Equipment and Signal Analyzers," in *Shock and Vibration Handbook, 3rd edition*, New York, McGraw-Hill, 1988.
- [22] U. S. Systems, "MAC/RAN Applications Manual Revision 2," Los Angeles, CA, 1991.

- [23] Spectral Dynamics Division, "Section 9 (I), Scientific-Atlanta," in *Introduction to Vibration Testing*, San Diego, CA, 1999, p. Rev 5/72.
- [24] W. a. Myers, *Probability and Statistics for Engineers and Scientists*, New York : Macmillan, 1978.
- [25] T. Irvine, "Sample Rate, Nyquist Frequency & Aliasing," *Vibrationdata*, no. 10, p. 18, 2014.
- [26] "Shock Response Spectra Sampling Rate Criteria," OSC ME File: MISC 030-074, 1997.
- [27] "paragraphs 3.7.2 and 5.5.3.5," in *IES Handbook for Dynamic Data Acquisition and Analysis*, Institute of Environmental Sciences, 2005.
- [28] C. Shannon, "Communication in the Presence of Noise," *Institute of Radio Engineers* , 1949.
- [29] Working Group 012 of IEST Design, Test, and Evaluation Division, IEST-RD-DTE012: *Handbook for Dynamic Data Acquisition and Analysis*, Schaumburg, IL: Institute of Environmental Sciences and Technology , 2006.
- [30] T. Irvine, "Leakage and Hanning Windows," *Vibrationdata*, no. 6, p. 19, 2014.
- [31] J. L. G. L. J. Yang, "A simple approach to integration of acceleration data for dynamic soil–structure interaction analysis," *Soil Dynamics and Earthquake Engineering*, vol. 26, pp. 725-734, 2006.
- [32] B. WH, "Integration of accelerograms," *Bull Seismol Soc Am*, vol. 60, pp. 261-263, 1970.
- [33] T. MD, "Zero baseline correction of strong-motion accelerograms," *Bull Seismol Soc Am*, vol. 61, pp. 1201-1211, 1971.
- [34] C. A. Trujillo DM, "A new approach to the integration," *Earthquake Eng Struct Dynam*, vol. 10, pp. 529-535, 1982.

- [35] Z. W. Y. H. Zhou Y, "Analysis of long-period error fo raccelerograms recorded by digital seismographs," *Earthquake Eng Eng Vibrat*, vol. 17, pp. 1-9, 1997.
- [36] M. M. P. C. Iwan WD, "Some observations on strongmotion earthquake measurement using a digital accelerograph," *Bull Seismol Soc Am*, vol. 75, pp. 1225-1246, 1985.
- [37] V. M. Graizer, "Effect of tilt on strong motion data processing," *Soil Dynamics and Earthquake Engineering*, vol. 25, pp. 197-204, 2005.
- [38] D. C. Mercer, "Acceleration, Velocity and Displacement Spectra – Omega Arithmetic," *Prosig Signal Processing Tutorials*, p. 8, 2006.
- [39] "5.2," in *MATLAB 在振动信号处理中的应用 (Vibration Signal Processing)*, 2005, pp. 112, 114-115.
- [40] Department of Defence USA, "Military Standard: Environmental Test Methods and Engineering Guidelines," MIL-STD-810F, 1989.
- [41] T. Irvine, "Integration and Differentiation of Time Histories & Spectral Functions," *Vibrationdata*, vol. 22, p. 22, 2014.
- [42] Inc., ANSYS, "Lecture 6 - Harmonic Analysis," *ANSYS Mechanical Linear and Nonlinear Dynamics*, p. 55, 2016.
- [43] INC., ANSYS, "Lecture 8 - Random Vibration," *ANSYS Mechanical Linear and Nonlinear Dynamics*, p. 44, 2016.
- [44] T. Irvine, "Miner's Cumulative Damage vie Rainflor Cycle Counting," *Vibrationdata*, no. Revision C, p. 29, 2012.
- [45] K. Ahlin, " Comparison of Test Specifications and Measured Field Data," *Sound & Vibration*, Sept. 2006.
- [46] R. C. a. H. Gaberson, "Modal Velocity as a Criterion of Shock Severity," Naval Research Lab, 1969.

- [47] T. Irvine, "Power Spectral Density Functions of Measured Data," *Vibrationdata*, vol. 12, p. 30, 2014.
- [48] Department of the Navy, "NAVMAT P-9492," USA National Defence , 1979.
- [49] Department of Defence USA, "Military Standard: Test Requirements for Launch, Upper-Stage and Space Vehicles," USAF, MIL-STD-1540C, 1994.
- [50] F. a. H. G. Kube, "An Investigation To Determine Effective Equipment Environmental Acceptance Test Methods," in *Advanced Development Report ADR 14-04-73.2*, Grumman Aerospace Corporation, 1973.
- [51] International Organization for Standardization, "ISO 2631: Mechanical vibration and shock -- Evaluation of human exposure to whole-body vibration," ISO, 2018.
- [52] L. Hall, "Simulations and analyses of train-induced ground vibrations in finite element models," *Soil Dynamics and Earthquake Engineering* , vol. 23, pp. 402-413, 2002.
- [53] A. P. & D. C. S. Park, "Influence of soil deformation on off-road heavy vehicl suspension vibration," *Jounral of Terramechanics*, vol. 41, pp. 41-68, 2004.
- [54] P. A. & D. Gingras, "Mars Emulation Terrain User Guide," Canadian Space Agency, Longueuil, Québec, 2010.
- [55] T. Irvine, "General Method for Calculating the Vibration Response Spectrum," *Vibrationdata*, vol. 16, p. 16, 2014.
- [56] T. Irvine, "AN INTRODUCTION TO THE VIBRATION RESPONSE SPECTRUM REVD," NSERC, 2009, 2009.
- [57] G. o. Canada, "Juno," 25 03 2015. [Online]. Available: <http://www.asc-csa.gc.ca/eng/rovers/juno.asp..>
- [58] Canadian Space Agency , "Analyse modale Juno," Longueuil, QC, 2016.

- [59] Centre for Mathematical Modelling and Computer Simulation, "Chapter 6: Shear Locking," C-MMAS, Bangalore, INDIA , 2014.
- [60] N. H. Nguyen, Composer, [Sound Recording]. Max Planck Institute of Colloids and Interfaces. 2015.
- [61] M. Johan Granlund, "Vehicle and Driver Vibration," Forestry Civil Engineering Scotland & ROADEX , Perth Racecourse, June 2010.
- [62] O. J. Woodman, "An introduction to inertial navigation," University of Cambridge , Cambridge, 2007.
- [63] T. Irvine, "SDOF Response to Base Input in the Frequency Domain," *Vibrationdata*, vol. 15, p. 20, 2014.

Appendix A

SECTION F-F
SCALE 1 : 4

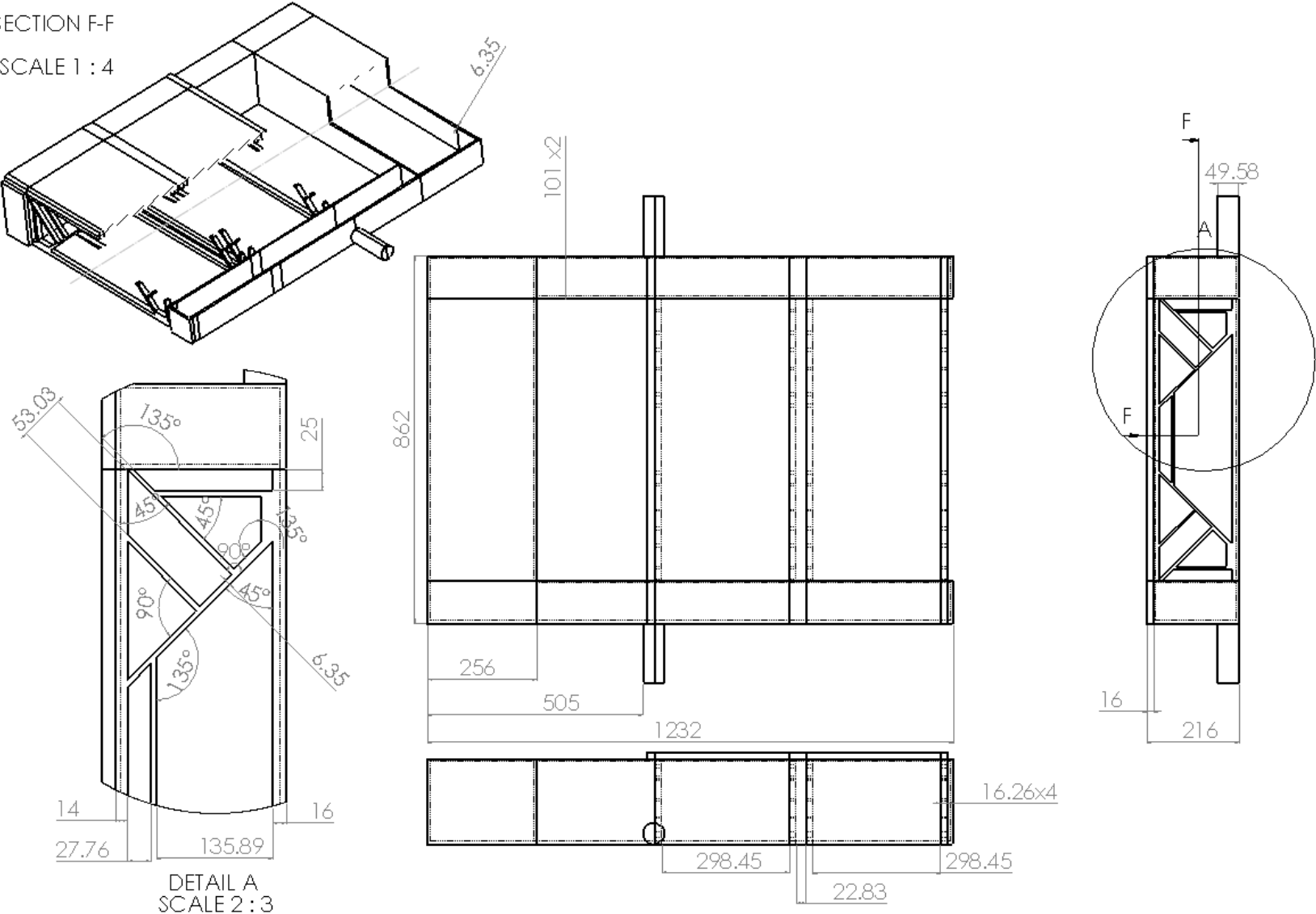


Figure A1 Dimension in mm of Initial rover geometry.

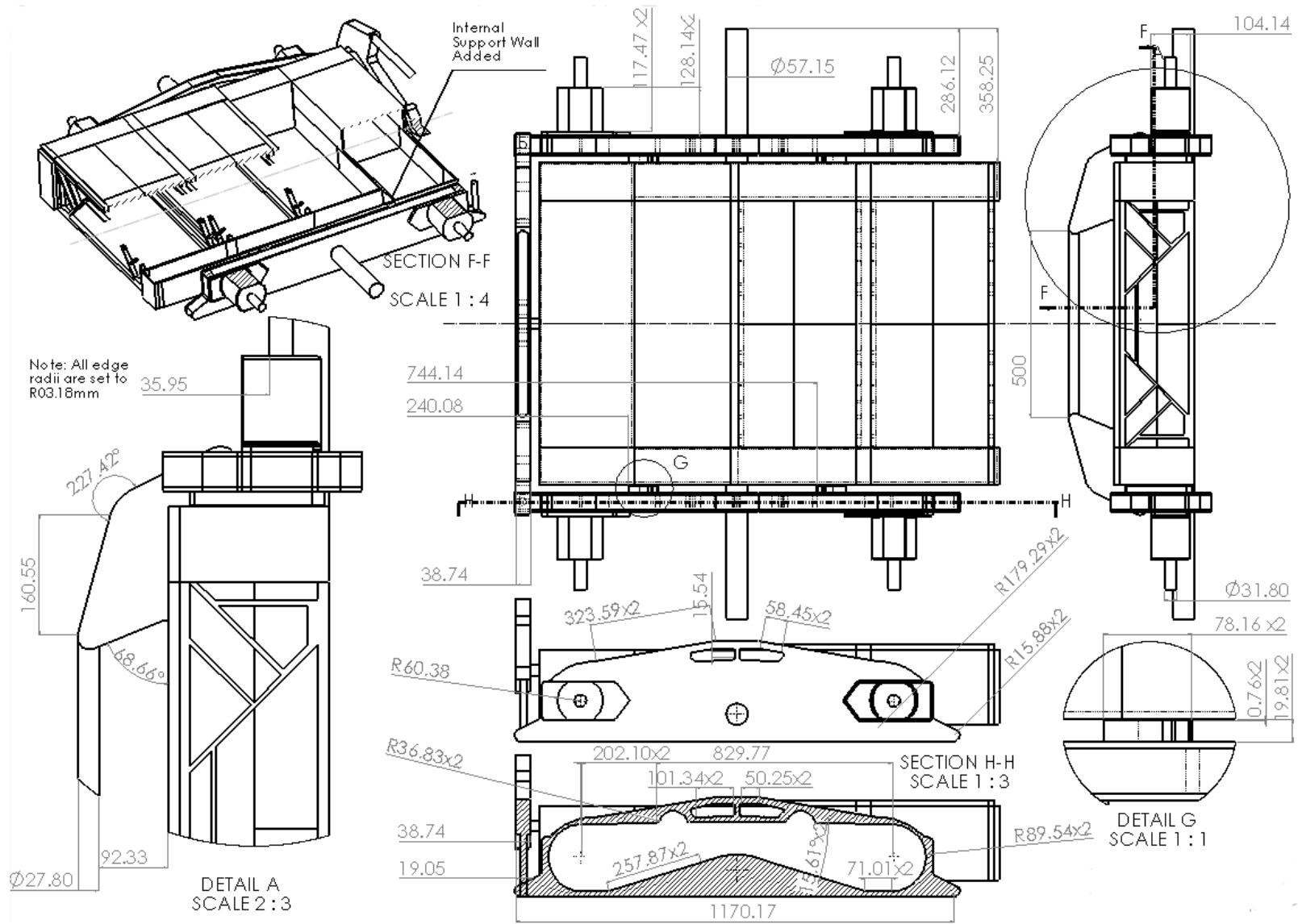


Figure A2 Baseline simulation rover geometry.